High-Precision Particle Arrangement in Gold–Polymer-Nanocomposites using RAFT Polymerization

Dissertation

zur Erlangung des mathematisch-naturwissenschaftlichen Doktorgrades
"Doctor rerum naturalium"
der Georg-August-Universität Göttingen

im Promotionsprogramm Gauss
der Georg-August University School of Science (GAUSS)

vorgelegt von
Christian Roßner

Göttingen, 2016

Betreuungsausschuss

Prof. Dr. Philipp Vana, MBA	Institut für Physikalische Chemie Georg-August-Universität Göttingen
Prof. Dr. Alec Wodtke	Institut für Physikalische Chemie Georg-August-Universität Göttingen

Mitglieder der Prüfungskommission

Referent

Prof. Dr. Philipp Vana, MBA	Institut für Physikalische Chemie Georg-August-Universität Göttingen

Korreferent

Prof. Dr. Alec Wodtke	Institut für Physikalische Chemie Georg-August-Universität Göttingen

Weitere Mitglieder der Prüfungskommission

Prof. Dr. Michael Buback	Institut für Physikalische Chemie Georg-August-Universität Göttingen
Prof. Dr. Martin Suhm	Institut für Physikalische Chemie Georg-August-Universität Göttingen
Prof. Dr. Dietmar Stalke	Institut für Anorganische Chemie Georg-August-Universität Göttingen
Prof. Dr. Claudia Höbartner	Institut für Organische Chemie Georg-August-Universität Göttingen

Tag der mündlichen Prüfung: 27.09.2016

Abbreviations and Symbols

4-ClMeBnA	4-(chloromethyl)benzyl acrylate
ACCN	azobis(cyclohexanecarbonitrile)
AF(M)	atomic force (microscopy)
AgNP	silver nanoparticle
AIBN	azobis(isobutyronitrile)
approx	approximately
ATRP	atom-transfer radical polymerization
AuNP	gold nanoparticle
br	broad signal
calcd	calculated
CCD	charge-coupled device
CPB	concentrated polymer brush
d	doublet
DC	Daoud–Cotton
DEGEMA	diethyleneglycol ethylmethacrylate
DEGMMA	diethyleneglycol methylmethacrylate
DFT	density functional theory
DLS	dynamic light scattering
DMAAM	*N,N*-dimethylacrylamide
DMAc	*N,N*-dimethyacetamide
DMAEMA	*N,N*-Dimethylaminoethyl methacrylate
DMF	*N,N*-diemthylformamide
DMSO	dimethylsulfoxide
DMT	Derjaguin-Muller-Toporov
DNA	deoxyribonucleic acid
EELS	electron energy loss spectroscopy
EDTA	ethylenediaminetetraacetic acid
EFTEM	energy-filtered transmission electron microscopy
equiv	equivalents
ESI	electrospray ionization
et al.	*et alii*
etc	*et cetera*
GIF	Gatan imaging filter
GMA	glycidyl methacrylate
HBP	hyperbranched polymer
IFT	indirect Fourier Transformation
IONP	iron oxide nanoparticle
IR	infrared
IUPAC	International Union of Pure an Applied Chemistry
LAMP	lipoic acid 2-hydroxy-3-(methacryloyloxy)-propyl ester
LCST	lower critical solution temperature
LSPR	localized surface plasmon resonance
m	multiplet

MPC	2-(methacryloyloxy)ethyl phosphorylcholine
MS	mass spectrometry
N^{i}PAAM	*N*-isopropylacrylamide
NMR	nuclear magnetic resonance
NMRP	nitroxide-mediated radical polymerization
NP	nanoparticle
P(4-ClMeBnA)	poly(4-(chloromethyl)benzyl acrylate)
PDDF	pair-distance distribution function
PDMAAM	poly(*N,N*-diemthylacrylamide)
PDMAEMA	poly(*N,N*-diemthylaminoethyl methacrylate)
PEG	poly(ethylene glycol)
PEO	poly(ethylene oxide)
PdNP	palladium nanoparticle
PGMA	poly(glycidyl methacrylate)
pH	pondus hydrogenii
PMAA	poly(methacrylic acid)
PMMA	poly(methyl methacrylate)
PMPC	poly(2-(methacryloyloxy)ethyl phosphorylcholine)
PN^{i}PAAM	poly(*N*-isopropylacrylamide)
POEGMA	poly(oligo(ethylene glycol) methacrylate)
ppm	parts per million
PS	polystyrene
PSS	polymeric support system
PTFE	polytetrafluoroethylene
PVBC	poly(vinylbenzylchloride)
PVP	poly(vinylpyridine)
q	quartet
RAFT	reversible addition−fragmentation chain transfer
ref.	reference
RDRP	reversible-deactivation radical polymerization
R group	RAFT leaving group
s	singlet
SAXS	small-angle X-ray scattering
SDPB	semi-dilute polymer brush
SDV	styrene-divinylbenzene copolymer
SEC	size-exclusion chromatography
SEM	scanning electron microscopy
SI	surface-initiated
SiNP	silica nanoparticle
stat	statistical
STEM	scanning transmission electron microscopy
STEM-SI	scanning transmission electron microscopy and spectrum imaging
t	triplet
TE(M)	transmission electron (microscopy)
TGA	thermogravimetric analysis
THF	tetrahydrofuran

TOAB	tetraoctylammonium bromide
TTC	trithiocarbonate
UV	ultraviolet
VBC	vinylbenzylchloride
vis	visible
VP	vinylpyridine
XPS	X-ray photoelectron spectroscopy
Z group	RAFT stabilizing group

Abstract

This thesis provides a comprehensive analysis of the scientific background on nanocomposites generated via reversible-deactivation radical polymerization (RDRP) techniques. Starting from this basis, nanocomposites with the special combination of a polymeric part from reversible addition–fragmentation chain transfer (RAFT) polymerization and gold nanoparticles were investigated in greater detail. It was shown by means of elemental mapping via scanning transmission electron microscopy and spectrum imaging (STEM-SI) in hybrid gold/RAFT polymer core–shell particles that the RAFT polymers' sulfur-containing end group is always co-localized with the lateral position of gold cores. This provides, for the first time, microscopic evidence for the claim that the RAFT moiety can be used as an anchoring group for the grafting of polymers to gold nanoparticles. The interaction strength of the trithiocarbonate-type RAFT group used in this work was also investigated employing a specially developed model system and following a literature-known UV/vis-based method for analyzing the Langmuir isotherm of adsorption. For the trithiocarbonate model system studied here, a similar free enthalpy of adsorption (-36 kJ mol^{-1}) as compared with phenyl dithioesters studied earlier had been obtained.

The characteristic features of RAFT polymerization had been exploited for the fabrication of defined particle arrangements. The discovery was made that RAFT polymers with specific macromolecular design can be used to assemble gold nanoparticles into unique nanohybrid architectures. It was demonstrated the possibility to precisely arrange gold nanoparticles in a controllable fashion by rationally tailoring the polymers used. Specifically, two different systems were realized to illustrate this point: (i) Gold nanoparticles from the two-phase Brust–Schiffrin synthesis were found by means of transmission electron microscopy (TEM) and dynamic light scattering (DLS) to assemble into globular particle network structures, when they are treated *ex situ* after their synthesis and work-up with linear RAFT oligomers of styrene featuring trithiocarbonate groups at both their termini (telechelic oligomers) or evenly distributed along the backbone (multifunctional oligomers). Here, the density of the primary gold nanoparticles within the network structures can be controlled by adjusting the degree of polymerization of the oligomeric particle linker, as evidenced by TEM. (ii) Higher-order particle assemblies featuring a hierarchical arrangement of two types of gold nanoparticles can be obtained from gold-core–RAFT-star-polymer-shell scaffold architectures. Such nanohybrid particles are shown to provide free star polymer termini (featuring

trithiocarbonate groups) in the polymeric shell, which are accessible for further functionalization reactions. Addition of a second type of gold nanoparticles to such scaffold architecture leads to the attachment of these particles on the exterior of the polymer shell, resulting in planet–satellite nanostructures. These unique nanoarchitectures had been thoroughly analyzed by a combination of several analytical techniques, including electron microscopy in the dried state and small-angle X-ray scattering for characterization in the colloidally dispersed state. When the planet–satellite structures are cast on surfaces for TEM characterization, it is found that the planet–satellite distance can be tightly controlled by adjusting the degree of polymerization of the star polymer linker. These nanostructures can also be equipped with functional polymer, illustrating the possibility of combining several distinct building units into one highly functionalized and well-defined nanostructure.

Foreword

Humans have always been intrigued by the formation of ordered structures from chaos; this may find its best expression in the fact that already at the very beginning of the developing rational thinking (LÓGOS), the cosmos and its decorative order were central and recurring subjects of debate of the presocratics.[1] This fascination for order formation persists, as is exemplified today for example by the study of the assembly of distinct building units into defined architectures performed within the intellectual framework of chemistry:[2] It is justified to claim that the formation of structures and their control on different length scales is one of the major driving forces within contemporary chemical sciences.

On the length scale of small molecules, chemists had been remarkably successful in synthesizing chemical compounds with intriguing complexity. Also on the larger micrometer-length scale, specific structuring can be successful by using masking techniques[3] or lithography.[4] The powerful and widely applied lithographic methods, however, currently reach their inherent limitations (dictated by the laser wavelength, numerical aperture of the lens used, and diffusion of the photo-resist) regarding the smallest possible size resolution (< 20 nm). Yet, there is a tremendous demand in further miniaturization of devices for technological applications.[5] Consequently, there is vibrant research activity in the precision design of smaller structures and their assembly on substrates (for specific applications).[6] Novel strategies are currently under exploration. For example, the precise synthesis of structures[7] with feature sizes of few to some tens of nm and their controlled assembly[8] can be already achieved with DNA origami. While this particular technique is rapidly developing toward achieving these goals,[7,8] it requires sophisticated design and synthesis procedures, offers only limited flexibility with regard to the chemical composition of the produced structures and is generally only suited for the production of sub-milligram quantities of material. It is, therefore, of huge scientific interest to develop scalable, efficient and flexible nanodesign strategies.

At the molecular level, polymers are predestined for such structuring purposes, which is due to their size (in the nm regime) and because they can be accurately designed (see Figure 1).[9] Concerning the targeted fabrication of polymers, the emergence of reversible-deactivation radical polymerization (RDRP) techniques has opened intriguing possibilities for material design and paved the way for innovative materials by enabling scientists to achieve a high level of structural precision.[10,11] RDRP methods provide a handle for the fabrication of polymeric materials with specific

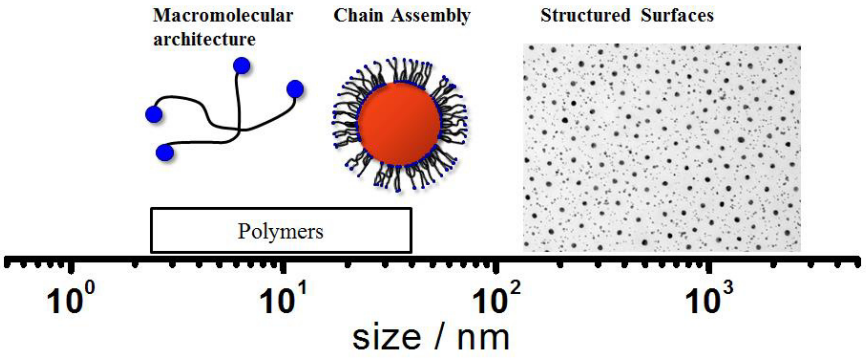

Figure 1 Polymer-based structures on different length scales which can be obtained by controlling the macromolecular architecture of individual chains, by the assembly of multiple chains (for example on the surfaces of colloidal particles), and from long-range ordered assembly of nanohybrid particles on surfaces.

topology, special functionality, defined composition, and with adjustable molar mass as well as small dispersities. Hence, well-defined macromolecular architectures are accessible with relative ease. To be specific, macromolecules with particular topologies such as, for example, graft copolymers[12] or star polymers,[13] are accessible via RDRP techniques. It is possible to introduce specific functionality at one chain end,[14] or along the polymeric backbone.[15] Moreover, a defined positioning of distinct monomers along the polymeric backbone can be achieved, leading to block copolymers[16] or even sequence-controlled macromolecules.[17,18] By such tailoring of macromolecules at the molecular level, it is possible to guide the formation of structures in a rational fashion and to impart some level of hierarchy to these structures: From the molecular parameters that can be controlled by RDRP techniques, the ability for self-assembly can emerge, like for example in block copolymers, which have an inherent tendency to phase-separate and hence form ordered structures in solution[19] and in the molten state.[20] Beyond that, these ordered structures can be used in conjuncture with inorganic nanoparticle building blocks, aiming at using the polymers as templates to control nanoparticle arrangement in polymer/inorganic nanocomposites.[21,22] This offers a powerful access to nanostructured materials in a 'bottom-up' fashion.

The conceptual framework of this dissertation is grounded on the line of thoughts presented above. Insofar, this work is meant as a contribution toward the development and analysis of nanodesign strategies which are based on well-defined synthetic polymers from RDRP techniques. The systems developed here have inherent model character, as they exemplify

how in principle defined macromolecules can be used to fabricate structurally ordered nanohybrids. This model character allows drawing more general conclusions from the results obtained in the presented work, although the studied systems are of course very special in their realization and behavior. I believe that these general results will prove useful for the development of novel methods for the challenging structure formation with feature sizes of few nanometers.

The following thesis will be structured as outlined below: The opening Chapter 1 of this thesis will introduce into the scientific background in the field of tailored nanocomposites with synthetic polymer from controlled radical polymerization techniques. After this more general introductory part, the focus of this work will be laid on gold/RAFT polymer nanohybrid materials. Aspects about the interaction between the inorganic and polymer components in this special combination will be addressed in Chapter 2. Chapters 3 and 4 describe in detail the design, synthesis, and structural characterization of ordered gold nanoparticle arrangements, realized by using RAFT polymers with special macromolecular architecture. General Conclusions as well as Future Perspectives are given in Chapter 5.

Table of Contents

High-Precision Particle Arrangement in Gold–Polymer-Nanocomposites using RAFT Polymerization

Chapter 1

Tailoring Nanocomposites via Controlled Radical Polymerization: State of the Art[1]

1.1 Preface

Inorganic nanoparticles (NPs) have been recognized as building units for the construction of materials that take advantage of the specific properties of NPs.[23] In order to obtain particles that are compatible for incorporation into such materials, it is necessary to shield their reactive surfaces with stabilizing ligands. To this end, functionalization of NPs with a polymer shell is an attractive way to introduce colloidal stability and at the same time modulate the properties of the resulting nanomaterial and equip it with stimuli-responsiveness.[24–26] The functionalization of particles with polymer can be undertaken by two different approaches: Using the so-called *in-situ* functionalization, it is possible to induce NP formation in the presence of polymers, which act as stabilizers for the growing particles. This strategy can, for example, be implemented using water-soluble reversible addition–fragmentation chain transfer (RAFT) polymers with dithiobenzoate termini, which can be reduced to thiol groups in the presence of a gold or silver salt precursor, leading to stable nanocomposites.[27] Alternatively, NPs can be functionalized *ex situ* after their synthesis and work-up, either directly with polymers ("grafting-to")[28] or with an initiator/chain transfer agent for surface-initiated (SI) polymerizations ("grafting-from")[29,30]. The types of inorganic particles most often encountered in nanocomposites, and therefore treated in this overview

[1]Adapted with permission from Rossner, C.; Vana, P. *Adv. Polym. Sci.* **2016**, *270*, 193–220, Copyright 2015, Springer International Publishing Switzerland.

chapter, are noble metal NPs, metal oxide NPs, and quantum dots. Metal NPs are particularly interesting because of their unique optical properties, which stem from surface plasmon resonance.[31] As a result of their chemical stability and facile surface modification, gold nanoparticles (AuNPs) are extensively studied representatives of this class. They are also interesting in the realm of controlled radical polymerization, as RAFT polymers inherently contain anchor groups for gold surfaces. It has been shown that trithiocarbonate (TTC) and dithiobenzoate groups attach to gold[32,33] (see also Chapter 2). Metal oxide NPs can also be readily conjugated with polymers via established anchor moieties,[34] while the choice of anchor group might also influence the structure of the resulting nanocomposites.[35] Their incorporation into hybrid materials with polymers could lead to modulation of mechanical properties and also to cost reduction. CdSe quantum dots received special attention due to their possible applications as luminescent tags and probes.[36]

Controlled radical polymerizations (also called reversible-deactivation radical polymerization, RDRP, according to IUPAC) offer a unique way to modulate polymeric materials at the molecular level. By exploiting a dormant state of the propagating macroradical, the fraction of irreversibly terminated species among the produced macromolecules can be reduced to a small number, which imparts "living" characteristics to the system and therefore enables the formation of complex macromolecular architectures, such as block copolymers and star polymers. Under typical conditions, the macromolecular species are rapidly switched between the dormant and an active state, which leads to an equal distribution of growth probabilities for all chains and may result in narrow molar mass distributions. It is thus possible to produce uniform polymers with defined molecular characteristics. These characteristics are defined by a large parameter space (monomer composition, degree of polymerization, degree of branching, distribution of special functional groups, etc.) which opens a huge operational window for macromolecular engineers to design polymers to meet specific requirements. In recent years, significant advances in the field of nanocomposites have relied on the combination of specially designed macromolecules from RDRP techniques with inorganic nanoparticles to control hybrid structure formation.[37] In this chapter describing the state of the art of this rapidly developing field, the literature of the past 10 years is examined to evaluate if and how macromolecular design by means of controlled radical polymerization can be used to prepare polymer/inorganic nanocomposite materials with controlled architectures (location of NPs in polymer matrices, interparticle spatial relations, etc.) and properties. In contrast to more comprehensive review articles on the more general topic of

assembly in polymer/colloid systems,[38,39] the focus is here laid on strategies in which controlled radical polymerization plays a key role.

1.2 Linear Homopolymers

In this section, the simplest case of homopolymers attached to a solid substrate with one end group will be considered. The polymer is thus composed of exactly one particular monomeric repeating unit; the average degree of polymerization of which can be controlled via living radical polymerization techniques. Hence, this type of polymer contains two sorts of information: (i) the functional group that is repeatedly expressed in the polymeric side chain or at the chain end remote from the surface, and (ii) the average size of one macromolecule. Both features influence the properties of composite materials of inorganic particles with polymers on their surfaces.

Homopolymers with distinct side chain functionalities can be obtained directly through homopolymerization or after post-polymerization modification of a polymer with reactive functional groups in its backbone, which can act as a platform for the preparation of a library of homopolymers with defined side chain moieties.[40,41] The polymeric backbone can be chosen such that stable nanocomposites with NPs in the respective solvent can be obtained. Such stabilizing polymers can, for example, be applied in NP functionalization together with destabilizing molecules in varying molar ratios in order to control the aggregation of NPs in colloidal dispersion.[42] Regarding the chemistry in the polymer side chains, it is particularly interesting to study homopolymer brushes in cases where the monomeric repeating unit is capable of undergoing specific interactions that are rather weak individually, but significantly enhanced in the case of multivalent interactions.[43] As a result of such multivalent interactions, materials with fundamentally new properties are obtained when homopolymers bearing weakly interacting repeating units are assembled on a solid support. An illustrative example of this principle is the so-called glyco-cluster effect, which is the reason why nanocomposites with glycopolymers have been investigated extensively in recent years.

RAFT polymerization is arguably tolerant to functional groups present in the monomer to be polymerized and also provides end groups that can be used as surface attachment points with or without additional post-polymerization modification. Therefore, monomers bearing unprotected glucoseamine,[44] glucoseamido and lactobioamido,[45] mannose,[46] or galactose[47] moieties can be polymerized in a RAFT process and their

polymers grafted to NP surfaces. As an alternative to the direct polymerization of glycomonomers, the sugar moiety can be clicked to the polymeric backbone in a tandem polymerization [3+2]-cycloaddition reaction.[48] Nanocomposites of glycopolymers with AuNPs form complexes with lectins, which can lead to AuNP clustering and result in a plasmon band red shift.[44,46] This recognition through complex formation may even be glycopolymer-specific.[44,47] Complex formation with lectins can be further exploited in developing cancer theranostics:[49] RAFT homopolymers with glucoseamine in their side chains can also be used to prepare nanocomposites with iron oxide nanoparticles (IONPs) of different shapes. The authors demonstrated that these nanohybrids attached to cell membranes of HeLa carcinoma cells expressing glucose transporters on their membranes. Also, the internalization of IONPs coated with glycopolymer was significantly increased compared with unmodified IONPs.[49]

It should be noted, however, that substrate recognition through gold nanocomposites with a homopolymer layer is indeed a broad concept not limited to glycochemistry: Recognition can also lead to quantitative and cation-specific detection.[50] AuNPs covered with poly(methacrylic acid) (PMAA) were shown to aggregate upon exposure to Cr^{3+} cations. This led to a concentration-dependent shift of the localized surface plasmon resonance (LSPR) absorption band. After exposure to analyte solution, the sensor could be recovered by removal of Cr^{3+} using EDTA. When the recognition element implemented into the polymer brushes is self-complementary, nanohybrids with a tendency to form assembled network structures are formed.[51] This can be realized by decorating RAFT polymers with the ureidopyrimidone moiety at the α-chain end and grafting those polymers to AuNPs with the sulfur-containing ω-end. Therefore, the functionality that acts as recognition element does not need to be incorporated into the polymeric backbone, but can instead be located at the dangling end of the polymer brush that is remote from the particle surface, as the monomeric repeating units act as a spacer.

RDRP techniques allow the preparation of macromolecules with predetermined degree of polymerization and narrow molar mass distribution. When such macromolecules are grafted onto the surface of NPs, it is interesting to investigate whether this size information can be used to organize inorganic particles in ordered assemblies. Following this idea and using surface-initiated atom transfer radical polymerization (SI-ATRP), Fukuda and coworkers assembled nanocomposites of AuNPs[52] and SiNPs[53] with a poly(methyl methacrylate) (PMMA) shell in a two-dimensional array using Langmuir–Blodgett deposition. The authors found that the PMMA

shell keeps the AuNP cores at certain distances, which become larger with increasing graft chain length. Using atomic force microscopy (AFM), it was demonstrated that the PMMA forms a compact shell on top of one AuNP and a stretched shell around individual AuNPs, which causes the gold core spacings.[52] Analogous shell morphology in gold nanocomposites was also revealed by Davis *et al.*, who observed a soft shell assembled around a hard core in phase contrast AFM images of hybrid particles deposited on a solid substrate.[54] The brushes on top of a particle were pulled downwards during the solvent evaporation process (Figure 1.1). When polymers are terminally grafted onto a surface at a high density, the surface-bound macromolecules adopt extended conformations and stretch away from the surface, this is, the grafted polymer is in the concentrated polymer brush (CPB) regime. A unique feature of particle surfaces is that, as a result of their curvature, the concentration of polymer segments decreases in regions remote from the surface. This can lead to surface-bound polymer eventually going into the semidilute polymer brush (SDPB) regime, as a result of decreasing packing constraints.[55,56] Dynamic light scattering (DLS) measurements of polymer brush height on individual nanohybrid particles[55,57] and confocal laser scanning microscopy of three-dimensional colloidal crystals[55–58] confirm this behavior. The scaling of polymer brush height can be understood roughly in terms of a simple blob model pioneered by Daoud and Cotton.[59] This model was originally developed to describe star polymer conformations, but can also be applied to polymer brushes attached to a solid core. When the number of branches (i.e., the grafting density) is high, the individual branches adopt a stretched conformation in regions close to

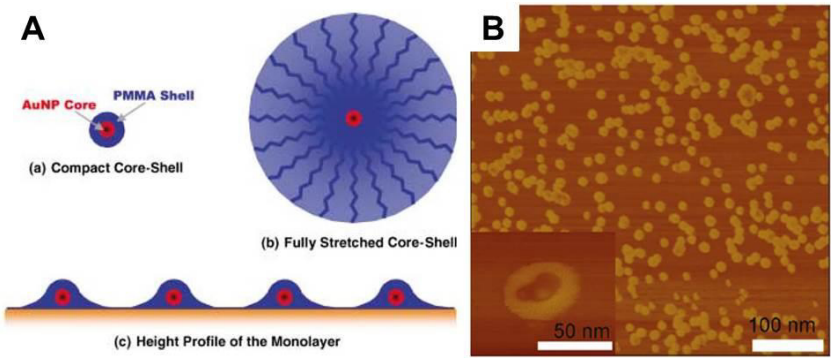

Figure 1.1 The sketch in image (A) depicts a structural model for a monolayer of hybrid particles, developed based on AFM measurements. Adapted with permission from ref. 52. Copyright 2003 Wiley-VCH Verlag GmbH & Co. KGaA, Weinheim. The phase contrast AFM image (B) shows a soft layer of polymer assembled around a hard gold particle core. Adapted with permission from ref. 54. Copyright 2009 American Chemical Society.

the core. Farther from the core, the individual branches might begin to relax because of the increased volume available for the chains, leading to a different scaling of star radius with the number of repeat units in a branch *N*. For large *N*, the Daoud−Cotton (DC) model predicts a scaling of star radius (polymer brush height) of ~$N^{0.6}$. This scaling is in agreement with polymer brush heights measured by DLS in this regime.[60] However, the simple DC model fails to describe the behavior of brushes for smaller brush heights (i.e., when the chains are in the CPB regime). In this case, brush height was shown experimentally to scale with ~$N^{0.8}$, an intermediate scaling between ~$N^{0.6}$ and ~$N^{1.0}$, the latter being the limit for highest grafting density and minimum surface curvature (i.e., dense polymer brushes on flat surfaces).[60] Fukuda and coworkers applied the DC model to brushes grafted onto a large core to investigate at what distance from the center of the particle the crossover from CPB to SDPB takes place.[55] This critical distance r_c was found to be given by:

$$r_c = \frac{r_o \cdot \sqrt{\sigma^*}}{\sqrt{4\pi} \cdot v}, \qquad (1.1)$$

where r_o is the radius of the inorganic core, σ^* the dimensionless grafting density, and v the excluded volume parameter. It follows that for small enough grafting densities, r_c will be smaller than r_o and the whole polymer brush thus shows SDPB behavior. For large enough values of σ^* and small polymer brush heights, the entire brush shows CPB behavior. At a critical brush height r_c, the CPB-to-SDPB transition occurs. Thus, the height of a polymer brush on an inorganic particle clearly scales with the degree of polymerization of the grafted chains, and the scaling behavior can provide the information about whether the polymer is in the concentrated brush regime or not. This is valuable information, as it was recognized that the mechanical properties of self-assembled structures from hybrid particles are strongly influenced by the CPB−SDPB transition because more interparticle chain entanglements can occur in the SDPB case.[61,62] The toughness of the hybrid materials of silica NPs with polystyrene (PS) and PMMA brushes was found to increase as the polymer brush height increased beyond the CPB−SDPB crossover.[62] On the other hand, material properties that do not depend much on polymer entanglements (i.e., the elastic modulus and hardness of the material) were shown to increase with increasing polymer brush molar mass and level off before the CPB-SDPB transition occurs (Figure 1.2).[62]

The state of the polymer brushes also affects the order formation in two-

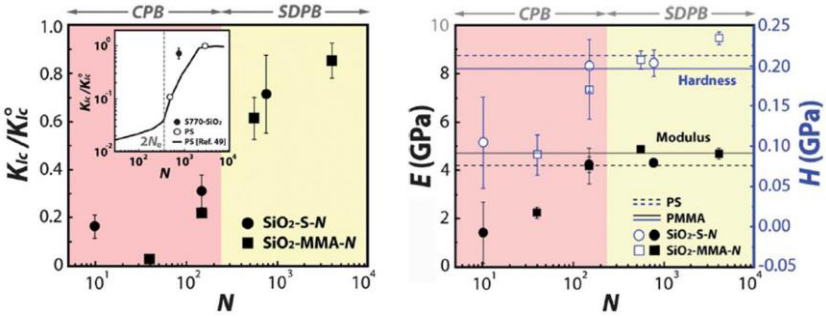

Figure 1.2 Mechanical properties of nanocomposites of silica NPs with PS and PMMA. The development of material toughness with the average number of monomeric repeat units per brush *N* is shown in the diagram on the left hand side. The plot on the right hand side shows the dependence of elastic modulus *E* and hardness *H* on *N*. Adapted from ref. 62 with permission of The Royal Society of Chemistry.

dimensional nanohybrid assemblies, because the SDPBs do not add significantly to the interparticle repulsive potential and act to dilute the array structure, resulting in decreased assembly order as the system goes far into the SDPB regime.[63] However, this behavior can be exploited intentionally by grafting bimodal polymer brushes, one of which is short and of high grafting density to shield the particle surface and one that is long with low grafting density, to achieve nanohybrids that can be better dispersed in a polymer matrix,[64] preventing particle assembly and structuring.[65] In such a molten state or blend, growing interparticle distances with increasing molar mass of the surface-bound polymer can also be observed by small-angle X-ray scattering (SAXS), and it was found that the interparticle distances can be further swollen by blending the hybrid particles with free polymer.[66] In the case of AuNPs, the gold core spacing results in unique optical responses, which stem from surface plasmon coupling[67] or, when the spacing is of the order of the wavelength of visible light, from Bragg diffraction.[55,58,68]

Nanocomposites with a tailored polymer shell thickness can also be obtained through RAFT polymerization surface-initiated from silica[69,70] and IONP surfaces,[69] or via grafting-to approaches.[71,72] The grafting-to strategy is particularly interesting because it can allow the precise control of the polymer properties independently of the NP, prior to immobilization on a surface. For such an attachment of polymer chains, it is necessary that the enthalpy gain from the interaction of the anchor moiety with the surface balances the loss of entropy of the polymer chain. This entropy loss is reflected in a decrease in polymer grafting density with increasing average molar mass of the employed polymer, which was verified for two types of

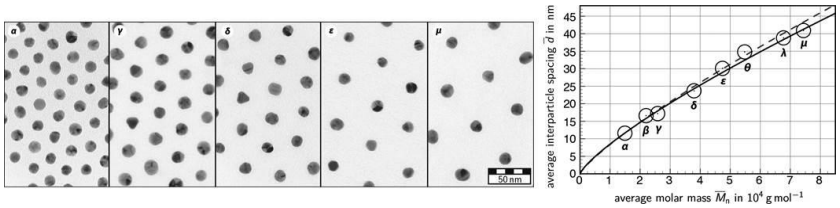

Figure 1.3 The TEM images on the left hand side show self-assembled monolayers from nanohybrid particles with gold cores and PN^{i}PAAM shells. The average degree of polymerization of N^{i}PAAM increases from left to right. The plot on the right hand side shows the dependence of interparticle spacing on the average degree of polymerization. Adapted with permission from ref. 71. Copyright 2013 American Chemical Society.

AuNPs.[72] This behavior is logical, since the increased entropy loss (resulting from the conical confinement of longer polymer chains) can only be counterbalanced by more relaxed conformations as a result of their confinement in a larger space (i.e. by reducing the grafting density). When homopolymers are grafted to NPs with one end group, the question of whether they form brushes on the surface can be answered by determining the polymer shell thickness as a function of polymer molar mass. This shell thickness can be quantified by systematically measuring the edge-to-edge distance between inorganic NP cores in self-assembled monolayers (Figure 1.3).[71] The data points obtained from the analysis of several TE micrographs can be fitted to a function describing the increase in average interparticle distances $\bar{d}$ with the increase in number average molar mass of grafted polymer. A simple yet suitable function can be chosen of the following form:

$$\bar{d} = k \cdot \left[M_n\right]^{1/l} . \qquad (1.2)$$

A fit of (1.2) to the data yields $k = 6.02 \cdot 10^{-12}$ m and $1/l = 0.79$. When k is indentified to be twice the contour length of the polymer and set fixed to this value ($4.4 \cdot 10^{-12}$ m), a value of 0.82 is obtained for the exponent $1/l$. Taking into consideration how the molar mass of surface-bound polymer translates to polymer shell thickness, this value obtained for $1/l$ might reflect densely grafted polymer brushes on the NP surface, provided that interparticle spacing in self-assembled monolayers can indeed be used as a measure of polymer shell thickness. That is, the information that is included in the scaling of interparticle distance with molar mass can be used to draw conclusions about the conformational state of the surface-anchored polymer chains.

1.3 Mixed Brushes of Two Different Linear Homopolymers

When two chemically different types of polymer are grafted to NPs, the situation becomes much more complex because the properties of both species influence the behavior of the resulting nanocomposites, depending on the individual chain lengths, grafting densities, and chemical properties of the two different brushes. Also, the different polymers might be grafted independently of each other, leading to a statistical distribution of both polymers on the surface, or they might be grafted as diblock copolymers at their block junction. Because the outcome of the latter results in mixed polymer brushes, this special case will be discussed here and not in Section 1.4 which deals with copolymers in a more general sense. The behavior of nanocomposites with mixed brushes can reflect the properties of both polymeric species at the same time or it can be intermediate between those of NPs with the respective homopolymer brushes. Grafting of brushes with different solubility characteristics can lead to amphiphilic nanocomposites with a tendency to phase-separate on the surfaces. The phase separation of immobilized macromolecules into different domains is a unique feature of mixed brushes and is particularly interesting because, unlike micelle formation in solutions containing free amphiphilic (macro)molecules, the outcome of the assembly is not influenced by the dilution of the system. Also, as shown in this section, phase separation in mixed brushes on NP surfaces and its modulation can prove useful in tuning nanocomposite properties and directing particle assembly.

Different surface morphologies (including rippled structures, different island structures with varying number of islands and layered structures) resulting from microphase separation of two anchored polymer species can be predicted from a theoretical model, depending on the chain lengths and composition of mixed brushes on NP surfaces.[73] It can be predicted theoretically that lateral phase separation of two different polymer brushes on surfaces occurs in a marginally good nonselective solvent if both chains are of nearly equal or only slightly asymmetric in length. If one polymer species becomes larger, the smaller polymers form domains in a bottom layer close to the surface and the top layer is composed exclusively of the longer stretched polymer.[74] This predicted behavior has later been confirmed experimentally.[75] Because the topology of separated polymer brushes on surfaces depends so strongly on the architecture of the polymeric species (i.e, the grafting density of both brushes and their degree of polymerization), the formation of well-defined mixed brushes on NP surfaces requires polymerization techniques that allow precise control over

macromolecular properties. To this end, the use of macroRAFT agents for the formation of diblock copolymers with gold-binding TTC groups at the block junction has been suggested.[76] This approach is interesting because it implies that the ratio of grafting densities for the different blocks is always equal to one. Alternatively, the different brushes can be grafted to the NP surface as individual homopolymers through specific reactions between the homopolymer end groups and functional groups on the particle surface.[77] This could offer a handle for tuning the ratio of the two grafting densities by adjusting the polymer feed ratio. Another elegant and much-adapted method for preparing precisely tailored mixed polymer brushes is the SI-ATRP followed by nitroxide-mediated radical polymerization (NMRP) from an asymmetric initiator that can be grafted to a surface of the particle and comprises initiation sites for both types of controlled radical polymerization techniques.[78] The two successive polymerizations lead to block copolymers grafted through their block junction. The resulting NPs show chain reorganization in response to a selective solvent environment that can lead to mobile and collapsed phases.[78] Employing this SI polymerization technique with asymmetric initiator, it can be shown by TEM that lateral microphase separation occurs in nonselective good solvents when the polymer molar mass reaches a certain threshold value, and that a selective solvent leads to collapsed domains of the polymer species interacting unfavorably with the solvent.[79,80] A systematic experimental study showed from the analysis of TEM images, that the domain sizes grow strictly with the average molar mass of the grafted brushes, although the exact scaling behavior was dependent on whether the particles were drop-cast from a (nonselective) good or bad solvent.[81] A lower grafting density of mixed brushes also leads to larger domain sizes, until the grafting density reaches a lower threshold value, below which no phase separation can be observed.[82] Lateral phase separation apparently leads to wedge-shaped separated domains if the curvature of the solid particle becomes large enough.[83] Phase separation is different in isolated nanohybrids compared with nanohybrids in self-assembled monolayers. For isolated hybrid particles, phase separation only occurs at the bottom close to the substrate, whereas interparticle brush interactions lead to extended phase-separated regions between neighboring particles.[84]

The influence of the mode of attachment of different brushes was also investigated. Mixed brushes of PMMA and PS were grown from a flat silica surface by either SI conventional radical polymerization or successive ATRP (PMMA brush) and NMRP (PS brush) from a common asymmetric initiator for both techniques, attached to the surface with one grafting point. Conformational changes in grafted polymer chains were studied

theoretically and experimentally by investigation of microphase separation after solvent exchange cycles with toluene and acetone. It was found that microphase-separated areas were larger for individually anchored PMMA and PS brushes. This effect was explained by density fluctuations of the different polymer species, which occur using this approach. Also, the memory measure (the probability that a specific domain re-forms after one cycle) was smaller for diblock copolymers grafted at their block junction. This was noticed as an indication that local fluctuations in grafted polymer chains act as nuclei in the domain structure formation.[85]

Randomly distributed mixed brushes of PS and PN^{i}PAAM on AuNPs can be obtained by *in-situ* reduction of a gold salt precursor in the presence of RAFT homopolymers.[86] The presence of both types of polymers on the AuNPs can be demonstrated by NMR and IR. When thin films of the composite material are prepared via hydrophilic Langmuir–Blodgett transfer, a more hydrophobic surface is obtained than with hydrophobic transfer, as shown from contact angle measurements after depositing a water drop on both surfaces. The authors concluded that this phenomenon might be indicative of phase separation of the two distinct polymer species on the NP surface during Langmuir–Blodgett assembly.[86] Detailed investigations into the behavior of mixed brushes can be undertaken when the polymers are grafted to a flat surface, which allows investigation via AFM.[87] Again, conformational changes in the polymer brushes allow the surface to adapt to its solvent environment, but it is interesting to notice that these conformational transitions can be kinetically locked when long enough chains cover shorter ones and thus prevent their swelling by a selective solvent.[87]

For cases where mixed brushes are randomly distributed over the surface or grafted as diblock copolymers at their block junctions, it was shown that the chain conformations can flexibly adapt to global changes in the environment. These observations were made by studying mixed brushes on NPs and lead to the question of whether such phenomena can be made useful for NP assembly.[88] When mixed brushes of thiol-terminated poly(ethylene glycol) (PEG) and PMMA from SI-ATRP are present on large (42 nm) gold nanocrystals, the hybrid particles proved stable as unimers in common solvents for both brushes (DMF, chloroform, DMSO). However, when the solvent was changed by addition of water and subsequent dialysis, these nanohybrids aggregated, probably as a result of formation of hydrophobic domains of collapsed PMMA chains that act as contacting areas for different particles. Interestingly, NP assembly led to a huge proportion (> 60%) of NP dimers. It was speculated that this is caused by depletion of PEG brushes from the dimer junction. The resulting

accumulation of PEG brushes in the noncontacting areas leads to stabilization of the dimer structures (Figure 1.4). This explanation is consistent with the observation that an increase in the PMMA fraction (PMMA:PEG ratio increase from 4:3 to > 5:1) results in the formation of larger multimers upon addition of the selective solvent water.[88] Assemblies of nanocomposites into larger vesicular structures comprising several particles with mixed brushes can also be realized: AuNPs (14 nm) and nanorods (aspect ratio 4:1) were covered with thiol-terminated PEG (grafting-to) and thiol-terminated ATRP initiator, which allowed the growth of PMMA and PMMA-*stat*-poly(vinylpyridine) (PVP). Film rehydration of these nanocomposites led to vesicular structures. These structures were shown to decompose under heat or decreased pH, since vinylpyridine (VP) renders the system pH-responsive. In the case of nanorods, decomposition can be triggered with NIR radiation.[89] These features render this system promising for delivery and controlled release of therapeutic agents.[90,91]

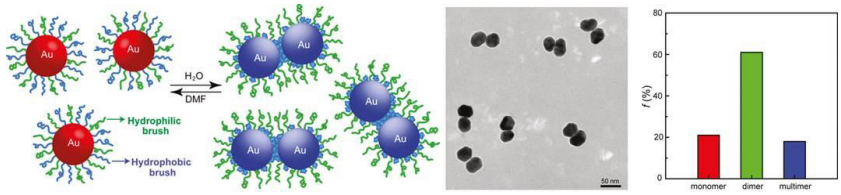

Figure 1.4 The schematic presentation on the left hand side shows the proposed mechanism of dimerization upon solvent exchange to a selective solvent. The image in the middle is a TE micrograph showing AuNP dimer structures, and the histogram on the right hand side shows the fraction of monomeric, dimeric, and multimeric AuNP species. Adapted with permission from ref. 88. Copyright 2011 American Chemical Society.

1.4 Linear Diblock Copolymers and Random Copolymers

As a result of the general immiscibility of different homopolymers, diblock copolymers exhibit an inherent tendency to phase-separate and can therefore form a range of ordered structures in solution and in the molten state. Thus, there has been a lot of research using diblock copolymers in conjuncture with NPs and aiming to use these polymers as templates to form tailored NP arrangements. Block copolymers are attractive in the realm of nanocomposites because each of the two blocks can be employed for distinct functions. For example, for block copolymers grafted to IONPs, the inner block can be used as an attachment site for the incorporation of

chemical tags, while the outer block provides solubility in the respective dispersant.[92] Alternatively, block copolymers can be designed such that one entire block induces NP formation through gold salt reduction and shielding of the formed NP surface, and the second block provides colloidal stability. Following this idea, block copolymers of *N*,*N*-dimethylaminoethyl methacrylate (DMAEMA) and 2-(methacryloyloxy)ethyl phosphorylcholine (MPC) were prepared by ATRP. Addition of $HAuCl_4$ lead to the accumulation of gold close to the DMAEMA repeating units as a result of the formation of salt bridges. The (unprotonated) tertiary amine then acts as reduction agent, which induces AuNP formation. Nanohybrids with an inner shell of PDMAEMA and an outer shell of PMPC are thus formed. Away from its isoelectric point, the PMPC layer imparts solubility to the nanocomposites. It was also shown that there is an optimum PDMAEMA block length for obtaining well-defined spherical AuNPs with reasonably narrow particle size distributions.[93] A more recent work employed the concept of gold salt reduction by one entire block of a block copolymer in an even more sophisticated fashion. Polymers comprising hydrophilic and hydrophobic blocks were used to coat AuNPs, which allowed growth of a gold nanoshell around these hybrid particles.[94] This became possible by introducing phenol side chain moieties into the hydrophilic block, which at basic pH were effective reducing agents for $KAuCl_4$, producing the gold shells. The hydrophobic blocks act as spacers in this case, which allows tuning of the thickness of the obtained nanogap between the gold core and shell, and also permits introduction of Raman tags by copolymerization with a functional monomer. The block that interacts with the NP surface does not necessarily be chemically bound; physisorption of copolymers on NPs can lead to uniform polymer films.[95] It was demonstrated that hydrophobically functionalized AuNPs can be incorporated into micelles from PS-*block*-poly(acrylic acid) (PAA) copolymers by inducing micelle formation through addition of a selective solvent (water) and subsequent crosslinking of the outer shell of the micelle,[96] or by cooling the solution to slowly decrease the critical micelle concentration.[97] In general, large excess of diblock copolymer (which can be separated after NP encapsulation) and a relatively large diameter of the NP (> 10 nm) are necessary to avoid the incorporation of multiple NPs into one micelle. This has been observed for small NPs (< 10 nm) which act as solutes swelling the micelle core.[98] In fact, the number of small NPs contained in a micelle can be controlled by adjusting the ratio of particles and block copolymers, with a higher average number of incorporated NPs being obtained as their relative proportion in the reaction mixture increases.[99]

Triggered assembly of temperature-responsive diblock copolymers was

used by McCormick and coworkers for colloidosome formation.[100] Block copolymers of DMAEMA and N^{i}PAAM were prepared by RAFT polymerization. Heating of a block copolymer solution induced reversible vesicle formation as a result of the collapse of the PN^{i}PAAM block. Addition of $NaAuCl_4$ to the assembled block copolymer solution at a fixed ratio at 50 °C led to incorporation of gold salt in the vesicles. The tertiary amine group of the DMAEMA repeating unit triggered gold reduction and AuNP formation. Interestingly, the vesicular structure was fixed after cooling and did not dissociate into monomeric block copolymers, as observed before AuNP formation.[100] In addition, the morphology of the self-assembled structures can be varied from simple micelles, mixtures of worm-like micelles and spherical micelles, and vesicles by adjusting the degree of polymerization of the temperature-responsive PN^{i}PAAM block in the preceding RAFT polymerization.[101] Preformed NPs can be incorporated into self-assembled solution structures of block copolymers depending on the specific interactions between the NP surface and both blocks. The NP–block copolymer interaction can, for example, lead to NPs being incorporated into micelle cores, although the constituent block copolymer alone forms vesicles. This is so because NP incorporation into the solvophobic phase can reduce the polymer stretching penalty in the self-assembled structures formed.[102] This point is further illustrated in a study[103] by Park and coworkers, which showed that PS-coated quantum dots were incorporated into the PS domain of micelles formed from PS-*block*-PAA polymers. On the other hand, when alkyl-coated particles were employed, they formed a layer between the PS–PS interface.[104] This was shown to occur because the alkyl–PS interaction is the least unfavorable interaction and the incorporation of a NP layer reduces polymer stretching.[103] Thus, two NPs with different surface chemistries can be incorporated at different positions in the polymer matrix. The NP– copolymer interaction can also be tuned such that the NPs assemble at the PS–PAA interface of the micelles formed (by carefully choosing the surface chemistry of the NP).[21] Hence, layered co-assemblies can be obtained with two types of particles located at the PS–PS and PS–PAA interfaces, resulting in different radial positions for the individual NPs (Figure 1.5).

We have seen so far that enthalpic interaction parameters are often crucial in controlling the position of NPs in block-copolymer assemblies.[21,96–99,101–104] Nevertheless, it has been shown impressively that the contribution of entropy to the free energy can become important in controlling the position of NPs in vesicular structures.[105] The co-assembly of NPs decorated with PS-*block*-poly(ethylene oxide) (PEO) copolymers and free (not surface-bound) block copolymers of the same type leads to vesicles with the NPs

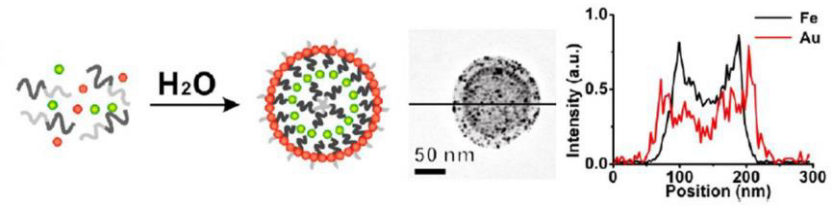

Figure 1.5 Solvent-induced formation of layered assemblies from block copolymers of PAA and PS and AuNPs functionalized with mercaptoundecanol as well as IONPs functionalized with oleic acid. The AuNPs (red) are located at the PS–PAA interface, while the IONPs (green) are located at the PS–PS interface. The graph shows different radial positions for the NPs. Adapted with permission from ref. 21. Copyright 2013 American Chemical Society.

being incorporated in the (solvophobic) PS domain. Interestingly, depending on the number of monomeric repeating units in the two blocks for both free and bound block copolymers, the NPs were either evenly distributed over the entire PS layer or they separated. This separation led to an accumulation of NPs in some areas, leading to "patchy" vesicles, or—in cases of strong separation—to an accumulation on one hemisphere (and depletion on the other), leading to Janus-type structures (Figure 1.6).

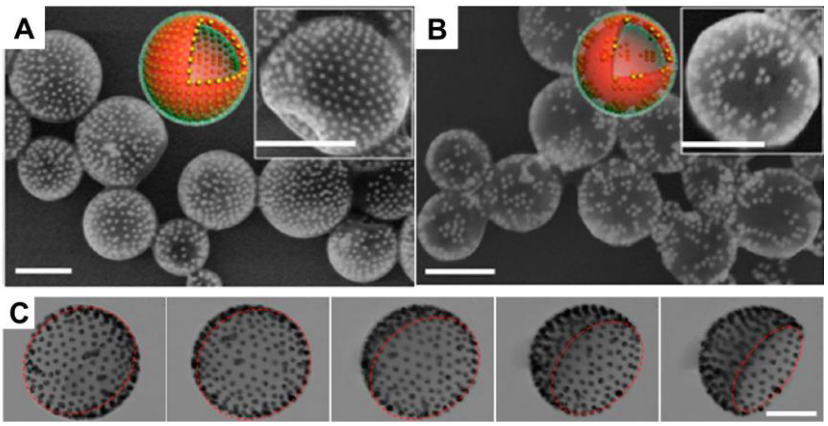

Figure 1.6 SEM images showing AuNPs grafted with block copolymers incorporated in vesicles and evenly distributed in one layer (A) and partly separated in clusters in this layer (B). TE micrographs at different tilt angles reveal fully separated AuNPs in one hemisphere of the vesicle (C). Scale bars: 200 nm (A, B) and 100 nm (C). Adapted with permission from ref. 105. Copyright 2014 American Chemical Society.

The concept of block copolymers acting as templates that can host NPs at defined locations can also be adopted to produce thin films. Thus, block copolymers, which show phase separation in the molten state, can be used

as matrices for selective incorporation of particles. Depending on the block composition and the temperature-dependent block interaction, phase separation can lead to different nanostructured morphologies.[106] However, the discussion is herein restrained to the most common type of phase separation, lamellar phase separation, as an illustrative example. The lamellar type of phase separation also has the advantage that, as a result of its symmetry, it facilitates prediction of NP localization in diblock copolymer hosts. A theoretical study evaluating NP distribution in copolymer melts found that neutral NPs lead to a Gaussian distribution centered at the lamellar interfaces, whereas strongly selective NPs are incorporated in the preferred domain, with a Gaussian distribution centered at the middle of this domain.[107] There could also be intermediate situations in which Gaussian distributions with distinct shoulders are observed. Generally, large degrees of polymerization in the diblock copolymer, and therefore a high degree of domain segregation, were shown to lead to narrow particle distributions in this theoretical work,[107] a finding that is, however, contrary to an experimental study investigating this effect.[108]

Depending on the wetting behavior of the two blocks of the block copolymer with the surface, thin films can show phase separation that is either parallel or perpendicular to the surface. If the surface comprises equal wettability for both blocks, this usually results in perpendicular phase separation. This effect can be nicely demonstrated by comparing two types of NPs, one of which is selective and one of which is neutral for a common block copolymer of PS and PMMA. It can be demonstrated experimentally that selective AuNPs locate inside the favorable block domain, whereas neutral NPs are located at the domain interfaces (see Figure 1.7),[22] fully consistent with theory[107] and other experimental studies.[109,110] It was furthermore shown by cross-sectional TEM that selective NPs are distributed throughout the respective domain, but within the entire film thickness, whereas neutral NPs reside preferentially close to the surface–air interface for entropic reasons.[22] The attraction of NPs to the surface of the substrate thus induces a change in the surface wettability properties and results in conversion from parallel to perpendicular phase separation when the amount of neutral NPs is high enough. A similar transition of block copolymer orientation after addition of NPs to the system has also been observed by others, employing a different system comprising a PS-*block*-PVP copolymer together with alkyl-coated CdSe particles.[111,112] To take full advantage of the periodical features present on the surface of phase-separated thin films, one could also choose to further swell specific domains with selective solvents prior to the addition of particles[113] or to permanently fix the phase separation by photo-crosslinking.[16]

By adding NPs to phase-separating block copolymer systems, one may also face phenomena resulting from interparticle interactions, which are often neglected by theory: When lamellar phase separation is used to introduce magnetic NPs functionalized with PMMA into the PMMA domain of a PS-*block*-PMMA copolymer, the incorporation can occur only at small NP concentrations. When the NP concentration is high enough, the polymer-coated NPs tend to form particle aggregates that are too large to be taken up inside one block domain, and therefore block copolymer assembly around these aggregates is observed.[114] A different scenario that can be observed upon increasing the NP concentration is an NP-induced phase transition. An interesting mechanism leading to phase transition in block copolymers has been described by Kramer and coworkers.[115] When NPs, which prefer to locate at block interfaces, were added with increasing concentration, the authors found that initially the domain size in lamellar phase-separated block copolymers decreased. This behavior was rationalized by strong segregation theory, predicting a scaling of domain thickness proportional to the block copolymer interfacial energy, which is decreased by addition of neutral NPs locating at the copolymer interfaces. Further increase in the NP concentration led to a lamellar-to-bicontinous transition, as shown for AuNPs selective for an interface with two different surface coatings. The effect of the molar mass of the block copolymer matrix on the phase transition was also studied and it was found that matrices with higher molar masses required smaller NP concentrations for phase transition.[115]

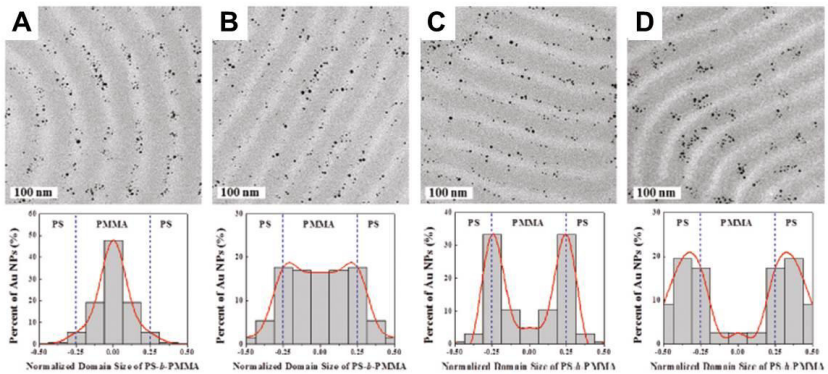

Figure 1.7 TEM images (top row), which show the lamellar phase separation of a PS-*block*-PMMA polymer perpendicular to the substrate surface (PS domains occur darker as they were stained with RuO_4) and the distribution of AuNPs modified with different polymeric ligands (the fraction of styrene increases from A to D). The diagrams in the bottom row show the particle distributions in the block copolymer domains for AuNPs coated with the four different polymers. Adapted with permission from ref. 22. Copyright 2011 American Chemical Society.

1.5 Linear Triblock Polymers

By applying triblock terpolymers as templates for the *in-situ* formation of NPs, it is possible to introduce even more information into a linear polymer by using the different blocks for distinct functions. For example, two outer blocks can be chosen such that the resulting polymer has a tendency to self-assemble into specific solution structures, while the inner block can comprise binding sites for NPs;[116,117] alternatively, one outer block can provide these binding sites and the other two blocks can provide amphiphilicity.[118,119] Such triblock terpolymers are, for example accessible through consecutive RAFT[116,117] or ATR[118,119] polymerizations. When an inner block of either PMAA[116] (providing attachement sites for the complexation of an iron salt precursor) or PDMAEMA[117] (providing attachment sites for tetrachloroauric acid) is sandwiched between outer blocks of PS and poly(oligo(ethylene glycol) methacrylate) (POEGMA), the polymers can be used to organize inorganic NPs into different patterns. Polymerization-induced self-assembly was employed in both of these studies; that is, the respective block copolymer precursors were used as macroRAFT agents in chain extension polymerizations with styrene in methanol, under which conditions polymeric NPs were formed. The two different inorganic precursor salts could then be introduced into the respective middle block of the triblock terpolymers, and inorganic particle formation could be triggered by adding base to form IONPs[116] or reduction agent to form AuNPs.[117] Depending on the degree of polymerization of styrene, this system can be tuned to form micelles, rods, and vesicles as hosts for inorganic NPs.[116] The polymers therefore encode these different solution structures and at the same time carry information about where the inorganic NPs will be placed in the resulting nanohybrid assembly structures.

The studies mentioned above followed the approach to first assemble specifically designed polymers and then induce NP formation after assembly formation. In principle, however, it should be possible to first decorate inorganic NPs with a polymer to create amphiphilic hybrid particles, which can then assemble into a variety of structures. This has been realized by Eisenberg and coworkers.[120] Their approach used triblock polymers made by two successive ATR polymerizations of first styrene and then VP, starting from a chloride-terminated PEG macroinitiator. The resulting PEG-*block*-PS-*block*-VP polymers were used to cover AuNPs and PdNPs via attachment through the PVP block. The obtained hybrid particles had amphiphilic character and tended to assemble into micellar structures after addition of water to their dispersions in THF. The self-assembled

structures revealed (by TEM characterization) NPs with defined location at the surface of the micellar core. The defined NP position resulted from the covalent attachment of the separating blocks. The hydrophilic PEG block could effectively stabilize these micellar structures in the hydrophilic environment at high enough grafting densities.[120]

Even higher precision in the formation of nanocomposites can be achieved by the ambitious procedure of NP monofunctionalization.[121] Liu and coworkers indeed found that small AuNPs can be functionalized with only a single macromolecule, a triblock terpolymer.[122] The authors used a macroRAFT agent with PEG in its RAFT leaving group ("R group") to successively polymerize glycidyl methacrylate (GMA) and styrene. The middle PGMA block was used to introduce lipoic acid, which acts as an anchor for gold surfaces via its dithiolane moiety. By analyzing the nanohybrids of this polymer with AuNPs via size-exclusion chromatography (SEC) and thermogravimetric analysis (TGA), it was concluded that indeed only one macromolecule attaches to AuNPs with diameters of ~2.0, ~2.9, and ~3.8 nm. Monofunctionalization was, however, not observed for AuNPs of ~4.9 nm, strongly suggesting a size selectivity for this stoichiometric functionalization. The nanocomposites with one macromolecule per inorganic particle were decorated with a PEG and a PS chain (the outer blocks of the initial triblock polymer) and can therefore be considered as true amphiphilic particles. The assembly of these nanohybrid particles into vesicles and micelles, depending on the packing parameter (which can be controlled by macromolecular design) has been demonstrated (Figure 1.8).[122]

In addition to the above-discussed cases of triblock terpolymers, linear triblock polymers can also take the form of ABA copolymers. A recent study[123] employed a symmetric ATRP macroinitiator with a PEG linker between the two initiation sites. ATR copolymerization of diethylenegylcol methylmethacrylate (DEGMMA) and diethyleneglycol ethylmethacrylate (DEGEMA), together with a comonomer for fluorescent labeling, permitted the formation of outer blocks with defined lower critical solution temperature (LCST). Silica NPs were surface-functionalized by SI-ATRP with polymers of different compositions of DEGMMA and DEGEMA to tune the LCST of the surface-grafted polymer and another comonomer as fluorescent tag. The fluorescent labels were introduced to study the spatial relation of the surface-modified SiNPs with the outer blocks of the triblock ABA copolymer. When the polymer immobilized on the SiNP surface had a similar LCST as the outer blocks of the triblock copolymer, mixtures of both species formed gels at a temperature above their common LCST. In these gels, the NPs were localized in micellar compartments of the collapsed outer A blocks of the ABA copolymer. Gel formation was a result of the

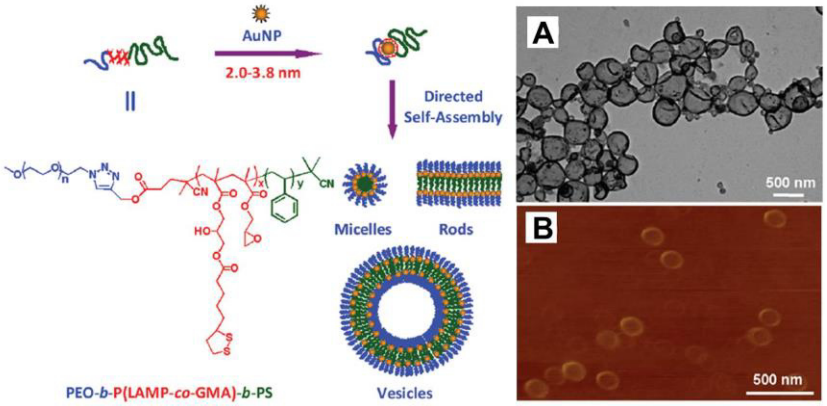

Figure 1.8 Schematic representation of the strategy employed for the monofunctionalization of AuNPs with one macromolecule and HRTEM (A) as well as AFM (B) images of the vesicular assembly structures obtained from these nanohybrids. Adapted with permission from ref. 122. Copyright 2012 American Chemical Society.

bridging of (soluble) PEG chains (B block of the ABA copolymer) between the collapsed entities. When the SiNPs were modified with a polymer of higher LCST than that of the outer block of the triblock copolymer, gels were formed at temperatures intermediate between the two LCSTs and SiNPs were not incorporated into the collapsed micelles. Careful manipulation of the properties of the surface-bound polymers therefore allows control of the location of inorganic NPs in organic polymer gels.[123]

1.6 Linear Multiblock Polymers

RAFT polymerization is unique among the most prominent RDRP techniques because the inherently bifunctional TTC group can be employed in RAFT-type chain transfer agents. As a result of this bifunctional nature, the TTC moiety can be easily incorporated into the backbone of linear multifunctional RAFT agents[124,125] or cyclic RAFT agents,[126] both of which permit the formation of multiblock polymers with narrowly distributed block lengths. In such systems, the RAFT mechanism causes a continuous redistribution of all blocks and RAFT groups during polymerization and this results in remarkably narrow ideal block distributions.[127] Consequently, such macromolecules are relatively well-defined and can thus be used as the tailored organic part of nanohybrids with inorganic particles. For AuNPs, this polymer comprises TTC groups as gold attachment points in its backbone.[128] Another advantage of these systems is that multiblock

copolymers can be obtained by only two successive polymerizations. Such multiblock copolymers can be useful, as shown by Du *et al.*, who suggested that amphiphilic RAFT multiblock copolymers of styrene and VP can be used for the interfacial assembly of AuNPs, gold nanorods (AuNRs) and AgNPs at liquid–liquid interphases.[129] The authors did not show, however, whether the TTC groups are maintained in the multiblock copolymers after treating them with $NaBH_4$ during the *in-situ* synthesis of AuNPs and AgNPs.

When the covalently linked blocks of a multiblock polymer are made of N^iPAAM monomer, the resulting polymeric material is water soluble and can therefore be brought directly into contact with AuNPs from citrate-reduction. Nanohybrids produced by this method were analyzed by TEM, which showed particles that assembled in hexagonal two-dimensional patterns with constant minimum spacing between the gold cores; absolutely no particle stacking was observed.[71] This indicates that the gold cores were not cross-linked by the multifunctional RAFT polymer, a result that was confirmed by SEC. The binding mode of this polymer on the surface of this type of AuNP could be revealed in even more detail: The spacing between the gold cores was analyzed systematically for different multiblock polymers of N^iPAAM and compared with the data (see Section 1.2, Figure 1.3) obtained for linear polymers of N^iPAAM with only one TTC group on the ω-end of the polymeric chain. It was found that gold core spacings were distinctively smaller and almost constant when multifunctional RAFT polymers with varying block numbers and degrees of polymerization were employed for surface functionalization reactions with these AuNPs. This leads to the conclusion that this type of polymer attaches to AuNPs from citrate-reduction in a multivalent fashion via its multiple TTC groups, meaning that these macromolecules wrap around the AuNPs and form polymer loops on the NP surface.[71]

1.7 Branched Polymeric Architectures

Branched polymers are fundamentally different from linear polymers, which were discussed in previous sections: Polymers of linear topology contain two end groups, whereas multiple end groups are present in branched architectures, which allows incorporation of multiple functional groups into macromolecules of globular shape. Branched polymers can therefore be considered as promising macromolecular NP linkers. The branching points can be statistically distributed over the macromolecules (hyperbranched polymers, HBPs), occur strictly regularly leading to generational structures

(dendrimers), or the branches can be joined at a common core (star polymers).

Branched polymers can still attach to surfaces via one or multiple branches. It is possible to attach an HBP to an inorganic particle with only one of its branches if when an ATRP initiator is immobilized on a surface, followed by polymerization of an initiator–monomer.[130] HBP with multiple anchor sites for NPs was prepared by Fredericks and coworkers,[131] who produced hyperbranched RAFT polymer by copolymerization with a difunctional monomer. The RAFT agent was of the TTC type and also contained an alkyne moiety in its R group; both functional groups are known to attach to gold surfaces. Addition of these polymers to AuNPs from citrate-reduction resulted in the formation of nanohybrid particles with unbound TTC and alkyne groups on their surfaces. These available functional groups could be used for the attachment of citrate-capped AuNPs, resulting in cross-linked AuNP nanoassemblies. In a subsequent study[132] by the same authors, it was shown that the structure of these assemblies varies with the macromolecular architecture of the HBP: With low numbers of branches (and consequently a low number of anchoring sites for gold), the nanoassemblies showed a plate-like morphology, whereas for a higher number of branches, globular assemblies with densely packed AuNPs were found. Because the approach introduced in these studies allows the attachment of further particles to a nanohybrid particle scaffold, it could also allow the attachment of particles of a different type to this scaffold architecture, leading to hierarchical multicomponent nanostructures. Such nanostructures can be realized using this approach by treating larger (48 nm) citrate-stabilized AuNPs with HBP to create nanohybrids acting as the scaffold, and then adding smaller (15 nm) citrate-capped AuNPs after purification of the initial nanohybrids.[133] The approach resulted in the formation of core–satellite nanostructures; varying the stoichiometric ratio of the two types of inorganic particles employed could control the average number of satellite particles in these arrangements.

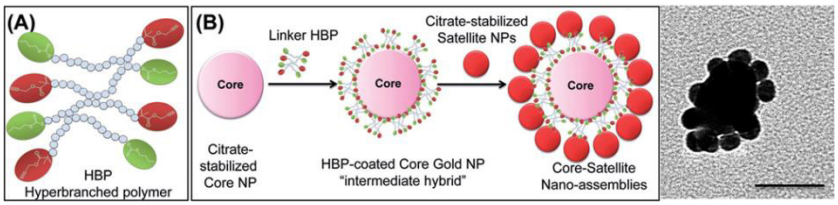

Figure 1.9 Schematic representation of the hyperbranched polymers (A) used for the synthesis of core–satellite particles (B) and a corresponding TE micrograph (scale bar: 50 nm). Adapted with permission from ref. 133. Copyright 2014 Royal Society of Chemistry.

1.8 Conclusions

We have seen in Section 1.2 that nanocomposites with distinct functional groups repeatedly presented on the surface can be used for specific interactions, which can lead to applications such as targeting of carcinoma cells. The length of the surface-bound polymer can be used to encode interparticle spacing in two- and three-dimensional assemblies, with possible applications in material science. Also, the scaling of particle distances with the molar mass of surface-anchored polymer contains information about the conformational state of the polymer at the surface. The set of parameters, which determines the architecture of polymers in nanocomposites, can be drastically expanded when two types of linear homopolymers are used instead of one (Section 1.3). In such situations, phase separation phenomena can be observed on the surfaces of colloidal particles, and we have seen how this phase separation can be modulated by the design of the employed macromolecules. The tendency of two different polymers to separate can also be exploited by covalently linking two immiscible homopolymers (i.e., by preparing diblock copolymers, as described in Section 1.4). By carefully adjusting its architecture, this type of polymer can be used to precisely control the location of inorganic NPs in a molten or solution state. Related to this is the case of triblock polymers presented in Section 1.5, whereby additional functionality can be imparted to the macromolecules through introduction of the third block. By further increasing the block number (i.e., creating multifunctional polymers, as discussed in Section 1.6), it is possible to encode polymer loops at surfaces. The branched polymeric architectures presented in Section 1.7 can also be considered as multifunctional polymers, but with a different topology from linear multiblock polymers. It was shown that it is possible to prepare higher-order assemblies including two different types of NPs by employing a hyperbranched polymeric linker through controlled radical polymerization.

The work done during the last decade and reflected in the literature summarized in this chapter therefore suggests that specifically designed macromolecules contain information that can be translated to the structure of nanohybrids and self-assembled structures. The encoding of this information with macromolecules becomes possible through macromolecular design by means of controlled radical polymerization. Thus, macromolecular design via controlled radical polymerization can be considered as a versatile programming language[134,135] to guide nanocomposite formation and assembly.

This thesis will follow this central idea and will focus on the development

of RAFT-based systems for assembling AuNPs in a rational and predetermined fashion. AuNPs are chosen as building units as a consequence of their chemical stability and facile surface modification. The systems for the controlled AuNP arrangement which had been developed within this thesis are presented in Chapters 3 and 4. Before we proceed to the discussion of these systems, the following Chapter 2 will deal with some general aspects of the specific interactions involved in nanohybrids of RAFT polymers with AuNPs.

Chapter 2

Model Systems for Aspects of the Interaction of RAFT Polymers with Gold Nanoparticles[2]

2.1 Structural Aspects

Self-assembled monolayers of thiols on gold surfaces are long-established in chemistry.[136] Based on this, the immobilization of thiol-terminated polymers on AuNPs via the 'grafting-to' strategy has become a practical approach toward polymer-coated AuNPs.[22,72,137–139] Insights into the binding of thiols on AuNP surfaces had been obtained from single-crystal structure determination in thiolated gold nanoclusters, composed of up to 133 gold atoms.[140–146] These small nanoclusters can serve as a model for the larger AuNPs; a typical binding motif for the thiol-sulfur in these crystal structures is the bridging of two Au centers through the sulfur atom. Key to the successful formation and crystallization of thiolated gold nanoclusters is the use of conformationally rigid thiol ligands. *N*-heterocyclic carbene based ligands are even capable of stabilizing mononuclear gold(0) species,[147] which may be whimsically considered as the smallest possible AuNPs.

In 2006, Duwez *et al.* have demonstrated via X-ray photoelectron spectroscopy that small molecule thiocarbonyl thio compounds show affinity toward flat gold surfaces,[32,33] and thereby hatched out the direct application of RAFT polymers as AuNP coatings, without prior end-group

[2]Adapted with permission from Rossner, C.; Roddatis, V.; Lopatin, S.; Vana, P. *Macromol. Rapid Commun.* **2016**, *37*, 1742–1747. STEM-SI Analysis was performed by Sergei Lopatin and Vladimir Roddatis; Crystal Structure Analysis was undertaken by Alexander Paesch and Peter Stollberg.

modification. The authors further concluded that the thiocarbonyl thio group attaches via two sulfur atoms to gold surfaces, as depicted in Figure 2.1A. Further evidence for the attachment of small molecule dithioesters to AuNPs was later found by Blakey *et al.*,[148] who deduced the presence of such interactions from UV/visible extinction spectroscopy (see also Section 2.2) and from Raman measurements. These Raman data, however, seem to indicate that the binding of the dithioester compounds studied is monodentate through the thiocarbonyl sulfur atom (Figure 2.1B).

Considering the literature-known details about the structure of RAFT groups interacting with gold surfaces, there remain two critical questions not answered: (i) Can the binding of the RAFT group to gold also be proven for polymeric species with RAFT end groups? (ii) What is the exact binding mode of RAFT groups to gold surfaces: monodentate, bidentate, or can both binding modes occur? To address these questions, new model systems had been developed within this work.

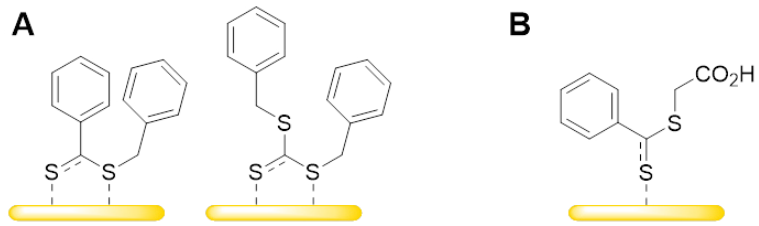

Figure 2.1 Representation of conceivable binding modes of small molecule RAFT agents on gold surfaces as proposed by Duwez *et al.*[32] (A) and Blakey *et al.*[148] (B).

Firstly, it was intended to employ electron energy loss spectroscopy (EELS) in a transmission electron microscope to resolve the lateral distribution of elements within samples of polymer–gold nanohybrids. Recent advances in this field have demonstrated the capability of such techniques to map light elements in the environment of inorganic nanoparticles. In particular, energy-filtered transmission electron microscopy (EFTEM) has been used to map sulfur in sulfurized palladium nanoparticles.[149] Here, specifically, it was sought to map the location of sulfur-containing polymeric end groups. For this purpose, a linear RAFT polymer of N^{i}PAAM ($M_n = 49$ kg mol^{-1}, $Đ = 1.18$) was synthesized and immobilized on AuNPs from citrate-reduction, forming core–shell particles.

Figure 2.2A displays a scanning transmission electron microscopy (STEM) dark-field image of such core–shell particles after drop-casting from colloidal dispersion. Although the polymer shell does not contribute

strongly to the contrast compared with the gold cores, the presence of distinct gold core spacings is indicative of a surrounding polymer layer.[71] Fine-structural analysis of this polymer shell by scanning transmission electron microscopy and spectrum imaging (STEM-SI) was attempted, disclosing distribution of carbon and sulfur (Figure 2.2B and 2.2C).

Two major results can be obtained from such analysis: (1) Sulfur is always co-localized with the gold cores. This result obtained for trithiocarbonate-containing polymers agrees with earlier observations for small molecules on gold surfaces discussed above and can be considered as a microscopic indication for the claim that RAFT polymers attach to AuNPs with their sulfur-containing ω-end. (2) Considering the lateral distribution of carbon, there appears to be a distinct ring present around AuNP cores (see white arrows in Figure 2.2B), with much carbon contributing to electron scattering in that region. This particular result is consistent with earlier AFM[52,53,150] and SEM[72] findings in two-dimensional arrays of polymer-coated nanoparticles which indicate that the height of the polymer shell is of comparable size to the gold core only in regions close to the core and decreases in regions more remote from the core. Moreover, also recent EFTEM experimental data[151] for polymer brushes on silica nanoparticles show similar results.

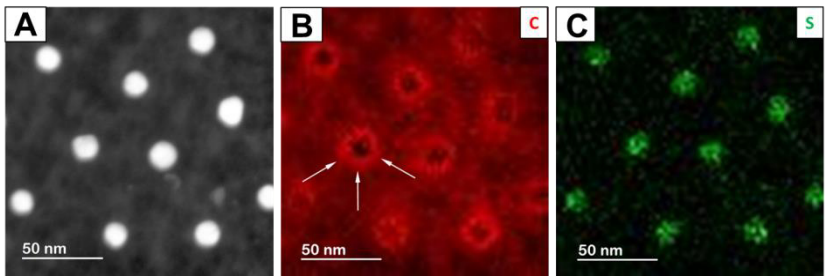

Figure 2.2 STEM dark-field image (A) of core–shell particles with a corona of linear TTC-terminated PN^{i}PAAM. Images (B) and (C) are obtained via STEM-SI and show maps of the elements: carbon (red) and sulfur (green), correspondingly.

In order to obtain further insights into the exact binding mode of the RAFT group to gold surfaces, it was attempted to examine the crystal structure of gold nanoclusters covered with small molecule TTCs. Initial trials to reduce a gold(III) salt precursor in the presence of RAFT agent **2** (see Figure 2.5 in the following section for the structure) and subsequent attempted crystallization did not yield crystalline product. Because the formation of ligand-stabilized gold nanoclusters from a gold(III) precursor is a very

complicated reaction and it is hard to rationally adjust to optimum reaction conditions, it was decided to try to isolate intermediates toward TTC-ligand-coated gold nanoclusters. A plausible intermediate is a gold(I) species with TTC ligand attached. Such compounds are accessible by reducing hydrogen tetrachloroaurate(III) by tetrahydrothiophene[152] and subsequent ligand exchange with a TTC ligand.[153] Using dibenzyl trithiocarbonate instead of **2** in this ligand exchange, yellow needles of chloro(dibenzyl trithiocarbonato) gold(I) could be obtained. The crystal structure of this complex (Figure 2.3) features dimers that assemble in an antiparallel fashion, held together by aurophilic interactions.[154] The gold atoms are linearly (177.0°) coordinated by the sulfur and chlorine atoms. It is notable that the Au–Au separation in this complex (3.17 Å) is close to the distance of gold atoms in cubic closed-packed gold metal (2.89 Å).[154] The Au–Au distance also compares well to a value determined for a comparable structure, which however featured a cyclic TTC (3.08 Å).[153] The S–Au distance is 2.27 Å, which is also very close to the value obtained for the literature-known structure with the cyclic TTC (2.29 Å).

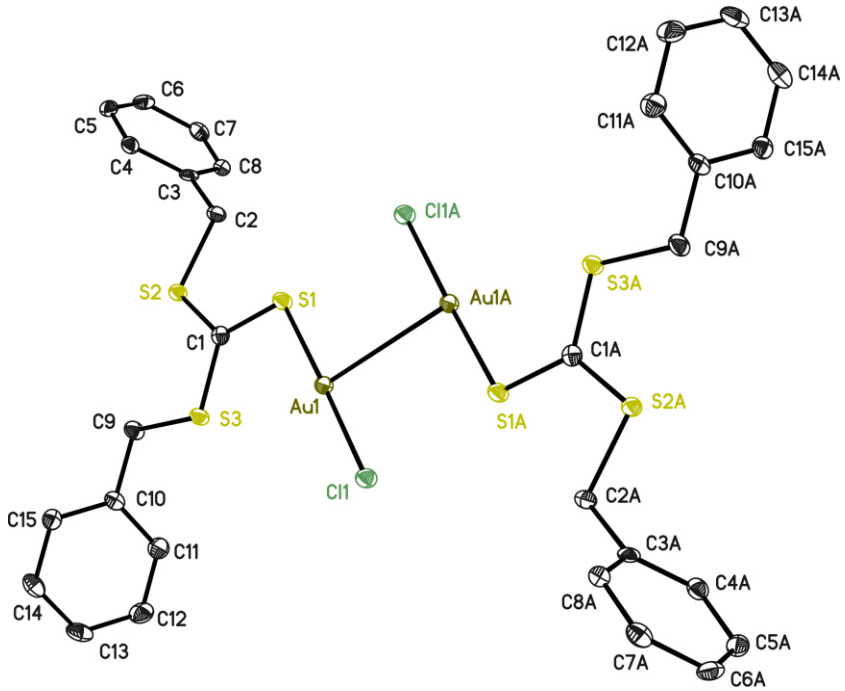

Figure 2.3 Single-crystal X-ray structure of chloro(dibenzyl trithiocarbonato) gold(I). Anisotropic displacement parameters are depicted at the 50% probability level. Hydrogen atoms are omitted for clarity.

It appeared worth trying to remove the chloride substituent and thereby opening another coordination site at the gold. Gold(I) centers can in principle dimerize through so-called "semi-supported"[155] as well as "fully-supported"[156] aurophilic interactions, in which one or more ligands, respectively, give rise to a μ-bridging of the Au(I) centers, even when the positive charges are not balanced with a coordinating anion or anionic ligand. Following this idea, the coordinating chloride anion was exchanged with the noncoordinating hexafluoroantimonate(V) through reaction with $AgSbF_6$.

The crystal structure of the product revealed Au(I) centers linearly coordinated by the dibenzyl trithiocarbonate ligands, without any aurophilic interactions being present. To the best of my knowledge, no similar structure has yet been reported in literature. The two dibenzyl trithiocarbonate ligands that attach to the same Au(I) center can arrange in a *cis* (Figure 2.4A) as well as in a *trans* fashion (Figure 2.4B) with respect to each other. In the *trans* case, the coordination is perfectly linear (180.0°), while it slightly deviates from linearity in the *cis* case (171.5°). The S–Au distance ranges from 2.28 to 2.30 Å, and is therefore slightly larger as in the structure of chloro(dibenzyl trithiocarbonato) gold(I).

As the crystal structure shown in Figure 2.4 does not involve any supported aurophilic interactions, no conclusions about whether TTC groups can bridge two Au(I) centers can be drawn. The only conclusion which can be drawn from this crystal structure is that trithiocarbonates interact with gold(I) centers via Au(I)–S-interaction involving the thiocarbonyl sulfur atom of the TTC moiety.

To better reflect the situation in gold nanoparticles, this compound may be reduced to Au(0) in order to induce Au clustering. From single crystal structure analysis of such TTC-stabilized gold nanoclusters, the question if TTC ligands can bridge two Au(0) centers (as suggested by Duwez *et al.* and schematically depicted in Figure 2.1A) may be finally decided, if these μ-bridges would be found in such situation. Although the crystallization of such TTC-stabilized gold nanoclusters could not be achieved in this work, a synthetic route to a defined precursor for these nanoclusters has been successfully developed, which opens the possibility of systematic trials toward the isolation of monodisperse TTC-coated gold nanoclusters.

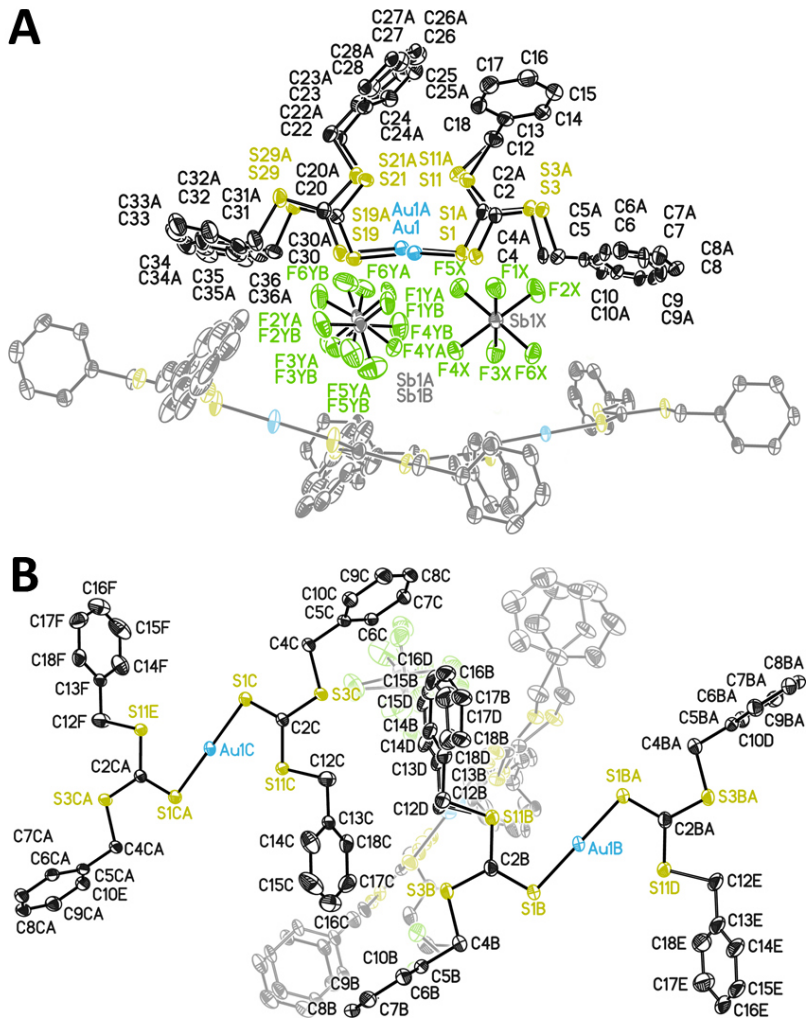

Figure 2.4 Single-crystal X-ray structure of bis(dibenzyl trithiocarbonato) gold(I) hexafluoroantimonate. Cis-coordinated (A) and trans-coordinated (B) Au(I) centers are emphasized in the upper and lower part of the Figure, respectively. Anisotropic displacement parameters are depicted at the 50% probability level. Hydrogen atoms are omitted for clarity.

2.2 Thermodynamic Aspects

Knowledge about the strength of the interaction between anchoring moieties and the surface is of extraordinary importance for understanding the behavior of derived nanocomposites. Concerning RAFT polymers and their nanocomposites with AuNPs, early reports followed a strategy that included the post-polymerization modification of the RAFT polymers sulfur-containing ω-end group into a thiol,[137,157] which was subsequently used as an established anchoring site for the attachment to the gold surface. Only later it was recognized that this end group modification is not necessary for immobilization of RAFT polymers at gold surfaces (see 2.1).[158] When dealing with interactions of organic ligands on surfaces, one has to consider that nonuniform surfaces feature different adsorption sites, which can provoke different adsorbate binding energies.[159]

The RS–Au bond formation is well-studied.[136] RS–Au bonds can be formed at the surface immobilizing either disulfides, which occurs via a dissociative mechanism,[160] or thiols, which proceeds through hydrogen release.[161] The RS–Au interaction strength can be shown to be roughly 170 $kJmol^{-1}$,[162] which, together with bond energies of 365 $kJmol^{-1}$ and 435 $kJmol^{-1}$ for RS–H and H_2, respectively,[163] lead to a net energy of roughly −20 $kJmol^{-1}$ (exothermic) for the adsorption of thiols on gold surfaces. Adsorption of disulfides provides an even stronger driving force, reflected in a free enthalpy of adsorption of −100 $kJmol^{-1}$ (or −50 $kJmol^{-1}$ per RS unit, for comparison).[163]

The situation is different for the adsorption of the thiocarbonyl thio group inherently contained in RAFT polymers. There, no covalent bonds are broken during attachment to the gold surface. For the purpose of characterizing the interaction strength, Blakey *et al.* developed a UV/visible spectroscopic experiment that allows the analysis of the Langmuir isotherm of adsorption.[148] From such analysis, the authors obtained a value of −36 $kJmol^{-1}$ (exothermic) for the free enthalpy of adsorption of a phenyldithioester RAFT agent on gold nanoparticles from citrate-reduction. This value may be considered as an estimate for the interaction strength of the phenyldithioester group on gold. One needs to consider, however, that the determined value contains contributions from free enthalpies of dissolution of the adsorbate as well as from the displacement of the primary (citrate and oxidized forms of citrate) ligands. It may therefore be more appropriate to consider this value a lower limit for the dithioester–gold-interaction.

Since RAFT polymers of the trithiocarbonate type are treated in this work,

the interaction of TTCs with gold surfaces was evaluated here following the method of Blakey *et al.* This is important, as the phenyl group is in direct conjugation with the thiocarbonyl group (through which surface attachment occurs) in phenyldithioesters studied by Blakey *et al.*; TTCs are structurally different in this regard. Also, it was intended to perform experiments with two different TTC group-containing model RAFT agents, to disclose a possible influence of the specific model structure used on the result for the free enthalpy of adsorption. Therefore, two model compounds (Figure 2.5) had been synthesized which are designed in order to enable different modes of colloidal stabilization, i.e. steric and electrostatic stabilization.

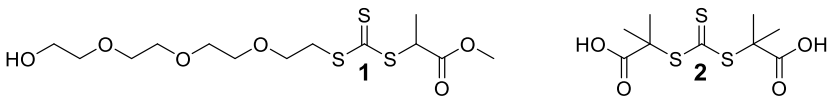

Figure 2.5 Chemical formulas for the two trithiocarbonate-containing model RAFT agents.

The symmetrical RAFT agent **2** with its two carboxyl termini was prepared following an established synthetic procedure[164] and intended as model compound which enables electrostatic stabilization in (basic) aqueous gold nanoparticle dispersions. The interaction of both model ligand compounds with gold nanoparticles from citrate-reduction leads to characteristic optical responses (Figure 2.6). In the case of RAFT agent **1**, its interaction with the gold nanoparticles leads to a decrease in extinction in the UV region and to the emergence of a low energy shoulder of the AuNP plasmon band. The extinction in the UV region mostly stems from interband transitions of the AuNPs,[165,166] which should hardly be influenced by the binding of a ligand to the particle surface. The decreased extinction is much rather a consequence of precipitation of AuNPs after their surface modification; precipitated material was also observed at the bottom of the cuvette. The low-energy shoulder of the plasmon band, on the other hand, can be related to AuNP aggregates still kept dispersed in which plasmon band coupling leads to a shift in the plasmonic frequency.[42] Both observations clearly demonstrate that ligand **1** is not suited to provide colloidal stability to the employed type of AuNPs in aqueous dispersion.

When the AuNP surface is modified with RAFT agent **2**, only subtle changes in the optical behavior are observed: A bathochromic shift of the plasmon band, indicative of the formation of a charge transfer complex upon surface binding of **2**,[148,167] is observed together with the emergence of an absorption band centered around 310 nm, which can be attributed to the π-π^*-transition of the thiocarbonyl thio group in **2**. This π-π^*-transition is

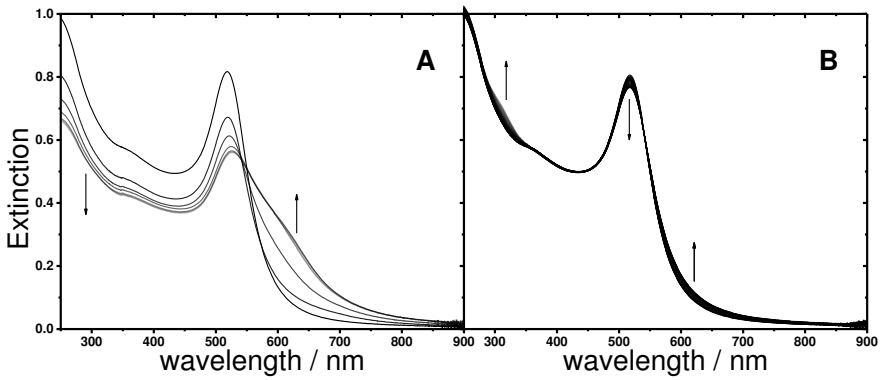

Figure 2.6 UV/visible spectra of gold nanoparticles from citrate-reduction after successive additions of RAFT agent **1** (plot labeled A) and **2** (plot labeled B).

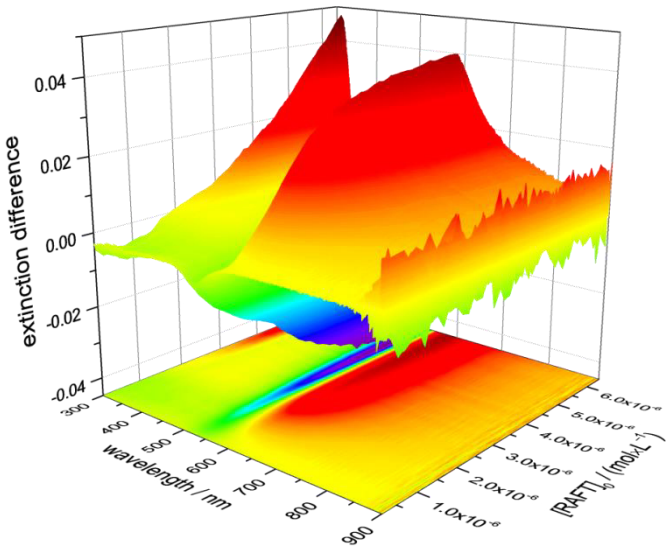

Figure 2.7 Extinction difference spectra obtained by subtracting the spectrum of the starting AuNP dispersion in dependence on the addition of RAFT agent **2**.

bleached upon coordination to the surface,[148] such that the measured extinction stems from nonbound **2** exclusively. To emphasive the subtle spectra changes, difference spectra can be obtained by subtracting the spectrum of AuNPs taken before the first addition of **2** (Figure 2.7). As both the amount of free (not surface-bound) **2** as well as the development of the plasmon band (formation of AuNP–**2** charge transfer complex) can be

followed in one experiment, the data obtained can be used to fit a Langmuir isotherm of adsorption (Figure 2.8):[148]

$$\frac{[\mathrm{RAFT}]}{[\mathrm{Au{-}RAFT}]} = \frac{[\mathrm{RAFT}]}{\Gamma_{\max}} + \frac{1}{K \cdot \Gamma_{\max}}. \qquad (2.1)$$

The here presented study of the adsorption of the model compound **2** following a method developed by Blakey *et al.*[148] suggests a similar free enthalpy of adsorption for TTCs compared to dithioesters (both -36 kJmol^{-1}).

This section can be concluded by noting that dithioesters and trithiocarbonates—functional groups often encountered as end groups in RAFT polymers—feature free enthalpies of adsorption to gold surfaces intermediate between thiols and disulfides, the most prominent functional groups for gold surface modification. This behavior is also reflected in recent work by Haddleton and coworkers, showing by employing microbalance measurements that the density of layers formed on gold through the grafting of oligomers (~5 kgmol^{-1}) with distinct sulfur-containing end groups decreases in the following order: disulfide > dithioester ~ trithiocarbonate > thiol.[168] The authors also found reasonable agreement with this trend in XPS experiments.

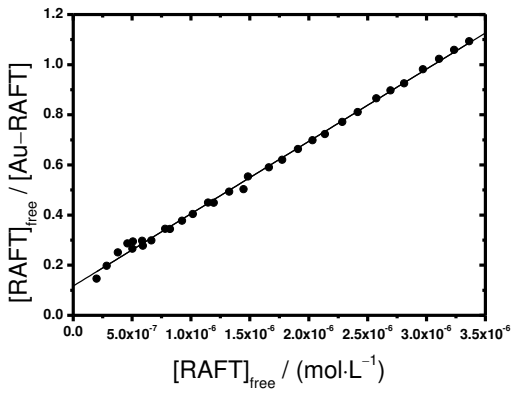

Figure 2.8 Langmuir isotherm of adsorption obtained by adding **2** to AuNPs from citrate-reduction in aqueous dispersion. Experiments were conducted at 21 °C. A fit to equation 2.1 yields an equilibrium constant of $2.5 \cdot 10^6$ M^{-1} for the binding of **2**, corresponding to a free enthalpy for the adsorption reaction of -36 kJmol^{-1}, i.e. 15 $k_B T$ at 21 °C. The analysis is based on an extinction coefficient that has been determined as $\varepsilon^{310\,\mathrm{nm}} = 13100$ Lmol^{-1}cm^{-1} in water for RAFT agent **2** within this work.

Chapter 3

Self-Assembly of Gold Nanoparticles into Superstructures[3]

3.1 Preface

A conceptually very straightforward and easy to implement way of placing NPs into ordered particle arrangements is to follow a strategy of NP self-assembly. In order to differentiate the term "self-assembly" from mere "formation", Whitesides and Grzybowski argued that "self-assembly" should be a tag only for processes in which pre-existing distinct components are involved and which can be controlled by adapting the specific design of these components.[2] AuNPs in particular are extensively studied model NPs for the exploration of strategies for their self-assembly, which is a consequence of their chemical stability and facile surface modification. The formation of AuNP assemblies can be mediated by a variety of distinct interactions, such as salt bridges,[169] hydrogen bonding,[170–172] π-π-interactions,[173,174] metal coordination,[175] dipole–dipole-interactions,[176] halogen bonding,[177] thiol–gold[139,178] and thioether–gold interactions.[179,180] In some cases, superstructure formation can be triggered by applying external stimuli, such as temperature,[170,173] addition of metal cations,[175] or light.[176,181] Other strategies rely on the cross-linking of AuNPs by organic particle linkers.

[3]Adapted with permission from Rossner, C.; Glatter, O.; Saldanha, O.; Köster, S.; Vana, P. *Langmuir* **2015**, *31*, 10573–10582, Copyright 2015, American Chemical Society; from Rossner, C.; Ebeling, B.; Vana, P. *ACS Macro Letters* **2013**, 2, 1073–1076, Copyright 2013, American Chemical Society; and from Rossner, C.; Ebeling, B.; Vana, P. Controlled Radical Polymerization: Materials (ACS Symposium Series) **2015**, *1188*, 293–307, Copyright 2015, American Chemical Society.

To obtain AuNPs in organic dispersants which can thusly be brought directly into contact with organic substances for further surface modification, the Brust–Schiffrin[182] synthesis is arguably the most commonly applied method. In addition to this originally introduced approach where the AuNPs are modified with an alkanethiol *in situ*, it is also possible to conduct the synthesis in the absence of thiols (*ex–situ* approach). While the exact mechanism of the latter is still a topic of research,[183] it is known that it leads to AuNPs with a weakly chemisorbed phase-transfer catalyst (most commonly tetraoctylammonium bromide, TOAB) on their surfaces.[184] TOAB can be easily substituted by competitive ligands,[185] which renders TOAB-capped AuNPs ideal candidates as building units in grafting reactions with functional (macro)molecules that may be used to interconnect these primary particles resulting in nanoparticle superstructures.

There are many examples reported in the literature that employ TOAB-capped AuNPs as building units for the formation of AuNP superstructures by simple addition of a cross-linking species that is capable of ligand exchange with the TOAB.[178–180,186] Such mediated assembly is more difficult to achieve in the case of electrostatically stabilized AuNPs, for example citrate-capped AuNP, since the repulsive electrostatic force impedes the AuNPs coming into close contact.[131] Therefore, electrostatically stabilized AuNPs are often found to not assemble into superstructures when treated with a cross-linking agent.[71,131] Superstructure formation and particle clustering can be achieved in these cases, if the AuNPs are covered with a sub-monolayer of the cross-linking organic species.[131,132] The additional electrostatic repulsion can lead to anisotropic superstructures deviating from globular shape.[172,187] Cross-linked particle superstructures featuring TOAB-capped AuNPs as building units, on the other hand, usually show globular morphology.[178–180,186] The concept of AuNP network formation mediated by multifunctional synthetic polymer was pioneered by Rotello and coworkers and the authors referred to this as ‘brick and mortar’ strategy.[171,188,189] Since it was not attempted within this early work to control the distribution of binding sites for the NPs within the cross-linking polymer,[190] the internal structure of the NP superstructures could not be modulated.[171] The distribution of binding sites for AuNPs within individual macromolecules can be controlled in RAFT polymers of specific multiblock architecture (see Section 1.6).[127] The influence of the binding site distribution within such multiblock RAFT polymers on the formation and internal structure of the resulting self-assembled hybrid superparticles will be the topic of this Chapter 3.

The formation of such spherical superstructures made of Brust–Schiffrin

particles and multiblock RAFT oligomers of styrene had already been described in earlier work.[191,192] In the present work described in this chapter, the internal structure of these nanoparticle superstructures had been explored and it had been probed which features on the level of polymeric architecture are influencing such a superparticle formation. Particularly, it appeared interesting to investigate the behavior of the several blocks in the multiblock RAFT polymer independently from each other and the overall multiblock structure, i.e. to study the performance of individual blocks in this superparticle formation. To this end, two sets of polymeric materials, one with TTC groups on both of its terminals (corresponding to individual blocks) and the other with multiple TTC groups incorporated along the polymeric backbone were prepared and investigated with regard to their ability of forming AuNP network structures from Brust–Schiffrin AuNPs. Following that, the self-assembly of TOAB-capped AuNPs mediated by these macromolecules is discussed and results from structural characterization of the superstructures are presented.

The following section will introduce into the design and synthesis of the specific polymeric architectures which act as particle cross-linkers.

3.2 Synthesis of Nanocomposite Materials

3.2.1 Design and Synthesis of the Macromolecular Linker

RAFT oligomerization of styrene mediated by telechelic ($\mathbf{L^2}$) and multifunctional ($\mathbf{L^m}$) linear RAFT agents (Scheme 3.1) were undertaken in order to obtain oligomers with TTC groups on both termini (so-called telechelic oligomers) and oligomers with TTC groups incorporated along their backbone, respectively. The synthesis of compound $\mathbf{L^2}$ is described in detail in the experimental part and the synthesis of compound $\mathbf{L^m}$ is described in a previous publication from the Vana lab.[124] Such RAFT agents of the TTC type with an acrylate type leaving group are suited for the fabrication of short chain oligomers of styrene with small dispersities.[193]

The resulting materials were analyzed by SEC (Table 3.1) and NMR (see Appendix A). In the case of telechelic oligomers, reasonably narrow molar mass distributions are observed in SEC analyses, proving a good control of the oligomerization process with RAFT agent $\mathbf{L^2}$. The relatively large dispersity values found for multiblock oligomers derived from $\mathbf{L^m}$, on the other hand, are known to reflect the distribution of the number of blocks among the macromolecules, while the block lengths are very narrowly distributed.[71,124] The average number of styrene units between the two terminal TTC groups in telechelic oligomers can be determined by both

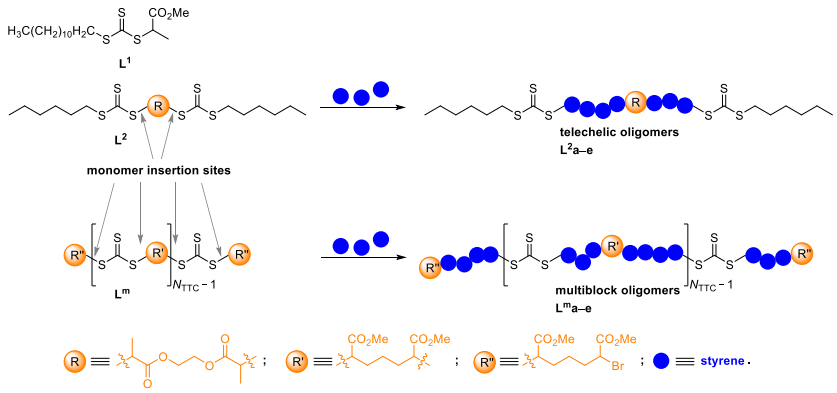

Scheme 3.1 A synthetic scheme showing the RAFT agents used comprising one ($\mathbf{L}^1$), two ($\mathbf{L}^2$) and multiple ($\mathbf{L}^m$, N_{TTC} refers to the average number of TTC groups per macromolecule in this case, as there is a distribution of this number among the produced macromolecules, see text) TTC groups and illustrating the molecular structures of the prepared telechelic RAFT oligomers derived from $\mathbf{L}^2$ and multiblock RAFT oligomers derived from $\mathbf{L}^m$.

SEC and NMR analysis. NMR is expected to give more accurate values at low degrees of polymerization due to the SEC calibration not being valid in this regime. The situation will change at larger degrees of polymerization because the NMR signal-to-noise ratio for the characteristic signal used in integration will decrease. Together, NMR and SEC give a good estimate for the average number of styrene repeating units and the results are summarized in Table 3.1. For multiblock oligomers, two quantities, namely

Table 3.1 Results from SEC and ^{1}H NMR characterization of telechelic and multifunctional RAFT oligomer samples.

Sample	M_n(SEC)	N_{st}(SEC)	N_{st}(NMR)	$Đ$(SEC)	N_{TTC}(NMR;SEC)
$\mathbf{L}^2\mathbf{a}$	750	2	5	1.25	2[a]
$\mathbf{L}^2\mathbf{b}$	1500	9	11	1.26	2[a]
$\mathbf{L}^2\mathbf{c}$	1800	12	14	1.29	2[a]
$\mathbf{L}^2\mathbf{d}$	2500	19	21	1.25	2[a]
$\mathbf{L}^2\mathbf{e}$	3500	28	24	1.32	2[a]
$\mathbf{L}^m\mathbf{a}$	4700	-	4	1.81	6
$\mathbf{L}^m\mathbf{b}$	8100	-	10	2.18	6
$\mathbf{L}^m\mathbf{c}$	8800	-	12	2.52	6
$\mathbf{L}^m\mathbf{d}$	11700	-	15	2.71	6
$\mathbf{L}^m\mathbf{e}$	13900	-	24	2.14	5

[a]not a calculated value.

the average number of styrene units (N_{st}) between two adjacent TTC groups and the average number of TTC groups (N_{TTC}), need to be determined. While the former value can be obtained directly from NMR measurements (see apendix for the corresponding spectra), the latter can be calculated from the average molar mass determined by SEC and the value for N_{st} from NMR.[191,192] The results from the analyses of multiblock oligomers can also be found in Table 3.1.

3.2.2 Preparation of Nanocomposite Materials

Gold nanoparticles were prepared by the two-phase Brust–Schiffrin synthesis and functionalized in an *ex-situ* approach. Prior to these functionalization reactions, the as-obtained nanoparticles were extensively washed with diluted sulfuric acid and water[184] to completely remove the reducing agent (sodium borohydride) used in the particle synthesis. This is necessary in order to assure the integrity of the TTC group in the substances used for surface modification. After this washing, the TOAB-capped AuNPs were treated with compound $\mathbf{L^1}$ (prepared according to literature)[192] and $\mathbf{L^2}$ (forming nanocomposites $\mathbf{L^1_{NC}}$ and $\mathbf{L^2_{NC}}$) as well as telechelic oligomers $\mathbf{L^2a–e}$ from Table 3.1 (forming nanocomposites $\mathbf{L^2a_{NC}–L^2e_{NC}}$) and multiblock oligomers $\mathbf{L^ma–L^me}$ from Table 3.1 (forming nanocomposites $\mathbf{L^ma_{NC}–L^me_{NC}}$) by addition of these materials to toluene dispersions of the AuNPs under stirring. AuNPs modified with monofunctional RAFT agent $\mathbf{L^1}$ were prepared for reference and also used to determine the particle diameter distribution *via* TEM (Figure 3.1).

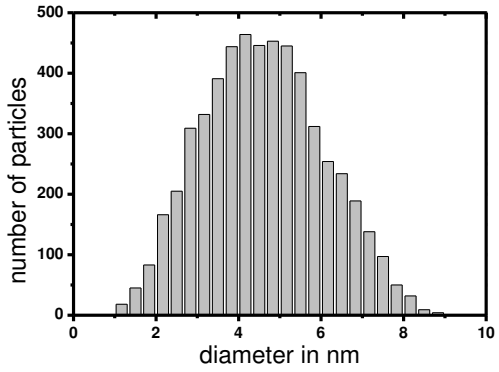

Figure 3.1 Diameter histogram of gold nanoparticles made by the two-phase Brust–Schiffrin synthesis which were used in this chapter. A total number of 5522 particles from 22 individual images was analyzed. The average diameter was found to be 4.6 nm with a standard deviation of 1.5 nm. The aspect ratio of the particles was determined from these images as 1.12 ± 0.09.

3.3 Analysis of Nanocomposite Materials

Dynamic Light Scattering (DLS). With the DLS method, it is possible to scan analyte samples over a large size range. DLS measurements had been conducted in order to obtain size information for the colloidal systems under investigation in dispersion. Dilute analyte samples were prepared in order to avoid multiple scattering and sample $\mathbf{L^1_{NC}}$ was included for reference. A single-stage sigmoidal decay of the correlation function over two orders of magnitude in the correlation decay times was observed for sample $\mathbf{L^1_{NC}}$ (Figure 2, top row). For samples treated with telechelic (samples $\mathbf{L^2_{NC}}$ and $\mathbf{L^2a_{NC}}$–$\mathbf{L^2e_{NC}}$) and multiblock (samples $\mathbf{L^ma_{NC}}$–$\mathbf{L^me_{NC}}$) RAFT oligomers (i) larger intercepts of the correlation functions and (ii) larger characteristic decay times are observed. The intercept can be understood as a measure for the signal-to-noise ratio and the improved signal intensity for samples $\mathbf{L^2_{NC}}$–$\mathbf{L^me_{NC}}$ (with respect to sample $\mathbf{L^1_{NC}}$) is therefore consistent with AuNP network formation, as the scattered intensity is expected to increase in case of particle agglomeration. A shift of the characteristic decay time of approx. one order of magnitude (with respect to sample $\mathbf{1_{NC}}$) and yet a single-stage sigmoidal decay is observed for samples $\mathbf{L^2_{NC}}$, $\mathbf{L^2a_{NC}}$, and $\mathbf{L^ma_{NC}}$. This indicates the presence of species with a much smaller diffusivity and this observation can be attributed to the presence of AuNP networks in dispersion. The remaining samples show characteristic decay times of the order of sample $\mathbf{L^1_{NC}}$, together with a tailing toward the characteristic decay times of samples $\mathbf{L^2_{NC}}$, $\mathbf{L^2a_{NC}}$, and $\mathbf{L^ma_{NC}}$. This behavior can be assigned to the presence of monomeric particles together with a small number of cross-linked particle network structures.

Fitted intensity distributions are displayed in Figure 3.2 (bottom row). It can be seen that the larger particles which had been attributed to AuNP networks are orders of magnitude larger than the primary particles (sample $\mathbf{L^1_{NC}}$, intensity distribution centered around 12 nm), as had already been observed in earlier work[191,192] by TEM. Interestingly, the fraction of AuNP networks to primary particles drops sharply once a distinct number of styrene spacers (approx. 5 monomeric repeating units) between two adjacent TTC groups is exceeded (a monomodal intensity distribution centered around large particle diameters is only found for samples $\mathbf{L^2_{NC}}$, $\mathbf{L^2a_{NC}}$, and $\mathbf{L^ma_{NC}}$ with $N_{st} \leq 5$, see Table 3.1). This critical number of styrene units is the same for multiblock RAFT oligomers and telechelic oligomers (resembling single blocks). This result shows that network formation in this system is mostly affected by the length of the spacer between two anchoring sites for gold: Network formation is only observed for small lengths of this spacer, independent of the overall number of these binding sites in one

macromolecule and the average molar mass of one macromolecule. After passing this threshold number, the relatively small fraction of AuNP networks shows the general trend to further decrease with increasing N_{st}. It is very likely that this observation reflects a tendency of the employed macromolecules (which are either telechelic or multifunctional) to attach to AuNP surfaces in a bidentate or multidentate fashion, respectively, leading to loops on the surfaces of individual particles impeding their cross-linking, as this mode of attachment to the surface was already observed by employing multiblock RAFT polymers of N^{i}PAAM (average molar mass > 40 kDa, and average number of TTC groups between 1.9 and 4.5, as determined by SEC analysis of the cleavage products) on AuNPs from citrate-reduction.[71] This is logical, as loop formation can only occur, if the number of monomeric repeating units between two anchoring sites for gold is larger than the Kuhn length of the respective polymer. Sample $\mathbf{L^m b_{NC}}$, however, which shows a monomodal intensity distribution centered around 14 nm falls off this trend, suggesting that only very small particle networks are present in this case. In addition, the fact that the dispersant can flow through the AuNP networks may possibly affect the determined diffusivity of the colloidal superparticles.[194] The fact that the extent of network

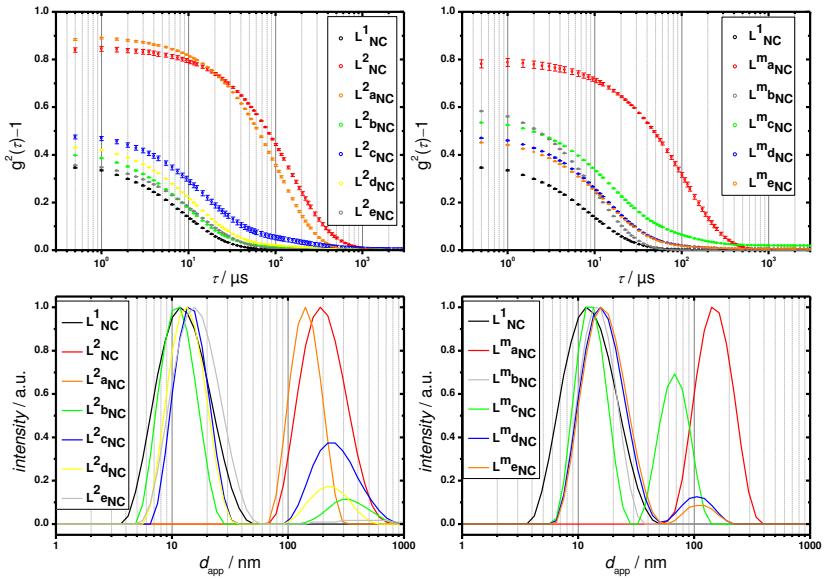

Figure 3.2 Dynamic light scattering data for AuNPs treated with telechelic RAFT oligomers of styrene (left side) and multiblock RAFT oligomers of styrene (right side); particles treated with monofunctional RAFT agent $\mathbf{L^1}$ (sample $\mathbf{L^1_{NC}}$) are shown for comparison in both diagrams. The top row shows the correlation functions of these nanocomposites, while the respective fitted intensity distribution functions are displayed in the bottom row.

formation decreases with increasing number of styrene repeating units in the organic part of the nanostructures makes clear that network formation is driven by the TTC groups and not by π-π-interactions between the phenyl moieties present in the monomeric repeating units, which can, however, principally lead to AuNP cross-linking.[173]

Small-Angle X-ray Scattering (SAXS). Complementing the DLS measurements presented above, SAXS characterization was undertaken in order to get insights into the internal structure of the AuNP networks. Because of the high electron density of gold, AuNPs provide much higher contrast to the dispersant compared with the organic molecules present in the investigated samples, which renders X-ray scattering techniques ideally suited to study such systems. Also, it is known for such systems that no radiation damage occurs due to exposure to the X-ray beam.[171,195]

Scattering profiles for samples with sufficient dilution (approx. 2 mg gold per mL) had been measured to exclude contributions from particle-particle interactions from individual particles. In case of particle clustering due to an attractive potential (in the case of this study, this is cross-linking by organic molecules) an increase of the scattered intensity toward smaller *q*-values can be expected.[196–198]

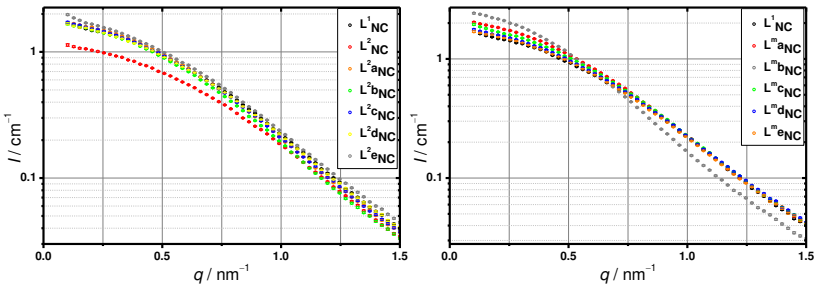

Figure 3.3 Small-angle X-ray scattering curves for Brust–Schiffrin particles treated with difunctional RAFT agent $\mathbf{L^2}$ (sample $\mathbf{L^2_{NC}}$) and telechelic RAFT oligomers $\mathbf{L^2a–L^2e}$ (samples $\mathbf{L^2a_{NC}–L^2e_{NC}}$) are shown in the diagram on the left side. Scattering curves for particles treated with multifunctional RAFT polymers $\mathbf{L^ma–L^me}$ (samples $\mathbf{L^ma_{NC}–L^me_{NC}}$) are displayed in the diagram on the right. The scattering curve of AuNPs modified with monofunctional RAFT agent $\mathbf{L^1}$ (sample $\mathbf{L^1_{NC}}$) is included for reference in both diagrams.

The data in Figure 3.3 show that the scattering curve of sample $\mathbf{L^2_{NC}}$ differs the most from the scattering profile of the reference $\mathbf{L^1_{NC}}$. Interestingly, decreased scattered intensity toward smaller *q*-values in the range investigated is found for sample $\mathbf{L^2_{NC}}$, for which particle networks were postulated from DLS. A Guinier fit (Figure 3.4) to the data suggests that the

scatterers in sample $\mathbf{L^2_{NC}}$ would even have a slightly smaller radius of gyration (R_g) of approx. 2.4 nm compared with the R_g value of approx. 2.6 nm obtained for a Guinier fit to the scattering data for sample $\mathbf{L^1_{NC}}$. To understand this unexpected behavior, the invariant Q was analyzed, which had been introduced by Porod:[199]

$$Q = \int_{q=0}^{\infty} I(q) \cdot q^2 \mathrm{d}q. \qquad (3.1)$$

To this end, the scattering curves were extrapolated toward zero scattering angle by the Guinier approximation (Figure 3.4) and toward large q-values by the Porod approximation. The Porod approximation also permits analytical integration of (3.1) in the respective q range (see Appendix B). Both extrapolations together enabled the determination of values for the quantity Q as given in equation 3.1. As can already be anticipated from the two scattering curves, these values differ significantly for samples $\mathbf{L^1_{NC}}$ ($Q_{\mathbf{L1NC}}$ = 0.37 cm^{-1}nm^{-3}) and $\mathbf{L^2_{NC}}$ ($Q_{\mathbf{L2NC}}$ = 0.30 cm^{-1}nm^{-3}), see also Figure 3.5. Although the scattering profile for an aggregating sample may be altered due to particle clustering, the value of Q is required to remain invariant.[199] The significantly reduced value for $Q_{\mathbf{L2NC}}$ with respect to the Q-value for nonaggregating system $\mathbf{L^1_{NC}}$ can therefore be understood as an indirect hint for amplified scattering at very small scattering angles not accessible by the experimental setup. Hence, the difference in the Q-values accounts for big, nonresolved AuNP aggregates.

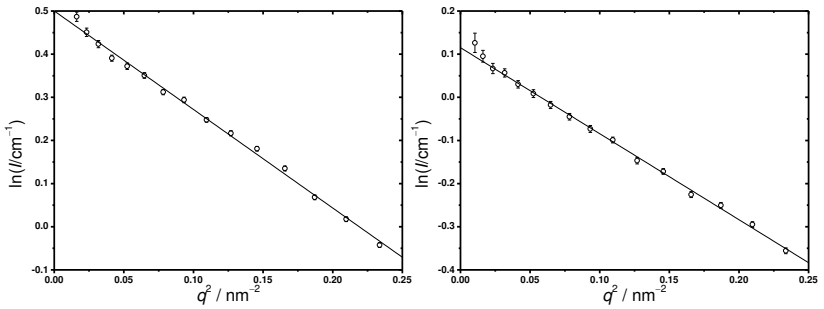

Figure 3.4 Gunier fit of the scattering data for samples $\mathbf{L^1_{NC}}$ and $\mathbf{L^2_{NC}}$ in a q-range $q < 0.5$. From the slope of the linear fit, radii of gyration of 2.6 nm and 2.4 nm, respectively, had been obtained. From the y-intercepts, intensities at zero scattering angle, $I(q=0)$ of 1.6 cm^{-1} and 1.1 cm^{-1}, respectively, can be obtained.

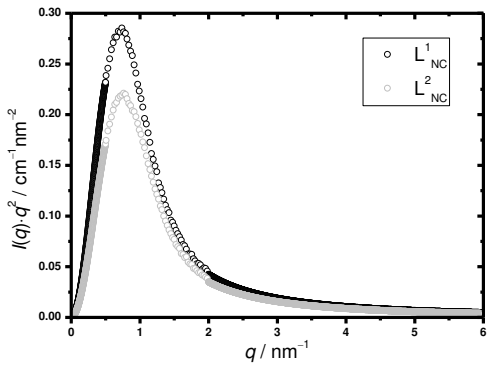

Figure 3.5 A plot of $I(q)\cdot q^2$ vs. q for samples $\mathbf{L^1_{NC}}$ (black curve) and $\mathbf{L^2_{NC}}$ (gray curve). Both curves consist of a part $q < 0.5$ nm^{-1}, which was derived from the Guinier approximation for extrapolation toward zero scattering angle, a part 0.5 nm^{-1} < q < 2.0 nm^{-1} showing the actual measured data, and a part $q > 2.0$ nm^{-1} derived from the Porod approximation for extrapolation toward large q. While integration over the Porod region can be done analytically, integration over the q-interval 0.0 – 2.0 nm^{-1} had been performed numerically.

Increasing scattering intensity with respect to $\mathbf{L^1_{NC}}$ toward smaller q-values can be observed for all remaining samples to only a small extent, an exceptional case being sample $\mathbf{L^m b_{NC}}$. Dynamic light scattering already indicated the presence of smaller particle network structures for sample $\mathbf{L^m b_{NC}}$ compared with the other samples. The increasing scattering intensity toward small q-values for sample $\mathbf{L^m b_{NC}}$ therefore likely reflects the presence of these small particle networks. The larger networks which were found by DLS for the other samples to be of the order of hundred nanometers in diameter, are beyond instrumental resolution D_{max} of the SAXS setup used, which is, according to the sampling theorem of Fourier Transformation, $D_{max} \leq \pi/q_{min} \approx 30$ nm.

As has been pointed out in a review[200] by Wang *et al.,* obtaining quantitative measures for interparticle separations in network structures is crucial for proving the claim of particle interconnection by the employed cross-linking agent. In the case of AuNPs from the two-phase Brust–Schiffrin synthesis, this is proving that interparticle distances are determined by the cross-linker rather than remaining phase-transfer catalyst (TOAB) on the particle surfaces.[200] For this purpose, structure factors had been determined for samples in which BS particles were treated with cross-linking agent by dividing the respective scattering curve by the single particle curve (sample $\mathbf{L^1_{NC}}$):[195]

$$I_{\text{L2NC-L2eNC,LmaNC-LmeNC}} \sim I_{\text{L1NC}} \cdot S(q). \quad (3.2)$$

A broad structure factor peak is observed for sample $\mathbf{L^2_{NC}}$ (Figure 3.6 A), which can be attributed to the accumulation of distinct interparticle separations in the dispersion. This structure factor does however not approach a value of 1.0, as would be expected for such network forming systems.[195] This can be explained by the fact that the scattering for sample $\mathbf{L^2_{NC}}$ is decreased in the experimentally accessible q-range and largely enhanced in the very small q-range as indicated by an analysis of the invariant presented above. To account for this, the obtained structure factor can be scaled by the ratio of the Porod constants obtained for samples $\mathbf{L^1_{NC}}$ and $\mathbf{L^2_{NC}}$, to achieve a structure factor which indeed approaches a value close to 1.0 (Figure 3.6 B). The peak position is of course not altered by this manipulation. Therefore, associated interparticle distances, $d_{\text{center-center}}$, can be estimated from the Bragg relation as such:

$$d_{\text{center-center}} = \frac{2\pi}{q^*}. \quad (3.3)$$

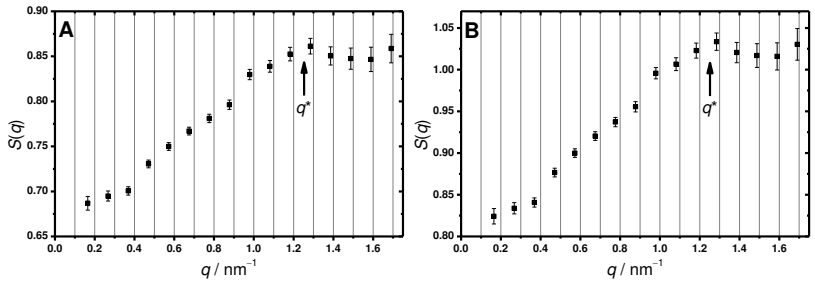

Figure 3.6 Structure factor for sample $\mathbf{L^2_{NC}}$ as determined *via* small-angle X-ray scattering by dividing the scattering curve of sample $\mathbf{L^2_{NC}}$ by the scattering curve of noninteracting particles from sample $\mathbf{L^1_{NC}}$ (A). The plot on the right displays the same structure factor scaled by the ratio of the determined Porod constants for samples $\mathbf{L^1_{NC}}$ and $\mathbf{L^2_{NC}}$ (B).

A value of 5.2 nm can thus be extracted from the structure factor in Figure 3.6. The particles were shown to a have an average diameter of 4.6 ± 1.5 nm by real-space characterization *via* TEM (see Figure 3.1). The diameter histogram obtained by TEM characterization is supported by the pair-distance distribution function (PDDF) obtained from indirect Fourier Transformation[201] of the scattering curve of sample $\mathbf{L^1_{NC}}$. This PDDF displays a maximum dimension of the scattering objects of approx. 9.5 nm (see Appendix, Figure C1), which is in good agreement with a largest

particle diameter of approx. 8.5 nm together with a particle aspect ratio of 1.12 (Figure 3.1). The value for $d_{\text{center-center}}$ determined from the structure factor analysis therefore corresponds to a particle edge-to-edge separation, $d_{\text{edge-edge}}$, of approx. 0.6 nm. For comparison, distances between thiocarbonyl sulfur and gold(I) atoms have been determined by X-ray diffraction to be approx. 2.3 Å,[153] (see also Section 2.1) while an edge-to-edge separation of approx. 2.0 nm would be expected, if interparticle distances would be determined by TOAB.[200] The SAXS data are therefore in line with particle cross-linking through the difunctional RAFT agent $\mathbf{L^2}$ in sample $\mathbf{L^2_{NC}}$ rather than only partial ligand exchange of the TOAB with the RAFT species, and particle distances being determined by two TOAB ligands.

While the structure factor peak is already very broad for sample $\mathbf{L^2_{NC}}$, probably due to the dispersity of the nanoparticles themselves, structure factor peaks for the other samples characterized in this work had not been observed. However, such structure factor peaks are common features for AuNPs connected by DNA linkers.[194,195,202] The disappearance of the structure factor peak for samples $\mathbf{L^2a_{NC}}$–$\mathbf{L^me_{NC}}$, with inserted styrene monomer, therefore likely reflects the dispersity of the particle linker as well as its conformational degrees of freedom, since polystyrene is much less rigid compared with DNA.

Transmission Electron Microscopy (TEM). The AuNP network structures were visualized by means of TEM to ascertain their shape after drop-casting from colloidal dispersion and applying high vacuum during the actual measurement. Network structures were observed in all cases of samples $\mathbf{L^2_{NC}}$–$\mathbf{L^me_{NC}}$, with the only exception of sample $\mathbf{L^2e_{NC}}$. A typical TE micrograph for sample $\mathbf{L^2e_{NC}}$ is included in the Appendix (Figure C2). Network structures with telechelic RAFT oligomers are shown in Figure 3.7 and structures with multiblock RAFT oligomers are shown in Figure 3.8. In all cases gray-scale analysis[104] along a horizontal axis was performed, which revealed the brightness of the image to generally decrease toward the center of the nanostructures. This can be attributed to more particles contributing to the contrast of the image toward the center of the nanoobjects, supporting that these objects are three-dimensional and evenly filled with primary AuNPs. A (partly) preserved three-dimensional shape of these nanoparticle superstructures after deposition on a solid substrate had already been found by AFM characterization and recognized as an indication for particle cross-linking.[192] The fluctuations in the gray-scale values represent the fact that the superparticle structure is heterogeneous, as it is composed of primary AuNPs. The TE micrographs corresponding to nanocomposites with multifunctional RAFT oligomers shown in Figure 3.8 reflect the earlier

observed[192] trend of decreasing particle density with increasing degree of oligomerization of the cross-linking agent, while a similar trend is not as clear for the nanocomposites with telechelic RAFT oligomers shown in Figure 3.7.

A question associated with the interpretation of TE micrographs in general which has to be taken into critical account is if the micrographs reflect structures as they exist in colloidal dispersion, or if TEM structures are merely drying artifacts[203,204] that result from the sample preparation. To address this question, the following experiment was peformed: Colloidal dispersions of hybrid systems comprising multiblock oligomers of styrene and Brust–Schiffrin particles were treated with a nonsolvent for polystyrene (*iso*-propanol in this case) to induce the aggregation of the primary species present in the original colloidal dispersion into larger aggregates. TE microscopic analysis was then undertaken in order to visualize the aggregated structures (Figure 3.9). As can be seen from Figure 3.9, agglomerates that are composed of spherical AuNP assemblies are observed in this case. This result strongly suggests that the spherical AuNP assemblies are the primary, colloidally stable species present in dispersion, and that modification of their solvent environment can trigger their agglomeration.

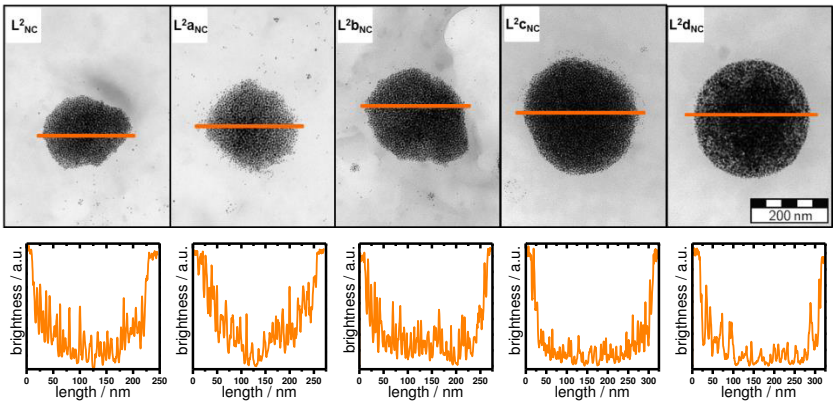

Figure 3.7 Transmission electron micrographs for samples $\mathbf{L^2_{NC}}$–$\mathbf{L^2d_{NC}}$ (top row). Results from gray-scale analysis along the axis indicated by the orange line are shown in the bottom row.

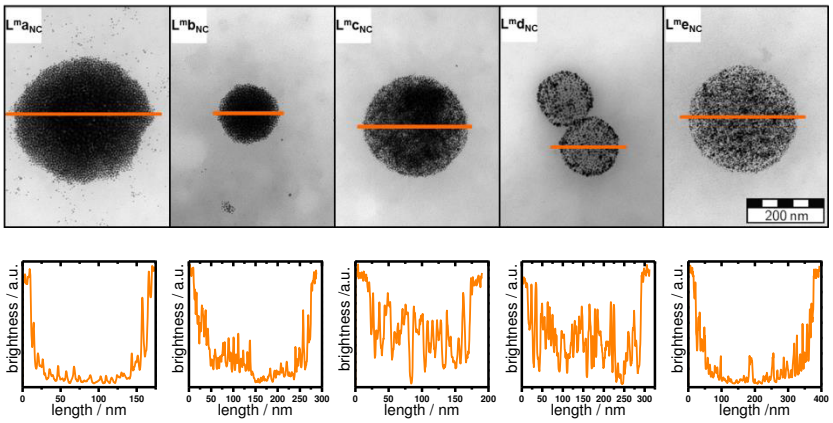

Figure 3.8 Transmission electron micrographs for samples $\mathbf{L^m a_{NC}}$–$\mathbf{L^m e_{NC}}$ (top row). Results from gray-scale analysis along the axis indicated by the orange line are shown in the bottom row.

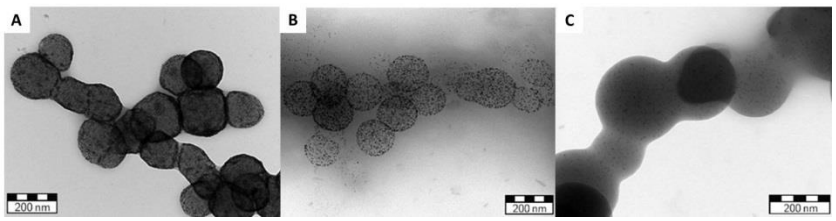

Figure 3.9 TEM images of chain-like agglomerates of spherical gold nanoparticle assemblies with multiblock oligomers of styrene. The number of styrene units per block increases from A to C.

UV/Visible Extinction Spectroscopy. In order to support the claims derived from the prior analyses, UV/visible spectra (Figure 3.10) of the nanocomposites under investigation had been analyzed. UV/visible spectra of AuNPs and their assemblies feature a plasmon band in the optical region which arises from charges oscillating with the so-called plasmonic frequency.[31] Toward smaller wavelengths in the UV region, increased extinction can be observed due to interband transitions between the 5d and 6s level.[165,166] It is known that a red-shift of the plasmon-band maximum will occur in the case of AuNPs coming into close proximity due to plasmon band coupling, with the critical distance for this phenomenon being determined by the ratio of interparticle distance $d_{\text{center-center}}$ to the particle diameter $2R$ (significant red-shift if $d_{\text{center-center}}/2R < 1.5$).[205] The magnitude of the plasmon-band red-shift is known to scale with interparticle distances.[206] On the other hand, relating the one-dimensional parameter of the plasmon-band red shift to interparticle distances exclusively can only be done for well-defined systems[206] but is generally problematic in case of AuNP networks, as its value depends on more parameters, the extent of network formation being the most obvious example, as recognized by Lim *et al.*[180] The smaller the extent of particle cross-linking becomes, the more primary, noncrosslinked particles will contribute to the plasmon band and, consequently, the plasmon-band shift will be weak. It is also important to compare samples of interest to a suited reference, because modification of the AuNP surface with ligands can lead to charge transfer complexes which also influence the plasmonic frequency.[148,167] Therefore, again, sample $\mathbf{L^1_{NC}}$ is a well-suited reference for comparison.

As can be seen in Figure 3.10, a pronounced shifting (with respect to sample $\mathbf{L^1_{NC}}$) of the plasmon band toward longer wavelength is only observed for samples $\mathbf{L^2_{NC}}$, $\mathbf{L^2a_{NC}}$, and $\mathbf{L^ma_{NC}}$, while the plasmon band peak position is only marginally shifted for the remaining samples. This is in perfect agreement with the DLS measurements, which revealed only a relatively small fraction of AuNP networks for samples $\mathbf{L^2b_{NC}}$–$\mathbf{L^2e_{NC}}$ and $\mathbf{L^mb_{NC}}$–$\mathbf{L^me_{NC}}$. Also, the spectra feature another peak centered at around 308 nm, which can be attributed to the π-π*-transition of not surface-bound TTC groups, as this transition of the thiocarbonylthio group is known to be bleached upon chemisorption to the AuNP surface.[148] Thus, it can be concluded from these measurements that the ligands were indeed added in excess to the particles. Together with the high binding constant of RAFT species at AuNPs (see Section 2.2), this leads to the conclusion that network formation is not triggered by insufficient shielding of the AuNP surface.

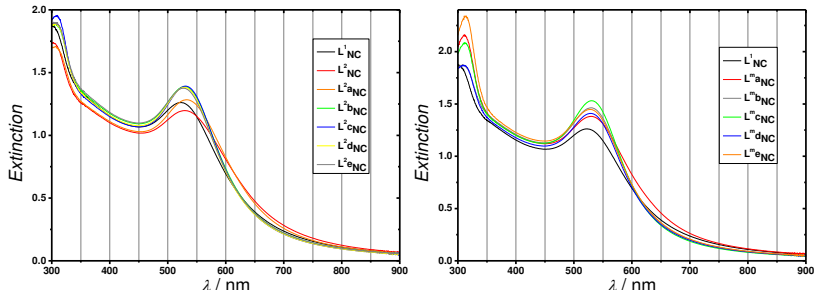

Figure 3.10 UV/visible extinction spectra for AuNPs treated with telechelic (left side) and multiblock RAFT oligomers (right side). The spectrum of sample $\mathbf{L^1_{NC}}$ is included in both graphics for reference (black line).

3.4 Conclusions

The self-assembly in hybrid systems of linear RAFT oligomers of styrene bearing two and multiple TTC groups and AuNPs into NP superstructures had been investigated in detail within this chapter. Analysis of a structure factor from SAXS measurements indicated that AuNPs are indeed interconnected by the employed particle cross-linker in these systems. Large particle network structures on the order of hundreds of nanometers were found by TEM. Gray scale analysis of the TE micrographs of the superstructures supports their three-dimensional shape and suggests that these structures are evenly filled with primary AuNPs. Inspection of the TE micrographs furthermore suggests that the density of these primary AuNPs within the network structures can be controlled by adjusting the degree of oligomerization of styrene in the multiblock oligomers using the RAFT technique. Evidence for the claim that globular particle network structures are indeed also present in the colloidally dispersed state had been obtained via (i) TEM showing that these globular network structures further agglomerate upon addition of a nonsolvent and (ii) via scattering techniques applied directly to such colloidal dispersions: While the large network structures were beyond instrumental resolution of the experimental SAXS setup, DLS measurements revealed—backed up by results from UV/visible spectroscopy—that a huge extent of network formation appears only in the case of a small number of styrene repeating units interconnecting two neighboring TTC groups, independent from the overall number of TTC groups. Consistent with that interpretation, indirect evidence for network formation was found by analysis of SAXS data only for sample $\mathbf{L^2_{NC}}$ with the very shortest particle linker without inserted monomer. The observed attenuation of network formation by increasing the oligostyrene linker

between two anchoring sites for gold is probably due to the formation of loops on the particle surfaces which confine all binding sites to one particle and therefore impede cross-linking with other nanoparticles.

The self-assembly of a particular type of AuNPs (i.e. TOAB-capped AuNP from the two-phase Brust–Schiffrin synthesis) was demonstrated in this chapter. A logical next step would be to test the possibility of employing RAFT polymers for forming hierarchical higher-order assemblies that feature more than one type of NPs. The application of self-assembly strategies can in such cases only be successful, if at least one component in the self-assembly process permits directional interactions, and the implementation of such directional interactions can be very sophisticated and demanding.[207,208] The following Chapter 4 will, therefore, concentrate on the development of a synthetic strategy which is based on purification of intermediates in a multi-step synthetic route rather than self-assembly for the fabrication of planet–satellite nanostructures. The implications of the presented approach will be investigated and the nanomaterials produced will be analyzed and discussed in detail.

Chapter 4

Tailored Assembly of Two Types of Gold Nanoparticles into Planet–Satellite Structures[4]

4.1 Preface

The investigation and application of multicomponent nanoarchitectures[209] requires the hierarchical arrangement of distinct domains on small scale. Such multicomponent nanoarchitectures can take a generic form in which one AuNP acts as a central unit with specific surface functionalization as scaffold architecture. For example, smaller AuNPs can be adsorbed directly on the surface of a larger central AuNP with specific surface chemistry[210] or they can be covalently attached to the central AuNP using "click" chemistry.[211] These approaches are very straightforward to implement, however, they do not allow the tuning of the spatial relations of the two types of particles, which strongly influence the physical properties of the resulting nanoobject.[31] These interparticle distances can be modulated within a few nanometers by varying the length of linking alkyl chains.[212–214] For controlling interparticle separations within larger length scales, it appears logical to employ well-defined polymers as particle linkers. In the past decade, the most significant advances in this field mostly relied on supramolecular recognition via complementary ssDNA, either alone[195,202,208,215–224] or in conjunction with rigid particle-linking bundles

[4]Adapted with permission from Rossner, C.; Vana, P. *Angew. Chem. Int. Ed.* **2014**, *53*, 12639–12642, Copyright 2014, Wiley-VCH Verlag GmbH & Co. KGaA, Weinheim; from Rossner, C.; Roddatis, V.; Lopatin, S.; Vana, P. *Macromol. Rapid Commun.* **2016**, *37*, 1742–1747; and adapted from Rossner, C.; Tang, Q.; Glatter, O.; Müller, M.; Vana. P. *submitted to ACS Nano*.

assembled via DNA origami.[207] Although these results are intriguing, they are limited by their complicated synthesis procedures, and are hardly expected to be suited for providing larger quantities of material (as has already been pointed out in the Foreword). Therefore, much research is devoted to using tailored synthetic polymers as key components in the development of efficient and flexible routes to structurally ordered nanoarchitectures (see also Chapter 1).[38,128,225] Within this chapter, the development of a modular synthetic strategy for the formation of planet–satellite nanostructures from RAFT star polymers and gold nanoparticles will be presented.

4.2 A Design Strategy for Synthesizing Planet–Satellite Nanostructures

For synthesizing planet–satellite structures, a modular approach in which the overall structure is built around a scaffold from inside to outside[226] appears to be a promising strategy. Such overall strategy can be realized in the form of a convergent synthetic procedure, in which the modular building units are prepared in parallel as individual components and subsequently combined in a controlled fashion (see Scheme 4.1). It had been shown that AuNPs can be modified with a polymer layer which in turn allows further particles to be attached to the resulting core–shell structure. That way, the core–shell particles act as multifunctional nanoparticle scaffold architectures,[43] for the attachment of additional AuNPs. This becomes possible, when multiple binding sites for gold are present in the polymer that is immobilized to the central AuNP, forming the scaffold. In the general sense, such strategy had been successfully implemented by using hyperbranched RAFT polymers (see also Section 1.7).[131–133] Compared with these hyperbranched polymers, macromolecules with star topology,[227] are much better defined at the molecular level, as their branches are all joined at a common core. By employing controlled techniques such as RAFT they can also feature a small dispersion with respect to branch lengths. When the different arms of the star are joined together via their reinitiating R groups, macromolecules with the sulfur-containing RAFT groups exposed on the outer sphere of the star—and therefore accessible for functional units to be attached—will result.

In the following, a novel synthetic strategy for the preparation of planet–satellite nanostructures will be evaluated in detail. The original approach is centered around well-defined RAFT star polymers, which, by virtue of their macromolecular characteristics, are intended to provide a

handle for the fine control of particle distances within individual planet–satellite arrangements (Scheme 4.1). Disclosing the role of this star polymer species will be the focus of Section 4.3.1. To protect the attempted structure from aggregation by providing colloidal stability, linear polymer species with one end group are suited candidates for this stabilization purposes. This linear polymer species is indeed essential for obtaining planet–satellite nanostructures: In earlier attempts, where no shielding linear polymer was employed, planet–satellite nanostructures with insufficient colloidal stability were obtained, showing the crucial role of the shielding linear chains. The nanoscopic localization of this linear macromolecular species within planet–satellite structures was revealed by means of TEM EELS and will be discussed in Section 4.3.3. Section 4.3.2 will be dedicated to the analysis of the star polymer canopy after casting the core–shell particles on surfaces. Finally, Section 4.3.4 will deal with the structural characterization of planet–satellite nanostructures in colloidal dispersion.

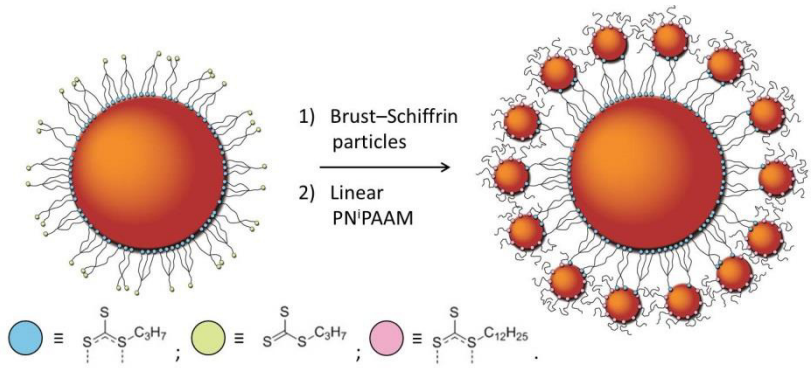

Scheme 4.1 Synthetic scheme for the preparation of planet–satellite nanostructures from AuNP-core–star-polymer-shell nanohybrids.

4.2.1 Two Distinct Types of Gold Nanoparticles as Modular Building Units

The most commonly employed method for synthesizing low-disperse AuNPs features the reduction of a gold(III) precursor in boiling aqueous solution by sodium citrate and is often referred to as "Turkevich" or "Frens" method.[228,229] The resulting aqueous colloidal dispersions are stabilized electrostatically by adsorbed excess citrate anions.[230] The size of the resulting particles can be controlled, for example by adjusting the gold(III)/citrate ratio.[229] A typical protocol[71,231] that was also used in this

thesis results in gold core diameters around 13-14 nm with small dispersity. When these particles from citrate-reduction are compared with AuNPs from the two-phase ex-situ Brust–Schiffrin synthesis (see Section 3.2.2), it is recognized that the diameter histograms for both types of particles do not overlap (Figure 4.1). Thus, although both types of particles are composed of gold, individual nanoparticles can be easily assigned to one of the two populations, as both can be strictly discriminated by their size.[231] By virtue of this property, these two types of particles are excellent candidates for their use as building units for planet–satellite nanostructures (as "planet" and "satellite" particles, respectively). A challenge that still needs to be overcome for bringing both types of particles together is posed by the fact that Brust–Schiffrin particles are obtained in toluene dispersion and the citrate-reduced AuNPs in aqueous dispersion. The approach followed here to tackle this challenge is to functionalize citrate-reduced AuNPs with a shell of water-soluble PN^{i}PAAM, which is, as free polymer, also soluble in typical organic solvents. With these gold-core–PN^{i}PAAM-shell particles, solvent exchange could then be attempted, making the core–shell scaffold structure ready for the addition of lipophilic Brust–Schiffrin particles. The choice of PN^{i}PAAM as the star polymer species is also interesting with regard to its stimuli-responsiveness, i.e., its temperature- and pressure-dependent coil-to-globule transition.[232] The preparation of these PN^{i}PAAM star polymers is discussed in the following section.

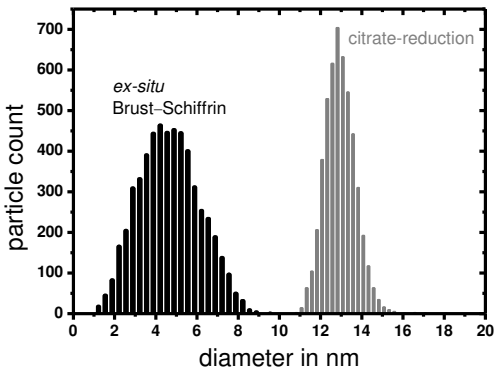

Figure 4.1 Diameter histograms for the two types of AuNPs which are used for the construction of planet–satellite nanostructures.

4.2.2 RAFT Star Polymers for the Fabrication of Planet–Satellite Nanostructures

RDRP techniques have enabled the formation of star polymers by the 'core-first' approach which circumvents significant issues associated with the coupling of preformed polymer arms ('arm-first' approach). The RAFT technique is unique in this respect, as it may result in either Z-star[227] or R-star RAFT polymers, which differ both in the formation mechanism and the structure of the obtained products: In the Z-star approach, RAFT groups are covalently linked to a common core via their stabilizing Z groups, so that linear macroradicals undergo propagation steps in solution. Continuous rapid interchange with the (dormant) arms of star polymer species enables the formation of star polymers with narrow molar mass distribution. The fact that the mediating RAFT groups remain close to the core of the star does not necessarily imply that they are not efficient in mediating the polymerization;[233] more important for achieving defined star polymer topologies is the appropriate choice of the leaving R group for the monomer to be polymerized.[234] While sulfur containing RAFT moieties will remain at the core in Z star polymers, these functional units will be expressed at the exterior of the star-shaped macromolecules following the R group approach, and thus may enable surface functionalization. In fact, star polymers with 'sticky' end groups are surface active species, because they show less entropic penalty caused by immobilization on the surface compared with linear polymers due to the presence of multiple arms.[235] RAFT star polymers with six, four, three, and (if considered a star polymer) two arms following the core-first R group approach were prepared for this study. This strategy implies that, in addition to the formation of well-defined star polymers, there will inevitably be contaminations from star-star couples formed via recombination of macrostar radicals, and also from linear initiator-derived chains which may be both irreversibly terminated and dormant.[236] The fraction of these side-products can be reduced to a small number, when only a low amount of radical initiator is decomposed under the polymerization conditions applied. The polymerization conditions for the preparation of star polymer samples used in this thesis can be found in the experimental part (Section 6.3.4).

In SEC characterization of macromolecules with star topology, the fact that their hydrodynamic radii are systematically smaller as compared with polymers of linear topology with the same molar mass needs to be considered. This effect is due to the confinement of the star polymer branches to a central core and the ratio of the hydrodynamic radii for star

polymer and linear polymer species is dependent on the number of branches joined at the core.[59] In earlier work, the Vana group found an elegant way to determine correction factors in order to compensate for this topological effect[237,238] and average molar mass values for star polymers were thus corrected by multiplication with these experimental factors (these factors are 1.15, 1.3, and 1.5 for 3-arm, 4-arm, and 6-arm star polymers, respectively). By taking these correction factors into account, the determination of star polymer molar masses becomes possible from measurements on a SEC setup that is calibrated by using linear polymer standards. The (uncorrected) SE chromatograms (Figure 4.2) display only small shoulders at higher molar masses and only reasonably low tailing toward lower molar masses, suggesting that contaminating side products mentioned above are present to only a small extent in the star polymer materials produced. Hence, the SE chromatograms prove the successful formation of well-defined macromolecular species with distinct molar masses.

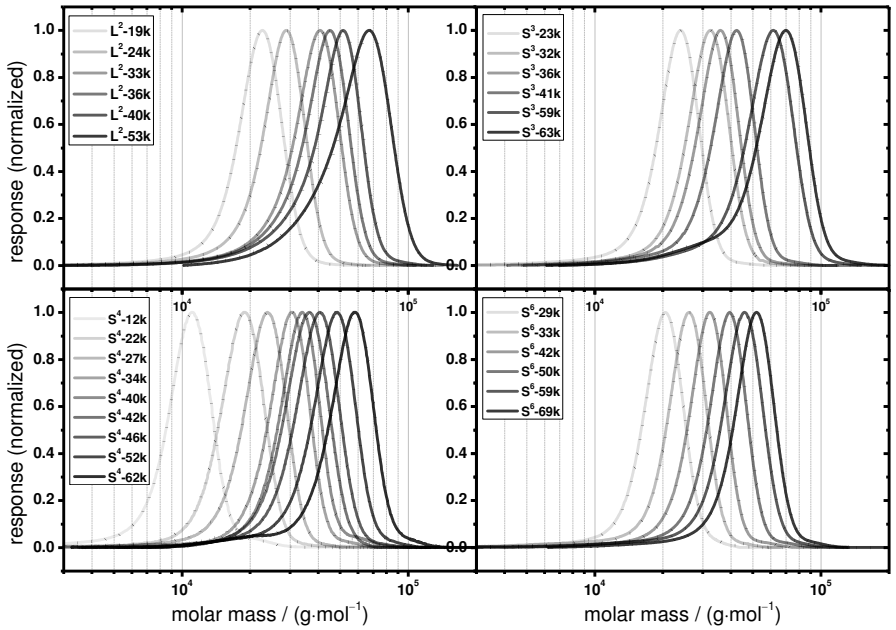

Figure 4.2 (Uncorrected) SE chromatograms for the star polymers and linear telechelic polymers of N^{i}PAAM used in this thesis. The traces were monitored by refractive index (solid lines) as well as UV (310 nm) detection (dotted lines). The absorbance at 310 nm is specific to the TTC groups and the excellent fit of the UV traces to the RI traces therefore proves that the TTC end groups are maintained in the star polymer materials produced.

The produced macromolecules were subsequently used to cover gold nanocrystals from citrate-reduction (see Section 4.2.1) in a 'grafting-to' approach, forming core-shell nanohybrids. The core–shell particles can be subject to centrifugation-redispersion cycles, enabling the purification of the nanohybrids by removal of unbound polymer and remaining low molecular weight compounds from the nanoparticle synthesis and also permits solvent exchange to methanol and finally dichloromethane, owing to the solubility of PN^{i}PAAM and its nanohybrids in a wide variety of solvents. Thus, the solvent transfer of citrate-reduced AuNPs from aqueous dispersion into organic solvents becomes possible by modification of the particle surface with RAFT PN^{i}PAAM.

4.3 A Detailed Investigation of the Strategy Toward Planet–Satellite Nanostructures

4.3.1 The Role of the Linking RAFT Star Polymers

A Qualitative Description. The nanohybrid gold-core–star-polymer-shell particles (i.e. the multifunctional scaffold nanoarchitectures for the attachment of the satellite particles) were characterized by TEM and DLS.

For the preparation of the specimens for microscopy, the nanomaterials were drop-cast from the respective colloidal dispersions on carbon-coated copper grids. Using simple drop-casting, nanohybrids arrange themselves into ordered two-dimensional arrays in some parts of the specimen, while long-range order over extended areas is generally difficult to achieve.[39] However, some regions featuring self-assembled hexagons still allow particle spacing to be quantified. For small ($\overline{2R}$ = ~3 nm) AuNP cores capped with organic ligands, it was shown that particle spacings depend on the particle coordination number, i.e. are different for particles inside or on the edges of self-assembled hexagonal patterns, while this trend becomes much less pronounced for larger ($\overline{2R}$ = ~5 nm) AuNP cores,[239] which are yet much smaller than the citrate-reduced particles used here. Therefore, it was made use here of systematically determining edge-to-edge distances for all particles in nondistorted hexagonal arrangements of nanohybrids with star polymers (Figure 4.3).[71] Although the polymer layer cannot be directly visualized in these micrographs, as it shows only weak electron interaction in addition to the background of amorphous carbon compared with the gold cores, the polymer shell keeps the cores at certain distances which grow

with increasing number average molar mass of the star polymers employed in the functionalization reactions (for absolute numbers of this values, see the quatitative discussion below).[71] This behavior had already been found for linear trithiocarbonate-terminated RAFT polymers.[71,231] Hence, the macromolecular characteristics of the star polymers used in functionalization reactions can be translated to the structures of the resulting core–shell nanocomposites, resulting in well-defined polymer shells (Figure 4.3).

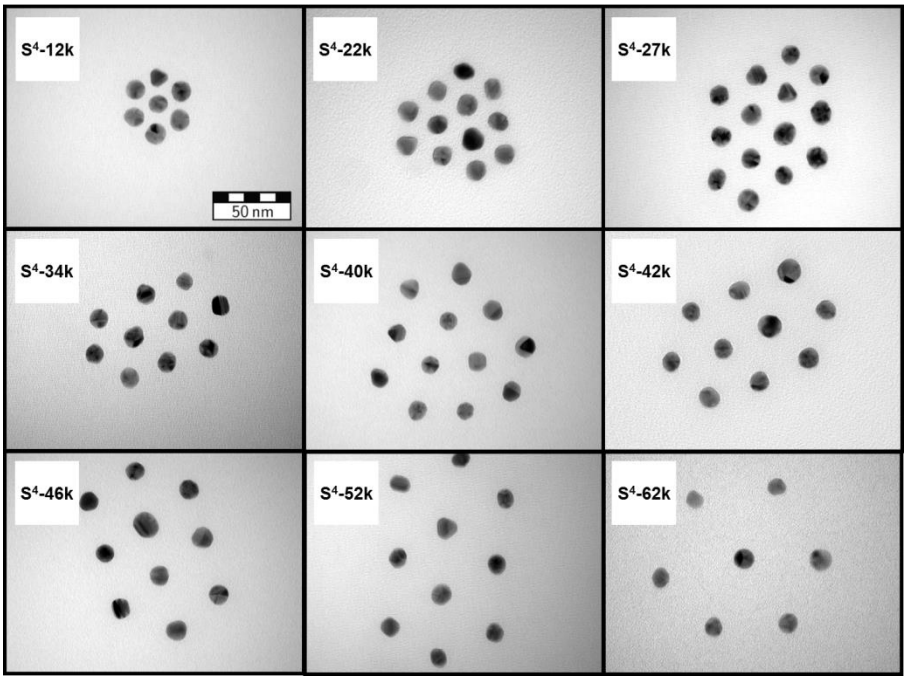

Figure 4.3 TE micrographs of hexagonally assembled patterns of AuNP-core–4-arm-star-polymer-shell hybrid particles. The labels indicate the different star polymers used. The scale bar in the upper left micrograph is valid for all micrographs.

Characterization in colloidal dispersion was undertaken in order to see whether the core–shell particles are present as individual units in the dispersed state. Here, several points need to be considered to obtain reliable results: The experiments have to be conducted in dilute dispersion (generally, < 1‰ by volume is considered sufficient dilution). This is required for avoiding the presence of a static structure factor (i.e., for measuring the self-diffusion of the colloidal particles under investigation) and the samples for DLS characterization had been prepared accordingly. When evaluating intensity-weighed distributions, it needs to be considered

that the scattered intensity has a strong dependency on the object size (for example $I \sim (2R)^6$ for Rayleigh scattering), which leads to the consequence that the larger scatterers contribute much more strongly to the intensity distribution than smaller scatterers. The conversion of such intensity distribution into a number-weighed distribution is, however, impeded, as this would require knowledge about the form of the scattering particles and their refractive indices, which is problematic for inorganic-core–polymer-shell particles.

Considering these aspects, the results from DLS analysis are in line with the presence of core–shell particles as individual units in colloidal dispersion and confirm also the increasing size of the polymer shell with growing star polymer average molar mass, at least for the samples with the smaller molar masses (Figure 4.4A).

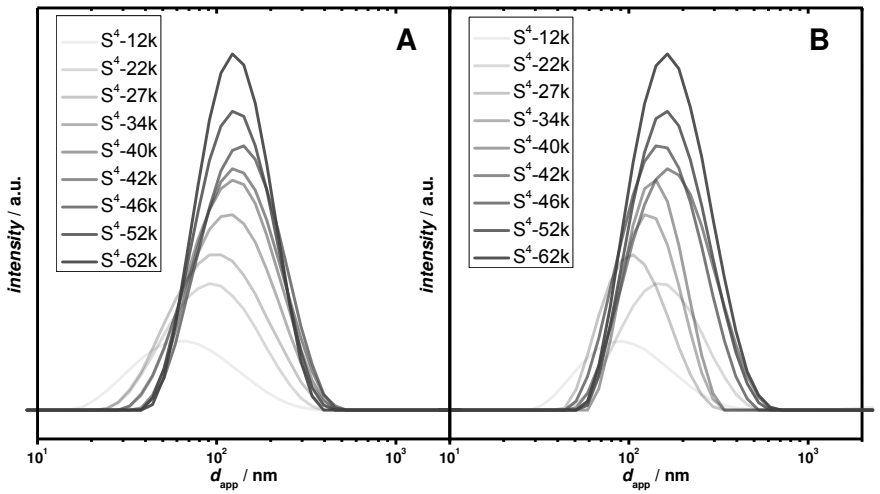

Figure 4.4 Intensity distributions obtained by DLS for the nanohybrids with 4-arm star polymer shells of varying average molar mass (A) and for planet–satellite nanostructures derived therefrom (B). For better visibility, peak maximum values were weighed by the molar mass of the star polymer attached to the surfaces.

One critical question at this point is if the immobilized star polymers still provide free, not surface-bound TTC groups in the polymer shell. It can be reasoned that if at least a fraction of the arms of the immobilized star polymers is not confined permanently to the AuNP surface, then the TTC groups in these dangling arms should still be available for functionalization reactions.

To prove that TTC moieties are exposed in the polymer shell and are

furthermore accessible for functionalization reactions, TOAB-capped AuNPs (~4 nm; see Figure 4.1 for the diameter histogram) made by the two-phase Brust–Schiffrin method were added to the nanohybrid core–shell particles in large excess. TOAB is known to be easily replaced by competitive ligands[185,192,240] (see Chapter 3), which implies only a weak binding strength of TOAB to gold that may result in poor colloidal stability. Hence, in order to shield the outer hemispheres of the satellite particles which are remote from the central planet particle, linear RAFT polymer was added 10 minutes after addition of the Brust–Schiffrin particles. After additional 5 minutes the mixtures were centrifuged for 8 hours at 8600 g. The supernatant almost exclusively contained individual Brust–Schiffrin particles, proving the excellent separation of excess satellite particles by centrifugation.

Figure 4.5 (upper three rows) displays exemplary TEM images of individual planet–satellite particles, derived from 4-arm star polymer. It can already be judged from these exemplary TE micrographs that the planet–satellite edge-to-edge distance within these nanostructures is determined by the average molar mass of the applied star polymer. This conclusion can be clearly drawn from the performed experiments as the planet–satellite distance increase cannot be caused by the linear polymer species, since only one sample of linear polymer with thus constant average molar mass was used throughout the entire series of samples derived from 4-arm star polymers.

It can be observed that these particles also tended to arrange in two-dimensional assemblies after solvent evaporation on the TEM substrate (as can be seen in the lower three rows of Figure 4.5) although these assemblies were not as regular as those found for nanocomposites without satellite particles. The conclusion that these 2-dimensional assemblies indeed form upon solvent evaporation from smaller units present in colloidal dispersion can be drawn from DLS measurements of the planet–satellite nanostructure samples: These DLS data reveal species which are slightly larger, but with sizes of equal order of magnitude to the prescursor core–shell particles (Figure 4.4B). The formation of two-dimensionally ordered films may become most evident from the three TE micrographs in the lowest row of Figure 4.5, which show a strictly alternating arrangement of the two distinct types of NPs, also with adjusted interparticle space between them. It has to be stressed here that no special technique for thin film formation (such as Langmuir-Blodgett transfer etc.) had been applied to prepare these TEM specimens. The ordered two-dimensional particle assemblies form already after simple drop-casting from colloidal dispersion, making these planet–satellite nanostructures promising candidates for the preparation of nanostructured surfaces.

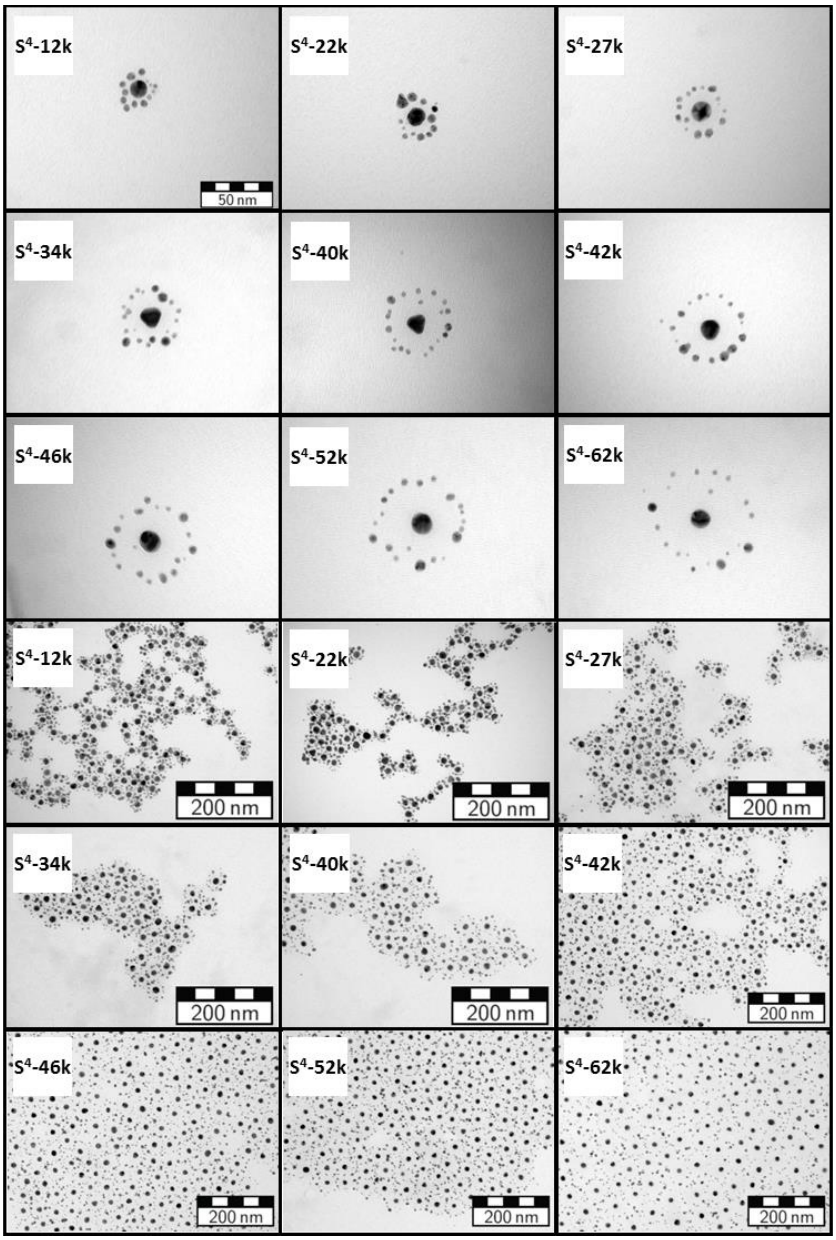

Figure 4.5 TE micrographs of individual planet–satellite nanostructures derived from 4-arm star polymers (upper three rows of this Figure, the scale bar in the upper left micrograph is valid for all micrographs in this upper part showing individual planet–satellite structures) and exemplary micrographs showing 2-dimensionally ordered areas derived from the arrangement of these nanostructures on the surface after drop-casting (lower three rows).

The formation of planet–satellite structures can be regarded as a prove for the hypothesis that a significant proportion of star polymers tethered to the central gold core provide TTC moieties exposed on their polymer shell, i.e. that not all of their branches are permanently attached to the central planet particle surface. To substantiate this claim, it is necessary to prove that indeed the star polymer branch termini are responsible for the planet–satellite nanostructure formation, rather than the monomeric repeating unit. In fact, it is conceivable that the N^{i}PAAM repeating unit present in the backbone of the star polymers used could also interact with the gold surfaces, as weak N–H···Au hydrogen bonds were identified in DFT calculations employing neutral Au_3 model clusters interacting with formamide ligands.[241,242] The prove for the critical role of the star polymer end groups can be achieved by two different control experiments: (i) One experiment can be designed such that the star polymer species are substituted with linear polymer comprising only one TTC-containing end group. As this polymer would be immobilized to the planet particle with this TTC-containing chain end, no TTC groups would be present in the polymer shell assembled around the planet particle, and, consequently, no planet–satellite structure formation would be expected after treatment with Brust–Schiffrin particles (negative control). (ii) A different control experiment would be to keep the overall star polymer structure, but to exchange the monomeric repeating unit to a species which does not provide any hydrogen bond donor functionalities, yet being otherwise similar in its structure and solubility characteristics to N^{i}PAAM (PDMAAM was chosen here for this purpose). If the star polymer end groups are indeed responsible for planet–satellite structure formation, then it would be expected that these structures also form here (positive control). Both types of control experiments had been undertaken (see Figure 4.6).

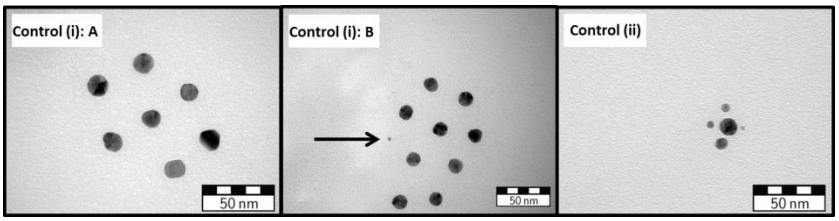

Figure 4.6 TE micrographs after attempted planet–satellite structure formation in control experiments: Micrographs for the negative control are labelled (i); the smaller satellite samples which are found in these experiments (middle image B, indicated by arrow) were very rarely observed within this sample and may be attributed to incomplete removal of free excess satellite particles by the two centrifugation steps. The micrograph labelled (ii) is from the positive control sample and shows a planet–satellite arrangement.

Concluding these control experiments, it appears that the small satellite particles do not attach to hybrid particles with a shell of linear monofunctional RAFT polymer (negative control), while planet–satellite structure formation is observed in the positive control conducted with 4-arm star polymer of DMAAM (M_n = 16 kg mol^{-1}; $Đ$ = 1.24). These observations suggest that indeed the TTC branch termini present in the star polymer structure, not the monomeric repeating units, play the dominant role in the formation of these nanoarchitectures.

The synthetic strategy was also probed with star polymers with different numbers of branches (Figure 4.7). As can be judged from the TE micrographs displayed in Figure 4.7, AuNP core separations in self-assembled hexagons of core–shell particles and within planet–satellite structures again increase within every star polymer series with increasing average molar mass. A detailed analysis of the resulting distance scaling behavior will be performed in the following.

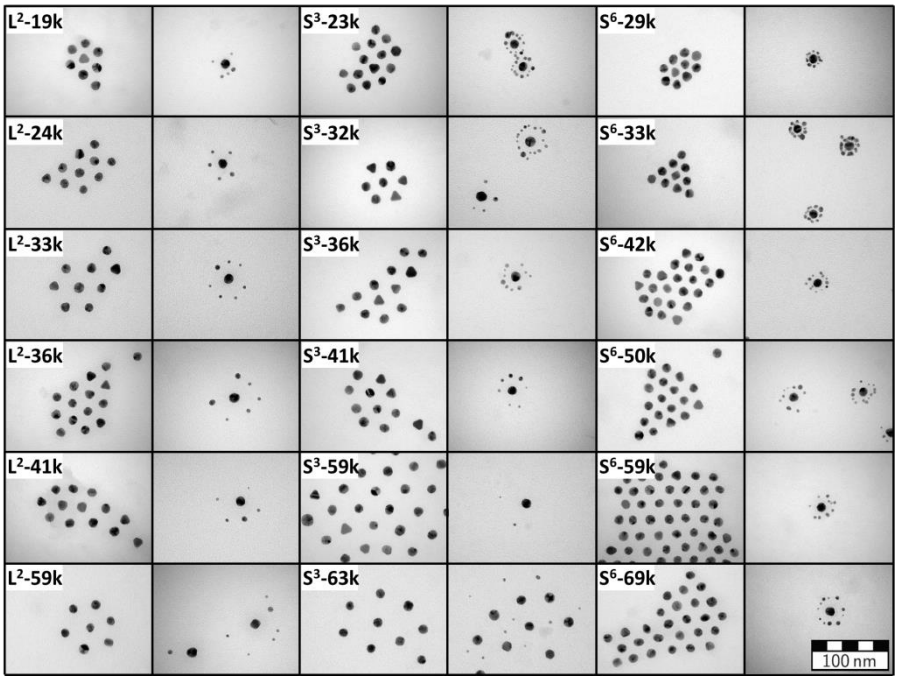

Figure 4.7 TE micrographs of hexagonally assembled patterns of AuNP-core–polymer-shell hybrid particles (columns 1, 3, and 5) and planet–satellite structures derived therefrom (columns 2, 4, and 6). The nanostructures were fabricated by using star polymer featuring 2 (left two columns), 3 (middle two columns) and 6 branches (right two columns).

A Quantitative Description. Several TE micrographs had been analyzed for each of the different samples of core–shell particles and planet–satellite nanostructures. In particular, the scaling of particle distances was investigated systematically in dependence of the average molar masses of the applied polymers and their topology (i.e. star polymer arm number here). In one exemplary case (the 3-arm star polymer case), planet–satellite nanostructures were also analyzed in the colloidally dispersed state via SAXS.

Generally speaking, within every star polymer series, both the interparticle distances in self-assembled hexagons of core–shell particles and the planet–satellite distances increase with increasing average molar mass of the polymer used (see Table 4.1 which lists average values and corresponding standard deviations and Figure 4.10 for the data; interparticle spacing histograms are also given, exemplarily for the samples derived from 3-arm star polymer in Figures 4.8 and 4.9). Here, the former distance is consistently larger than the latter distance for the samples featuring 3-arm, 4-arm, and 6-arm star polymers (the 2-arm case being an exception which will be discussed later). Roughly speaking and neglecting effects of the sample preparation on the TEM supports, the edge-to-edge separations in hexagonal core–shell particle arrangements should be twice as large as the thickness of one polymer layer, assuming that there is no polymer shell compression upon core–shell particle assembly. On the other hand, the edge-to-edge distances in isolated planet–satellite structures should be as large as the thickness of the layer covering the planet particle, provided that the satellites bind to the outside of this layer, rather than being incorporated in this layer. Hence, a value of 0.5 may be expected for the ratio of these two values (the determined ratios are given in Table 4.1). Indeed, values well around 0.5 are found for the star polymer samples featuring 3, 4, and 6 branches. The values for this ratio might be even slightly smaller than 0.5, especially for low star polymer molar masses with a tendency of these values becoming slightly larger than 0.5 with increasing star polymer molar masses. The observation of values smaller than 0.5 is reasonable, considering that the TE micrographs of planet–satellite structures provide two-dimensional projections of the investigated objects. A trend toward higher values for this ratio with increasing polymer molar mass may have its cause in an incresed compression of the polymer shell in self-assembled hexagons with increasing molar masses of immobilized polymer,[239] in particular because planet–satellite distances were always measured for isolated planet–satellite structures (with thus no compression) in the experiments conducted here. To sum up, values that are found for the ratio

Table 4.1 Results from the analysis of TE micrographs.

Polymer	Interparticle separation[a] / nm	#[b]	Planet–Satellite distance[c] / nm	#[b]	Ratio[d]	Avg. # satellites per planet
L^2-19k	8.7 ± 2.1	325	6.4 ± 2.0	194	0.74	4.6
L^2-24k	10.9 ± 2.3	249	9.2 ± 2.5	221	0.84	4.1
L^2-33k	15.5 ± 2.9	189	13.9 ± 2.7	217	0.90	4.1
L^2-36k	12.7 ± 2.5	423	16.5 ± 4.0	222	1.30	4.8
L^2-40k	14.8 ± 3.1	275	19.3 ± 4.6	178	1.30	3.8
L^2-53k	17.9 ± 4.8	125	23.8 ± 6.7	135	1.33	1.8
S^3-23k	8.3 ± 2.0	338	4.3 ± 1.7	330	0.52	7.6
S^3-32k	10.9 ± 2.0	288	8.2 ± 2.3	301	0.75	7.8
S^3-36k	12.4 ± 2.7	232	8.4 ± 2.4	215	0.68	6.4
S^3-41k	15.4 ± 2.9	308	10.8 ± 2.8	123	0.70	5.8
S^3-59k	21.7 ± 3.9	366	15.1 ± 4.2	104	0.70	2.1
S^3-63k	27.7 ± 4.6	198	16.0 ± 4.5	102	0.58	1.0
S^4-12k[e]	5.8 ± 1.5	471	2.6 ± 1.6	167	0.45	n.d.
S^4-22k[e]	8.5 ± 1.7	290	3.5 ± 1.5	266	0.41	n.d.
S^4-27k[e]	12.6 ± 2.0	382	6.0 ± 1.9	199	0.48	n.d.
S^4-34k[e]	15.4 ± 2.2	448	8.0 ± 2.6	208	0.52	n.d.
S^4-40k[e]	19.4 ± 1.5	287	10.9 ± 2.7	255	0.56	n.d.
S^4-42k[e]	20.1 ± 3.1	318	10.9 ± 3.2	284	0.54	n.d.
S^4-46k[e]	22.5 ± 3.0	342	14.7 ± 3.5	357	0.65	n.d.
S^4-52k[e]	26.7 ± 3.7	151	17.9 ± 4.1	224	0.67	n.d.
S^4-62k[e]	33.4 ± 4.2	180	22.4 ± 5.7	208	0.67	n.d.
S^6-29k	4.4 ± 1.2	338	1.4 ± 1.0	350	0.32	9.5
S^6-33k	5.5 ± 1.5	290	2.2 ± 1.4	576	0.40	10.5
S^6-42k	7.0 ± 1.7	409	3.5 ± 2.1	479	0.64	9.2
S^6-50k	8.6 ± 1.9	402	6.0 ± 2.2	381	0.70	8.2
S^6-59k	10.1 ± 2.2	455	6.1 ± 2.1	350	0.60	7.7
S^6-69k	10.4 ± 2.3	400	9.2 ± 2.4	348	0.88	10.4

[a]Determined as particle edge-to-edge separation in undistorted hexagonal arrangements. [b]Number of distances measured. [c]Determined as particle edge-to-edge separation in isolated planet–satellite nanostructures. [d]The ratio of planet–satellite distance / interparticle separation. [e]Note that a different shielding linear polymer was used for the preparation of planet–satellite samples derived from the 4-arm star polymer.

discussed above are consistent with the hypothesis that the satellite particles which are introduced by attaching them to planet particles covered with star polymer shells indeed bind to the outside of this polymer shell, rather than penetrating deep into this shell (which would be reflected in a value significantly smaller than 0.5 for the ratio discussed above), at least in the configurations which are obtained after preparing the samples on TEM grids.

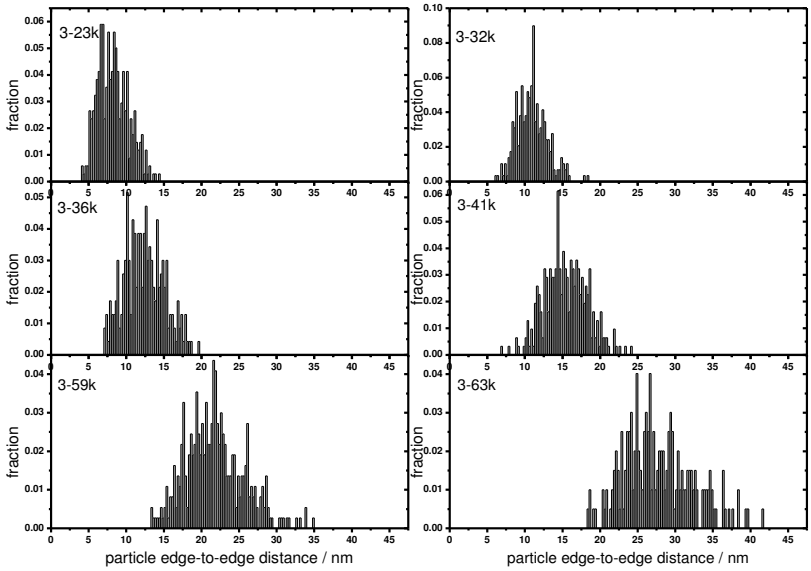

Figure 4.8 Histogram of particle edge-to-edge separations in hexagonal arrangements for the different 3-arm star polymers as determined by TEM. (The binning step size reflects the resolution of the micrographs at the magnification at which micrographs had been taken.)

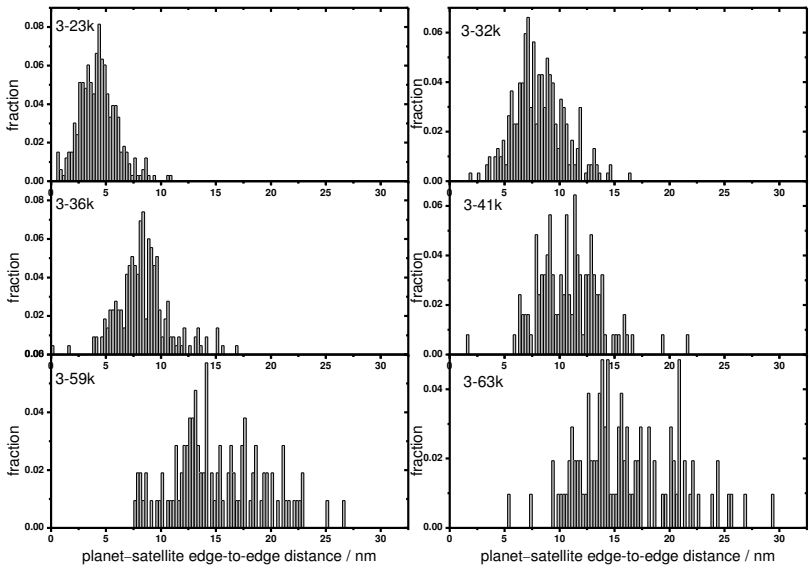

Figure 4.9 Histogram of planet–satellite edge-to-edge separations for the different 3-arm star polymers as determined by TEM. (The binning step size reflects the resolution of the micrographs at the magnification at which micrographs had been taken.)

In the case of the samples featuring telechelic polymer (2 star branches), measured planet–satellite separations can take values that are even larger than the corresponding edge-to-edge distances in self-assembled hexagons of the respective core–shell particle precursors, which is an unexpected result from the first view. To understand this behavior, the particle separations in core–shell particle hexagonal arrangements were compared with values obtained from samples that feature shells of linear monofunctional RAFT polymer of N^{i}PAAM, which had been determined earlier.[71,231] Between both types of core–shell nanohybrids, the only distinction is the presence of TTC end groups on both or only one terminal of the linear macromolecules. Yet, interparticle separations in hexagonal arrays are significantly smaller for polymer shells comprising telechelic polymer compared with linear polymer featuring only one TTC end group. Such behavior had already been found when multifunctional linear RAFT polymers with multiple TTC groups evenly incorporated along the polymeric backbone were compared with monofunctional RAFT polymers, and the different behavior was attributed to the formation of polymer loops on the NP surfaces.[71] Following similar arguments as explicated in this earlier work, it can be concluded that polymer loops do also form when telechelic polymer is immobilized on the surfaces of AuNPs from citrate-reduction. However, since planet–satellite nanostructures do also form when core–shell particles with a shell of telechelic polymer are treated with satellite particles and as it could be deduced from control experiments (see above) that free TTC groups in the polymer shell are necessary for planet–satellite structure formation, it can be concluded that only a fraction of the immobilized telechelic polymers forms loops on the NP surface, the remaining fraction attaching with one chain end only and providing free TTC end groups. These conclusions drawn from the thorough analysis of TE micrographs are fully consistent with simulation results for these structures, which had been obtained by Qiyun Tang and Marcus Müller, and will be published in a forthcoming publication.[243] These simulation results indicate that the fraction of polymer loops increases with increasing interaction strength of the terminal end groups with the particle surface (see also Section 2.2 for the determination of the strength of this interaction.)

It may well be that the telechelic polymers attaching with one end group do not contribute much to the interparticle repulsive potential, such that edge-to-edge distances in self-assembled hexagons of core–shell particles would be determined mostly by the polymer loops on the surfaces, while planet–satellite distances would be determined by the length of the

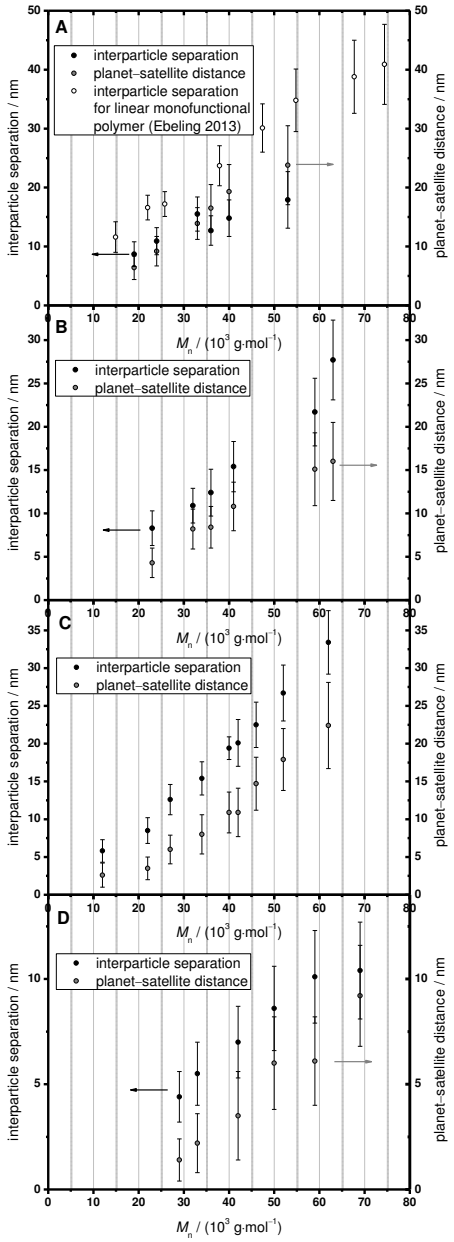

Figure 4.10 Scaling of interparticle edge-to-edge distances in self-assembled arrays of core–shell particles and of planet–satellite edge-to-edge distances with the average molar mass of the employed telechelic (A), 3-arm star (B), 4-arm star (C), and 6-arm star (D) polymer. Data shown as empty circles in plot A is taken from literature.[71]

telechelic polymer. This could explain the exceptional behavior of the samples derived from telechelic polymer.

Another topological effect can also be observed comparing 2-arm, 3-arm, and 6-arm star polymers (for the 4-arm star polymer case, a different shielding linear polymer was used and this case is therefore not considered for this comparison): It is interesting to note that the average number of satellite particles per planet particle increases with increasing star polymer arm number (around 4 for the 2-arm case, an exception being the sample with the highest molar mass, around 7 for the 3-arm case, exceptions being the two samples with highest molar masses, and around 9 for the 6-arm case, see Table 4.1) which, again, reflects the fact that satellite particle attachment is caused by the interaction with the TTC end groups. Hence, a higher number of end groups in the polymer shell leads to the attachment of more satellite particles under otherwise equal conditions.

The planet–satellite edge-to-edge distances can also be analyzed in dependence of the star polymer arm length: See Figure 4.11 which plots these distances as a function of the number average molar mass of individual star polymer branches. Such analysis reveals that the data for the 2-arm, 3-arm, and 6-arm star polymer cases can be collapsed to one master curve. Only the data for the 4-arm star polymer are slightly off this master curve, but it cannot be decided here if this is an effect from the star polymer structure or from the different shielding linear polymer used for the preparation of planet–satellite structures derived from the 4-arm star polymer. Still, the very good match of the data from samples derived from 2-arm, 3-arm, and 6-arm star polymer indicates that the planet–satellite edge-to-edge distance determined by TEM is controlled by the star polymer arm length. Thus, this result provides another piece of compelling evidence that satellite particles are attached to the central planet particle by interconnection with the applied star polymer species.

To confirm the presence of planet–satellite structures and for obtaining distance scaling data in the dispersed state, SAXS experiments were undertaken, exemplarily for the 3-arm star polymer case. Due to the much higher contrast of gold to the solvent compared with the organic polymer, it can be assumed that only the inorganic part of the nanostructures contributes to the scattered intensity (see also Section 3.3). Experiments were performed under dilute conditions, such that the intensity profile reflects the particle form factor.

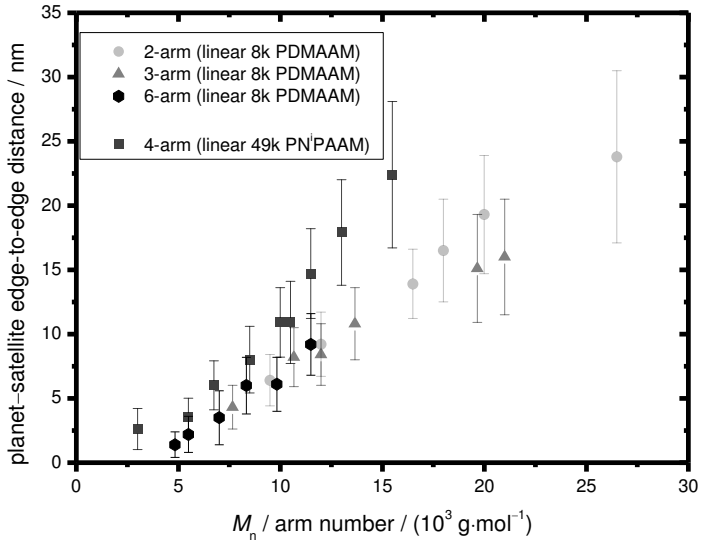

Figure 4.11 A plot of planet–satellite edge-to-edge distances as a function of the number average molar mass of star polymer arms.

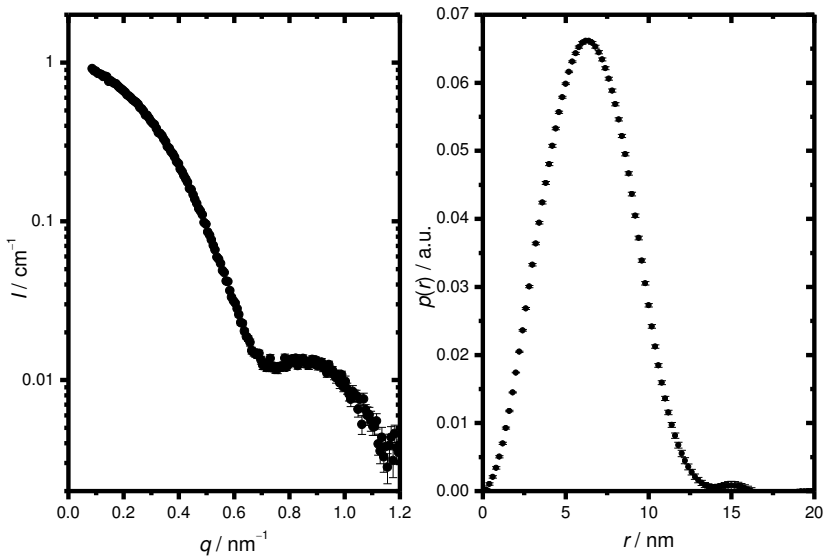

Figure 4.12 Small-angle X-ray scattering curve (left) and corresponding pair-distance distribution function (right) for core–shell particles with a shell of L^1–49k.

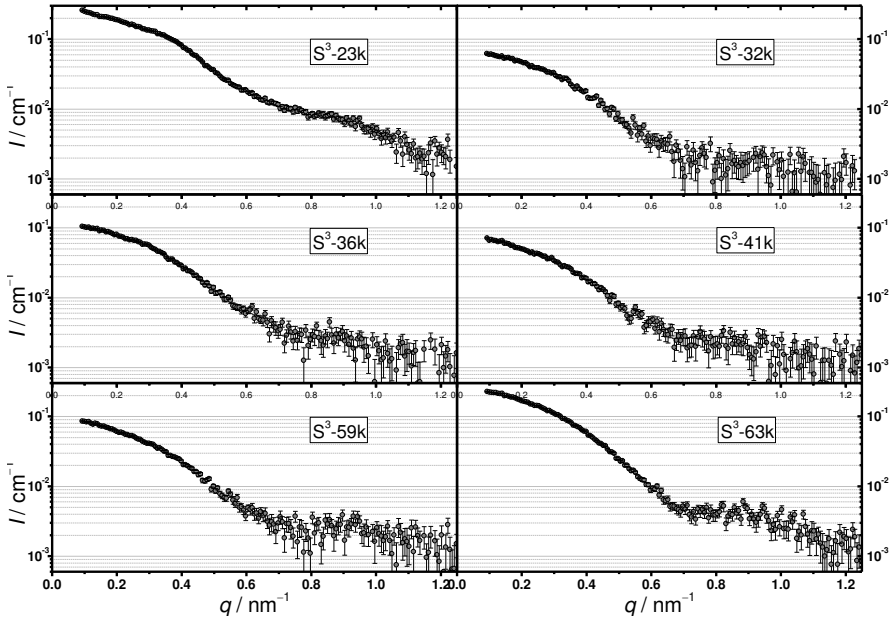

Figure 4.13 Small-angle X-ray scattering profiles for planet–satellite structures derived from 3-arm star polymers.

Figure 4.12 displays the small-angle scattering curve for core–shell particles with a shell of linear monofunctional polymer (M_n = 49 kDa, $Đ$ = 1.18)[244], i.e. individual planet particles without satellites attached. This scattering curve features distinct oscillations, which are indicative of a relatively narrow particle size distribution. In comparison, Figure 4.13 shows how the shape of the scattering curve is altered for planet–satellite structures with respect to individual planet particles. It is, however, difficult to judge these differences in reciprocal space, due to the abstract nature of this domain. Real-space information about the samples can be obtained after indirect Fourier Transformation (IFT)[201] of the intensity profiles into the corresponding pair-distance distribution functions (PDDFs), $p(r)$[194,245,199,246] (see Figure 4.14 and right side of Figure 4.12):

$$p(r) = \frac{1}{2\pi^2}\int_{q=0}^{\infty} I(q)\cdot qr\cdot \sin(qr)\,\mathrm{d}q. \qquad (4.1)$$

The function $p(r)$ is a measure for the number of distances r within a scattering object of homogeneous electron density and, since only the gold contributes to the scattering to a good approximation, the $p(r)$ function represents the number of distances within this inorganic part.

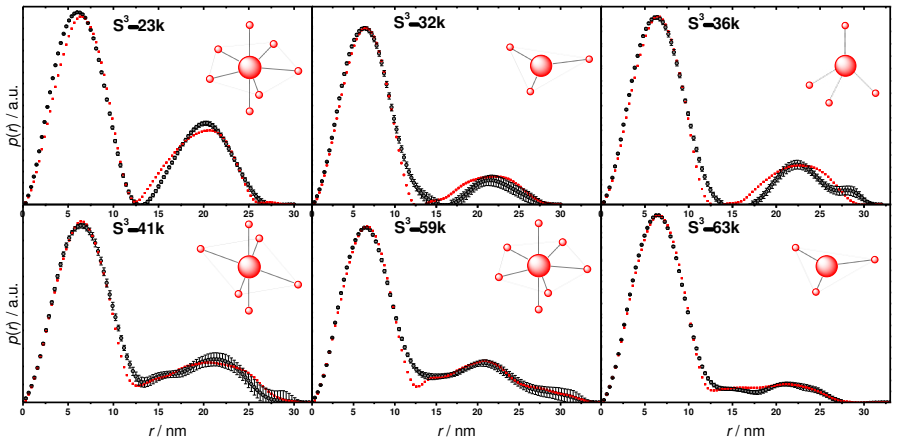

Figure 4.14 Experimental PDDFs (gray circles) for planet–satellite nanostructures derived from 3-arm star polymer and PDDFs of models calculated based on equation (4.2) (red data points). Insets in the upper right of the single plots schematically illustrate the arrangement of satellites around the planet particles in the structure models.

All experimental $p(r)$ functions displayed in Figure 4.14 feature a large peak with a maximum around 6.4 nm. This peak predominantly contains contributions from the large planet particles (see for comparison the plot on the right side of Figure 4.12 for the PDDF of core–shell particles with planet particle cores). Toward larger distances, a second maximum of the PDDFs is observed in all cases. This maximum can be attributed to the presence of distances between planet particles and surrounding satellite particles, on one hand, and between different satellite particles which are attached to the same planet particle, on the other hand. In order to draw conclusions about planet–satellite spacings in the dispersion, multibody scattering curves for different structure models had been calculated based on the Debye expression:[199]

$$I(q) = C \cdot \sum_{i=0}^{N} \sum_{j=0}^{N} V_i V_j \cdot F_i F_j \cdot \frac{\sin(q \cdot d_{ij})}{q \cdot d_{ij}}, \qquad (4.2)$$

where C is a constant, V the particle volume, and d_{ij} the center-to-center distance between the i-th and j-th particle. Assuming spherical particles with radius R, F takes the form:

$$F(q,R) = \frac{3\left(\sin(qR) - qR \cdot \cos(qR)\right)}{(qR)^3}. \qquad (4.3)$$

The constant *C* was chosen such that model scattering curves had the same scattering intensity at zero scattering angle, *I*(0), as desmeared experimental scattering curves, thus ensuring equal integral values of experimental and model PDDFs, due to the Fourier relation:[199]

$$I(0) = \lim_{q\to 0} 4\pi \cdot \int_{r=0}^{\infty} p(r) \cdot \frac{\sin(qr)}{qr} \mathrm{d}r = 4\pi \cdot \int_{r=0}^{\infty} p(r) \mathrm{d}r. \quad (4.4)$$

The multibody structures consisted of spherical planet particles with a radius of 6.2 nm (best fit to the desmeared scattering curve for core–shell particles) and spherical satellite particles of 2.0 nm radius[192,240] (dispersities in particle sizes were neglected). Multibody scattering curves calculated according to equation (4.2) were next converted into PDDFs via IFT and compared with experimental PDDFs. While this comparison is very sensitive to the number of satellites attached to the planet particle (see exemplarily in Appendix Figure D1, shift in the ratio of the integral values for the two peaks) and also to the planet–satellite distance (see exemplarily in Appendix Figure D2, shift in the position of the peak at larger *r*), differences between calculated PDDFs coming from the alternate positioning of the satellites are only marginal (see Appendix Figure D3). Therefore, a fixed number of satellites at a given distance were always positioned forming typical coordination polyhedra, leading to a uniform distribution of satellite particles (for example, 7 satellites were arranged in a pentagonal bipyramidal fashion).

Figure 4.14 displays experimental and model PDDFs. For the three samples featuring 3-arm star polymers with the smallest molar masses (i.e. samples with star polymers S^3-23k, S^3-32k, S^3-36k) the experimental data can be fitted relatively well using models with a set number of satellites as well as one fixed planet–satellite separation. This observation is remarkable as it suggests that planet–satellite distances are indeed narrowly distributed for these samples in colloidal dispersion. For the samples with star polymers of higher molar masses (i.e. samples with star polymers S^3-41k, S^3-59k, S^3-63k), good agreement between experiment and models is only achieved when model structures with different planet–satellite spacings are mixed, suggesting a broader planet–satellite distance distribution for these samples. Table 4.2 displays planet–satellite edge-to-edge distances and numbers of satellite particles in model structures that fitted the experimental data best.

The numbers of satellite particles in the model structures used to fit the experimental SAXS data are in reasonable agreement with the values determined from microscopy (Table 4.1). Unlike for the microscopy data,

Table 4.2 Characteristics of the planet–satellite model structures which fitted the experimental SAXS data best and which are also schematically illustrated in Figure 4.14.

Polymer	Average planet–satellite edge-to-edge distance / nm	Range of distances employed in model	Number of surrounding satellite particles
S^3-23k	11	–	7
S^3-32k	13	–	3
S^3-36k	14	–	4
S^3-41k	11 ± 5	7–14 nm	6
S^3-59k	11 ± 6	2–22 nm	7
S^3-63k	9 ± 4	4–14 nm	3

on the other hand, planet–satellite distances do not increase strictly with increasing average molar mass of the star polymers.

To explain this discrepancy, the morphology of the surrounding polymer shell in core–shell structures after casting on a solid substrate will be analyzed in more detail in the following section.

4.3.2 The Morphology of the Star Polymer Canopy in AuNP-Core–Star-Polymer-Shell Nanohybrids

In Section 4.3.1, structural information about hybrid nanostructures was obtained from TEM and SAXS. Since both the electron and X-ray beam interact much stronger with gold rather than with the polymers, these techniques provide direct information merely about the inorganic part of the nanohybrids. The polymer canopy covering the inorganic particles can be in principle visualized via AFM, as emphasized by a recent systematic AFM study of similar structures.[247] Figure 4.15 displays representative micrographs of gold-core–star-polymer-shell particles, exemplarily for the sample with star polymer S^3-36k. It can be seen from image (A) that the core–shell particles also tend to assemble into ordered island structures on the glass slides used for sample preparation, as had been observed in TE micrographs where the particles were deposited on a thin film of amorphous carbon (Figure 4.7). A region of the specimen that contained mostly isolated core–shell particles (Figure 4.15B) was investigated for analyzing mechanical properties (DMT modulus, without prior calibration, since these measurements were intended to serve qualitative purpose only) of the hybrid particles (Figure 4.15C). As can be judged from Figure 4.15C, a hard particle core is surrounded by a softer shell (see also Section 1.2), providing

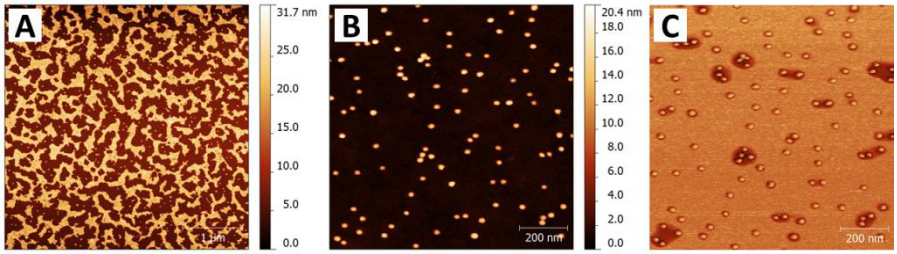

Figure 4.15 Exemplary AF micrographs for AuNPs covered with a shell of 3-arm star polymer S^3-36k: Height-contrast images show an overview (A) where core–shell particles assembled into island structures after drop-casting and isolated (B) core–shell particles at higher magnification. Image (C) is obtained by measuring the DMT modulus for the section shown as height image in (B).

direct evidence for the presence of the polymer shell, which could not be directly visualized in the TE micrographs presented in Section 4.3.1. Although such AFM analysis presented here gives sound qualitative results, quantitative analysis is complicated by tip-sample convolution,[248] roughness of the substrate surface and the long measurement time which would be required to obtain a sufficient number of AF micrographs for the different samples. It was, therefore, intended to compliment the data set from TEM analysis with additional information about the polymeric shell from TGA measurements.

From data for particle spacings in self-assembled hexagons of gold-core–star-polymer-shell particles (see TEM analysis in the previous section), it is in principle possible to determine grafting densities σ of the macromolecules attached to the AuNP surfaces, if a model for the polymer shell is available.[52,150,249] A conceivable model is the volume filling hexagonal packing model with constant film thickness,[250] which avoids unfavorable free interstitial regions[251] in the hexagonal arrays:

$$\sigma = \frac{\left[\frac{\sqrt{3}}{2} d^2 \cdot h - \frac{\pi}{6} \cdot (2R)^3\right] \cdot N_A \cdot \rho}{M_n \cdot \pi (2R)^2} \qquad (4.5)$$

Here, d is the interparticle center-to-center distance, h the film thickness, N_A the Avogadro constant, and ρ the polymer bulk density. Investigating isolated AuNP-core–polystyrene-shell particles, Vaia and coworkers have shown that the overall volume of a polymer shell covering an AuNP as measured by AFM is in line with the assumption of a polymer shell of bulk density.[247] Therefore, although the situation is different in TEM due to the application of high vacuum, polymer bulk density (1.1 g cm^{-3} for

PN^{i}PAAM) should be a good estimate for the density of the polymer shell. Grafting densities are also directly accessible via TGA measurements.[249,250,252]

Table 4.3 lists determined (via TGA, see Figure 4.16) grafting densities for 3-arm star polymers on the larger planet particles as well as film thickness values calculated from TEM results (interparticle separations, Table 4.1) according to equation (4.5), taking the distribution in gold core diameter and particle spacing (Figure 4.8) into account. A trend of decreasing grafting density with increasing molar mass is commonly observed when linear polymers with one end group are grafted to nanoparticles,[72,253] and this behavior had been explained based on thermodynamic considerations.[72] The determined σ values for 3-arm star polymers show a similar trend of decreasing grafting density with increasing average molar mass and lie significantly below values determined by Boyer *et al.* (0.92 macromolecules per nm^2 of citrate-reduced AuNPs for M_n of approx. 26 kDa),[252] and also Liang *et al.* (0.75–1.04 macromolecules per nm^2 for AuNPs of different sizes and M_n of approx. 5 kDa)[254] for TTC-terminated linear PN^{i}PAAM grafted to AuNPs, although direct comparison is difficult, since slightly different grafting procedures as well as different RAFT Z groups were employed in these studies and within this work. The calculated values for the average film thickness, h, assuming the volume filling packing model decrease with increasing star polymer molar mass and lie beyond the average diameter ($\overline{2R}$) of the gold cores, with the sole exception of the sample with star polymer S^3-23k with the smallest star polymer molar mass. This leads to the rational conclusion that the interparticle space is not completely filled with polymer[67] (with the sole exception of the sample with star polymer S^3-23k) which had been observed by means of AFM,[52,53,150]

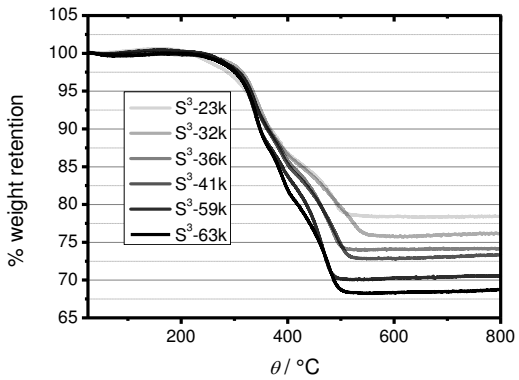

Figure 4.16 Results from thermogravimetric analysis of nanohybrid core–shell particles with planet particle gold cores and 3-arm star polymer shells.

and SEM[72] for similar systems (see also Figure 1.1 in Section 1.2). The polymeric layer probably adopts the shape of a compact shell in close proximity to the AuNP core and farther from the core extends as a flatter polymer film after drop-casting on a substrate, as also indicated by elemental mapping of the backbone element carbon in gold-core–linear-polymer shell particles (see Section 1.1, Figure 1.2).

Table 4.3 Grafting densities of 3-arm star polymers on large planet particles as determined via TGA and film thickness values, h, according to equation (4.5).

Polymer	σ^{TGA} / (macromolecules nm^{-2})	h / nm
S^3-23k	0.36	17.6
S^3-32k	0.26	10.7
S^3-36k	0.26	9.3
S^3-41k	0.24	7.0
S^3-59k	0.19	3.9
S^3-63k	0.19	2.9

The decreasing grafting densities with increasing star polymer average molar mass may also be an explanation for the distance scaling behavior in colloidal dispersion as revealed via SAXS (Table 4.2): The decrease in the grafting density observed for the larger molar masses may possibly lead to insufficient long-term stability of the prepared nanostructures, and the apparently decreasing planet–satellite distances found in SAXS analysis may therefore be considered as a result of aging effects.

The results above were deduced from analyzing nanohybrids with core–shell morphology. In the more complicated case of planet–satellite nanostructures, structural information about the polymeric part can be obtained from STEM-SI (Figure 4.17). The results from this elemental mapping revealed co-localization of sulfur both with the large planet particles as well as with the smaller satellite particles (Figure 4.17C). This is fully consistent with the results obtained in Section 2.1 from the analysis of core–shell particles featuring larger planet particles alone and is in accordance with the assumed planet–satellite assembly mechanism as illustrated in Scheme 4.1. From the carbon map (Figure 4.17B) for the planet–satellite nanostructures, there can be a distinct ring observed around the AuNP cores, comparable to the situation in simpler core–shell particles (Figure 2.2). The polymer canopy has largest height around the planet particle core. A flatter polymer film, which wets the graphene film of the substrate, extends between the planet particle and the surrounding satellites.

The conclusions drawn in this section about the polymer canopy

morphology in nanohybrid core–shell particles and planet–satellite structures are summarized in a schematical illustration which is shown in Figure 4.18.

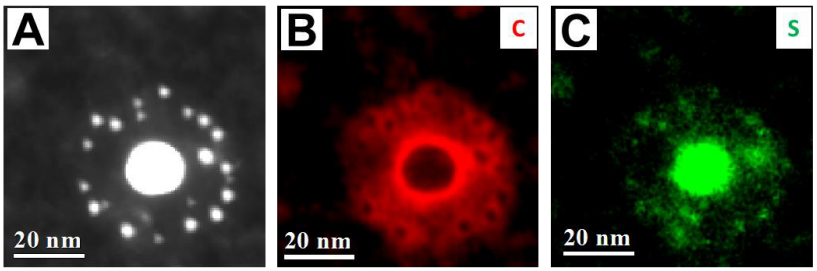

Figure 4.17 STEM dark-field image (A) of an isolated planet–satellite nanostructure. Image (B) and (C) are obtained via STEM-SI and show maps of the elements carbon (red color) and sulfur (green color). S^4-46k was used as the star polymer in the preparation of these structures.

Figure 4.18 Schematical illustration of the polymer shell morphology in self-assembled layers of simple core–shell particles (A) and in planet–satellite nanostructures (B).

4.3.3 The Role of the Linear Polymer Species

In the modular synthetic procedure for synthesizing planet–satellite nanostructures, star polymers fulfill the task of connecting central planet particles with the surrounding satellite particles. This conclusion could be drawn from presented experiments showing increasing planet–satellite distances with increasing star polymer molar mass (see Section 4.3.1).[244] However, from the analysis performed in the previous sections, the exact role of linear RAFT polymer used in this synthetic procedure could not be fully resolved. Since the linear polymer was found to be required to provide colloidal stability of the nanostructures, making their purification via centrifugation possible, it can be reasoned that the linear polymer shields the surfaces of the satellite particles introduced before. However, this could not be directly proven from the prior analyses nor could the question be answered whether the linear polymer also attaches to the central planet particles, by penetrating through the star polymer shell (see Scheme 4.2).

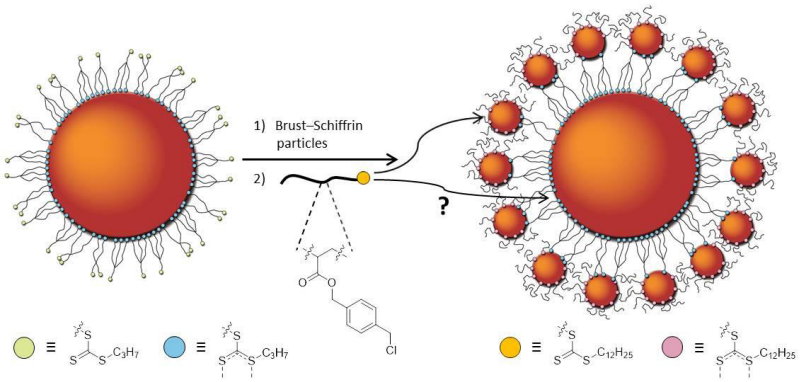

Scheme 4.2 Synthetic scheme for the formation of planet–satellite nanostructures using functional polymer containing benzyl chloride moieties in the monomeric repeating units. Introduction of this functional linear polymer and its localization within the planet–satellite nanostructures is a particular aim of this section.

Answering this question is of importance, because the introduction of linear polymer opens the possibility of equipping these nanostructures with additional chemical functionality.

Within this section, the functionalization of planet–satellite nanostructures by specially designed macromolecules is presented. These macromolecules were chosen such that they (i) contain reactive functional groups and (ii) are suited for the analysis of their lateral distribution within the resulting nanostructures. To localize macromolecular species within the planet–satellite nanostructures, electron energy-loss spectroscopy and STEM-SI had been employed.

As side-chain functional linear polymer, trithiocarbonate-terminated RAFT polymer containing chlorine in the monomeric repeating units was synthesized to have this polymer species "labeled" with that element for deriving its distribution in the resulting planet–satellite nanostructures. The monomer 4-vinylbenzyl chloride (VBC) is well-established in RAFT polymerizations both in homogeneous solution[70,255,256] and initiated from solid surfaces.[70] Investigating different polymerization conditions for RAFT-mediated VBC polymerization, it turned out, however, that it was difficult to achieve at the same time high molar masses and small dispersities.[70] To retain the established benzyl chloride motif in the monomer structure and at the same time to yield better control over molar mass distributions, an acrylate-type monomer carrying benzyl chloride in its side chain (4-(chloromethyl)benzyl acrylate, 4-ClMeBnA) had been synthesized. RAFT polymerization of this monomer was conducted using

RAFT agent **L**[1] as mediating agent.[192] As can be seen from the SEC analysis results (Table 6.2), polymer with reasonably small dispersity is obtained. Since the number average molar mass value obtained via SEC was derived using polystyrene calibration and since the molecular weight of the 4-ClMeBnA monomer is about a factor of two larger compared with styrene, it is expected that the SEC result underestimates the true average molar mass value of P(4-ClMeBnA). Consistent with that, the theoretical molar mass (27 kDa, Table 6.2) is significantly larger compared with the SEC result and should be closer to the true average molar mass value.

Elemental mapping via STEM-SI had been performed to locate the chlorine-containing (macromolecular) species (Figure 4.19B) within the nanostructures formed. From such analysis, there appears to be a high abundance of this element in regions where many satellite particles are located in close proximity or close to satellite particles of comparatively large diameter. Such finding supports the earlier claim that linear polymer attaches to the surfaces of the satellite particles. The presence of chlorine is also revealed around the larger planet particles. These results show that the linear polymer can be used to introduce special chemical functionality (in this case the benzyl chloride motif) to planet–satellite nanostructures. Specifically, the benzylchloride moiety introduced here in the form of linear homopolymer of 4-ClMeBnA is activated toward reaction with nucleophiles and may enable post-polymerization modification of this surface-bound polymer in planet–satellite nanostructures.[257,258] This possibility underlines the versatility of the synthetic route toward planet–satellite nanostructures, in which planet–satellite distances can be controlled by adjusting the degree of polymerization of star polymer (see Section 4.3.2) and where the overall nanostructure can be functionalized through introduction of the linear polymeric species.

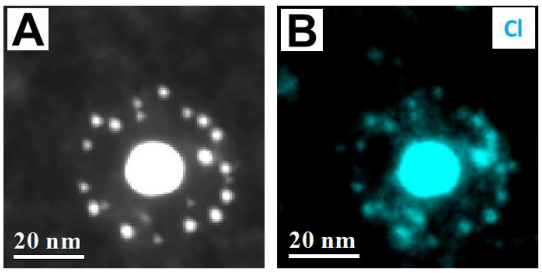

Figure 4.19 STEM dark-field image (A) of an isolated planet–satellite nanostructure (the same as already shown in Figure 4.17). Image (B) is obtained via STEM-SI and shows a map of the element chlorine (blue color).

4.3.4 The Scope of the Presented Design Strategy

As had been detailed in section 4.2, the synthetic strategy for the formation of planet–satellite nanostructures follows a modular approach, which implies that the individual building units can be varied independently from each other in their shape and composition. Within this section, two straightforward examples are included to illustrate this point.

The planet particles which are made by the citrate-reduction method can be varied in size by modifying the synthetic procedure used.[229] Using larger (~50 nm in diameter) AuNPs as planet particles, the formation of planet–satellite nanostructures proceeds smoothly as with the smaller planet particle AuNPs (~13 nm) that were used in the experiments presented above (see Figure 4.20), although the planet particles were not as uniform in size and regularly shaped as in the cases described earlier. Nevertheless, this result shows the general possibility of changing the size of the constituent planet particle building block.

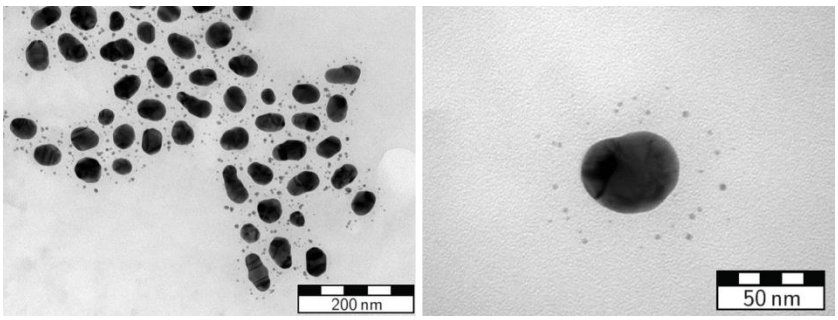

Figure 4.20 TEM image of planet–satellite nanostructures assembled from large planet particles (~50 nm), using star polymer S^4-46k.

It should also be mentioned here that the chemical composition of the particle building blocks can as well be varied. Following the same design strategy as presented in Section 4.2, Wentao Peng realized nanostructures in which the central AuNP planet particle is surrounded by AgNP satellite particles. Also in this bimetallic system, the possibility of precisely adjusting the Au-planet–Ag-satellite separation by using star polymer with defined degree of polymerization is maintained.[259]

Together with the possibility of using planet particles of larger sizes and satellite particles made from a second chemical element, it was already

demonstrated in Section 4.3.1 the possibility of using star polymers of PDMAAM instead of PN^{i}PAAM (Figure 6.6 control (ii)), and also the linear polymer species can take different forms (PN^{i}PAAM, PDMAAM, P(4-ClMeBnA). This means that it is in principle possible to adapt each of the single building units that build up the overall planet–satellite nanostructure for specific requirements. This possibility renders the design strategy toward planet–satellite nanostructures presented and analyzed in this Chapter 4 very versatile and flexible and therefore applicable as a platform methodology for the efficient preparation of a large library of different planet–satellite structures.

Chapter 5
Closing Remarks

5.1 Conclusions

Within this work, the state of the art in the field of nanocomposites with polymers from controlled radical polymerization had been reviewed (Chapter 1) and model systems had been developed toward an improvement of the understanding of the specific interaction between RAFT polymers and gold nanoparticle surfaces (Chapter 2). Furthermore, two systems for the fabrication of ordered nanohybrid structures, which are based on specially designed RAFT polymers, had been developed and characterized in detail (Chapters 3 and 4).

Although the conclusion that the RAFT moiety can be exploited as an anchoring group for the attachment to gold surfaces had already been drawn from the investigation of small molecule model systems featuring trithiocarbonate- and dithioester-based RAFT agents before, this work provides, to the best of my knowledge, the first direct evidence for this specific interaction between RAFT polymers and gold nanoparticles. This conclusion was drawn from the observation of the co-localization of the element sulfur (present in the RAFT polymers' trithiocarbonate end groups) with the lateral position of gold cores in hybrid core–shell particles that were analyzed via STEM-SI. The interaction strength of trithiocarbonate groups with the surfaces of gold nanoparticles from citrate-reduction was first investigated in this work, following a literature-known method. The interaction strength (15 $k_B T$ at 21 °C) turned out to be similar to the case of phenyldithioesters already described in literature and its magnitude was found to be sufficient to affect efficient adsorption of RAFT polymers on gold nanoparticle surfaces. These new insights highlight and underline the possibility of using RAFT polymers directly to form nanohybrids with gold nanoparticles in 'grafting-to' approaches.

Chapters 3 and 4 revealed that controlling the distribution of the trithiocarbonate groups within the macromolecules produced can provide a rationale for the production of tailored nanohybrid polymer/gold structures. The two systems described in these chapters demonstrate that hierarchically ordered nanostructures with feature sizes of a few nanometers can be created and that their internal structure can be manipulated in a directed manner. Control over the produced nanostructures can be achieved by using the enabling 'tool' of RAFT polymerization, permitting exquisite control over the macromolecular architecture of the polymers prepared, which play the key role in these hybrid nanostructures: Specifically, if these polymers are employed as macromolecular particle linker, the adjustment of their degree of polymerization can be used to achieve defined particle spacings. Since the RAFT process permits the formation of polymeric material with a small dispersion with respect to the degree of polymerization, well-defined macromolecular particle linker can be obtained, and, therefore, particle spacings can be tightly controlled.

Two principally different strategies can be used to achieve a defined nanoparticle arrangement: The self-assembly of distinct building units can be exploited (Chapter 3) or nanostructures can be formed stepwise via isolation and purification of intermediates (Chapter 4). While the former approach is very straightforward to implement, it involves some limitations concerning the achievable complexity of the internal order of the self-assembled structures, if the constituent building blocks are not specially designed. Without such sophisticated building block design, defined higher-order assemblies are accessible via the latter approach. If the respective synthetic approach is realized in the form of a modular preparative route as within this work, it offers a convenient way to achieve a variety of combinations of distinct building units in one single nanostructure. For example, highly functionalized planet–satellite nanostructures had been prepared in this work, which include gold nanoparticles of different sizes interconnected by thermoresponsive poly(*N*-isopropylacryamide) and where the overall structure is functionalized with a second polymer containing benzylchloride moieties in the side-chains (Section 4.3.3).

In Section 4.3.1, it was furthermore also demonstrated that the observation of the formation of certain nanostructures can be used to draw conclusions about the structure of the precursors: The formation of planet–satellite nanostructures from planet-particle-core–star-polymer-shell particles was—complimented by control experiments—recognized as a prove that the surface-bound star polymers provide free, not surface-confined branch termini, which can capture and bind the satellite particles. This shows the possibility of verifying structural features of nanostructures by analyzing the

chemical behavior toward certain components, if direct evidence for such features is hard to achieve by analytical techniques.

5.2 Future Perspectives

The superparticle system described in Chapter 3 can be regarded as a structure which provides a confined environment. In principle, the potential to create precisely defined confined environments[260] could lead to theranostic agents, or artificial enzymes. Therefore, it seems worthwhile to continue the work on these systems. Particularly, future studies may concentrate on developing possibilities to achieve higher yields of self-assembled superstructures, for example by employing star-shaped rather than linear multifunctional cross-linking species. It has also been shown that the assembly of nanohybrid core–shell particles into superstructures can be triggered by an external stimulus.[181] The possibility of controlling the dynamics of superstructure assembly/disassembly may potentially be useful for the realization nanocontainers as delivery vehicles, and controlled release.

It should be noticed that Wentao Peng already continued studying the planet–satellite structures described in Chapter 4, by further exploring the scope of the presented nanodesign strategy. He realized a planet–satellite system, in which central AuNP planet particles are surrounded by satellite AgNPs (Figure 5.1).[259] This finding illustrates the general possibility of combining several distinct building units, also of different chemical nature, into one nanostructure. One may also think about using gold nanorods or nanowires as core material to test the possibility of aligning spherical satellite particles around this one-dimensional template. This approach should, if practicable, further strengthen the concept of hierarchically ordered multicomponent architectures made to order by RAFT star polymers. Generally speaking, the possibility of combining several building units in one well-defined nanostructure may enable materials scientists to build differently shaped nanostructures and to implement several functionalities and/or multiple levels of stimuli-responsiveness for the construction of smart materials. Therefore, further exploration of the scope of this nanodesign strategy can be considered very promising, as it offers tempting opportunities for achieving useful combinations of nanomaterial properties in a single nanoarchitecture.

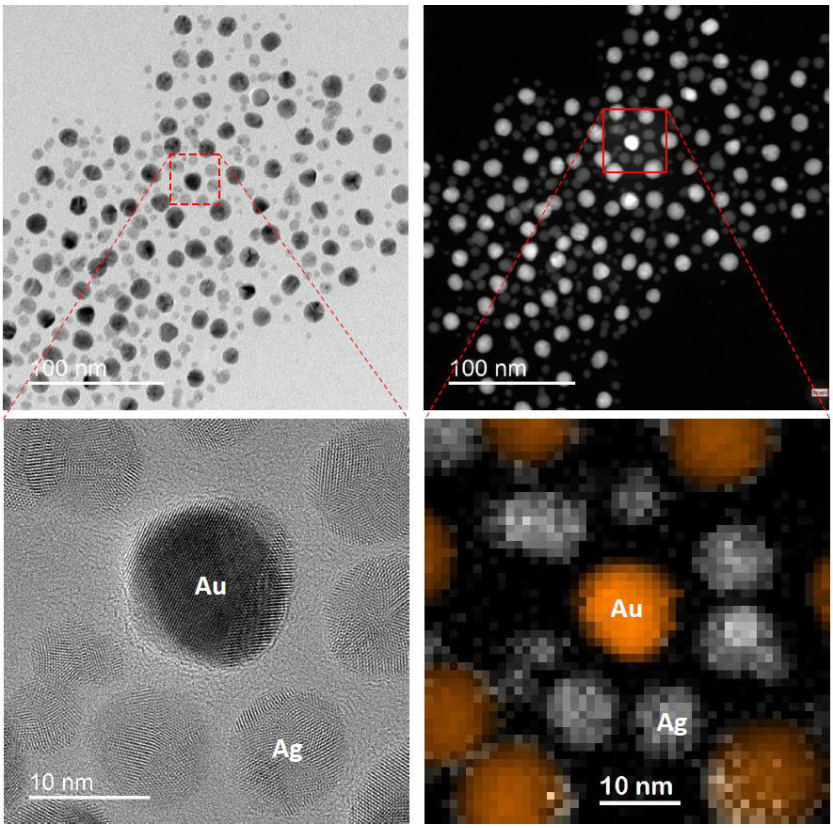

Figure 5.1 Overview bright-field (upper left) and dark-field (upper-right) image. The images on the bottom show magnified details in a high-resolution bright-field image (left) and in an elemental map obtained via HAADF (right) for a specimen of gold-planet–silver-satellite nanostructures.

To be more specific about plausible future investigations that exploit the possibility of combining different building units as suggested in the above paragraph, it may be expected that research in biomedicine could benefit from the ability to generate defined nanopatterned surfaces which can form the central part in biophysical investigations: Using defined two-dimensional arrays of gold nanoparticles (see Section 4.3.1) to present ligands for interactions with cell membranes is an established principle.[261] With the central element of nanostructured surfaces, cell properties like receptor-density-dependent adhesion and cell polarization can be obtained, which may guide to optimum therapeutic ranges of novel pharmaceuticals.[262,263] The cited systems, however, employ surfaces with controlled particle density of one type of particle which is translated to

surface-densities of one receptor-molecule. Being able to pattern surfaces in which two types of particles are presented in a strictly alternating fashion would enable to encode receptor densities for two different receptors, i.e. going from a one-dimensional to a two-dimensional parameter space. It may be, therefore, envisaged to use the novel planet–satellite system to form well-defined surfaces for the attachment of two different receptors. For that purpose, star polymers of poly(ethylene glycol) acrylate monomer should be used to avoid nonspecific protein adhesion, as would be expected in the case of polymers of the acrylamide type. Two types of nanoparticles (the planet and satellite particles) could then be functionalized with different cyclic peptides (comprising special anchor moieties) for specific recognition of proteins, as described in literature.[262,263] For achieving orthogonal functionalization of the planet and satellite particles, it may be convenient to combine metal oxide nanoparticles with noble metal particles, which can be surface-modified by using orthogonal anchor moieties (such as, for example, silanyl- and trithiocarbonate groups, respectively.)

The method of STEM-SI has been shown within this thesis to be extremely useful for obtaining detailed structural information about the polymer canopy in hybrid polymer/inorganic nanostructures. As such, this method can be anticipated to provide direct insight also into the structure of more complex polymer arrangements on solid surfaces (such as mixed brushes and their phase separation on nanoparticle surfaces and copolymers). The author intends to explore the applicability of STEM-SI toward the analysis of these mentioned structures in his post-doctoral work.

Chapter 6

Experimental

6.1 Chemicals

Acryloyl chloride (ABCR), Ambersep® OH (Fluka), 2-bromopropionyl bromide (Aldrich), carbon disulfide (Aldrich), 4-(chloromethyl)benzyl alcohol (Aldrich), *N*,*N*-dimethylacetamide (Aldrich), dimethyl-2,6-dibromoheptanedioate (mixture of diastereomers, Aldrich) lithium bromide (Aldrich), pentaerythritol (Aldrich), *n*-propanethiol (Aldrich), octadecylamine (Aldrich), sodium borohydride (Aldrich), sodium citrate tribasic dihydrate (Aldrich), tetra-*N*-octylammonium bromide (ABCR), and triethylamine (Aldrich) were purchased at the highest purity available and used as received. Ethylene glycol (Merck, p.a.), glycerol (Fluka, 86–88 %), hexanethiol (Aldrich, 95 %), hydrogen tetrachloroaurate trihydrate (ABCR, 99.9 %), magnesium sulfate (Grüssing, 99 %), and pyridine (Grüssing, 99.5 %) were used as received.

N,*N*-Dimethylacrylamide (Aldrich), and styrene (Aldrich) were passed through a short column of activated basic alumina prior to use.

AIBN (Akzo Nobel) was recrystallized from diisopropyl ether, ACCN (Akzo Nobel) was recrystallized from methanol, dipentaerythritol (technical grade, Aldrich) was recrystallized from water, *N*-Isopropylacrylamide (Aldrich) was recrystallized from toluene/hexane (3:1), and these substances were then stored at 4 °C prior to use.

Acetone, chloroform, dichloromethane, dimethylformamide, isopropanol, methanol, and toluene (p.a. grade, Fisher) were used as received. Anhydrous dichlormethane (Aldrich) was used as received.

Nanopure (type I) water was obtained using a Millipore filtration system equipped with a UV lamp (electric resistivity was over 18.2 MΩ·cm) and filtered through a 0.05 μm cellulose filter before use.

6.2 Analytical Methods

Atomic Force Microscopy (AFM).

The AFM measurements were performed using a Multimode 8 microscope under air. A Scan Asyst Air HR cantilever with a resonant frequency of $f = 130$ kHz and a force constant of $k = 0.4$ Nm^{-1} was used. Image artifacts were corrected and removed using Gwyddion software (Departement of Nanometrology, Czech Metrology Institute). Samples were applied on plasma-cleaned glass slides and one drop of the respective colloidal dispersion was given onto them with a glass pipet.

Dynamic Light Scattering (DLS).

DLS measurements were performed with a Malvern Zetasizer Nano S instrument equipped with a He-Ne laser ($\lambda = 633$ nm). Dilute (in every case below 0.1 % wt) analyte solutions were transferred into 10 mm quartz cuvettes and left to stand overnight prior to the measurements to assure sedimentation of remaining nondispersed impurities. Scattered intensity was detected at an angle of 173°.

Mass Spectrometry (MS).

Mass spectrometry was conducted in part on a Bruker Daltonik micrOTOF ESI–time-of-flight–mass-spectrometer and in part on a Bruker Daltonik maXis ESI–time of flight–mass-spectrometer. In all cases, the spectra were obtained in positive ion mode applying a spray voltage of 4.5 kV and a capillary temperature of 180 °C.

Nuclear Magnetic Resonance (NMR) Spectroscopy.

Most NMR spectra were acquired on a Bruker Advance III 300 (^{1}H NMR and ^{13}C NMR). In the case of RAFT agent **S^{4}** and its tetrabromide precursor, spectra were acquired on a Bruker Advance 400 (^{1}H NMR) and Varian Inova 500 (^{13}C NMR). Samples were dissolved in deuterated chloroform or deuterated dichloromethane. The spectra were referenced to the residual signal of the deuterated solvent.

Scanning Transmission Electron Microscopy and Spectrum Imaging (STEM-SI).

These experiments were performed by Dr. Vladimir Roddatis (Göttingen) and Dr. Sergei Lopatin (Thuwal).
Scanning transmission electron microscopy and spectrum imaging (STEM-SI) studies were performed using a FEI Titan 80-300 Environmental TEM equipped with an electron monochromator and a Gatan Imaging Filter (GIF)

Quantum 965ER. The microscope was operated at 80 kV in order to minimize electron beam induced damages of polymers and to increase EELS signal/noise ratio. Samples for electron microscopy studies were dropped onto a PELCO® Graphene TEM Support Films supported by a lacey carbon film on a 300 mesh copper grid. EELS maps were acquired in STEM mode. To extract elemental maps from the spectrum image (SI) a correlation method was exploited. In this method the actual shape of a core-loss edge for a given element is correlated with spectra for entire SI. An image built in such a way is essentially a map of correlation coefficients. This allows to avoid artifacts of standard extraction methods, when signal and background from heavy (big Z) particles gives a rise of counts in the elemental map regardless of element presence in the specimen.

Size-exclusion chromatography (SEC) with DMAc.

Polymer samples of PN^{i}PAAM and PDMAAM were analyzed on a DMAc SEC setup. SEC characterization was performed on an Agilent 1260 Infinity system with an isocratic solvent pump, a PSS GRAM (polyester copolymer network) precolumn (8 × 50 mm), and three PSS GRAM separation columns (8 × 300 mm, nominal particle size = 10 µm; pore sizes = 30, 10^3, and 10^3 Å) using DMAc (containing 0.1 % of LiBr) as the eluent with a flow rate of $8 \cdot 10^{-4}$ L min^{-1}. The system was calibrated using linear PSS poly(methyl methacrylate) standards (M_p = 0.8–1820 kg mol^{-1}) with narrow size distribution. The system was equipped with a refractive index detector and UV detector. Analyte samples were dissolved in DMAc containing toluene as flow rate marker and filtered through 0.45 µm polytetrafluoroethylene (PTFE) filters.

Size-exclusion chromatography (SEC) with THF.

Polymer samples of PS and PVC were analyzed on a THF SEC setup. SEC characterization was performed using an Agilent 1260 infinity system. It was composed of an autosampler, an isocratic solvent pump, a PSS SDV (styrene-divinylbenzene copolymer network) precolumn (8 × 50 mm, nominal particle size: 5 µm), three PSS SDV separation columns (8 × 300 mm, nominal particle size: 5 µm, pore sizes: 10^6 Å, 10^5 Å, and 10^3 Å) maintained at 35 °C in a column compartment, a UV detector, and a refractive index detector. The flow rate of the mobile phase was 1.0 mL min^{-1}. The whole setup was calibrated with PSS polystyrene standards of low dispersity with toluene as internal standard. All samples were filtered through a 0.45 µm PTFE syringe filter prior to injection.

Small-Angle X-Ray Scattering (SAXS).

The SAXS measurements presented in Chapter 3 were performed in the lab of

Professor Sarah Köster in Göttingen. Experimental details are outlined below:
The measurements were conducted employing a Hecus S3-MICROpix camera system, SWAXS version (Hecus X-ray Systems, Graz, Austria) equipped with an iMOXS X-ray source (IfG, Berlin, Germany). A primary X-ray beam (λ = 1.54 Å, Cu K_α radiation) was applied to the samples with a flux of approx. $5 \cdot 10^{13}$ ph s^{-1} m^{-2} at 50 kV and 600 µA. The X-ray beam had a size of approx. 1.1×1.5 mm^2. Before reaching the detector, the primary beam was blocked with a 2 mm tungsten filter. The sample-to-detector distance was 27.5 cm. Scattered X-rays were detected by a Pilatus 100K single photon counting pixel detector (487×195 pixels, pixel size 172×172 μm^2, Dectris, Baden, Switzerland). Five measurements for 180 s of exposure time each were made for every colloidal sample.

The SAXS measurements presented in Chapter 4 were performed in the lab of Professor Otto Glatter in Graz. Experimental details are outlined below:
SAXS measurements were conducted employing a SAXSess camera (Anton Paar, Graz, Austria) and sealed tube X-ray generator (DebyeFlex3000) operating at 40 kV and 50 mA. The divergent polychromatic X-rays were focused into a line-shaped X-ray beam (λ = 1.54 Å, Cu K_α radiation) using a Goebel mirror. Scattering profiles were recorded with a CCD camera (2084×2084 pixels, pixel size $24\ \mu m \times 24\ \mu m$, PI-SCX, Roper Scientific, Germany). For every sample, measurements were performed in methanol dispersion four times for 10 minutes at 25 °C and averaged.

In all cases, the scattering patterns were edited by subtracting solvent background and integrated into one-dimensional scattering functions. Absolute intensities were determined from measurements of water as a standard[264] (ultrapure type I water, electric resistivity 18.2 MΩ·cm at 25 °C). Scattering intensity curves were plotted as a function of the scattering vector defined as

$$q = \frac{4\pi \cdot \sin\vartheta}{\lambda},$$

where 2ϑ is the scattering angle.

Thermogravimetric Analysis (TGA).

TGA experiments were conducted on a Netzsch TG 209 F3 Tarsus in a temperature range from 25 °C–1000 °C with a heating rate of 10 K min^{-1} under an air flow of 20 mL min^{-1}. Grafting densities σ in macromolecules per nm^{-2} were calculated as such:

$$\sigma = \frac{M_{\mathrm{Au}} \cdot N}{M_{\mathrm{n}} \cdot A_{\mathrm{AuNP}}} \cdot \left(\frac{1}{x} - 1\right),$$

where x is the weight retention at 600 °C, N the average number of gold atoms per AuNP, and A_{AuNP} the AuNP surface, taking the surface distribution into account. Several batches of citrate-capped AuNPs were combined to provide a sufficient amount of material and to assure equal particle size and size distribution within all samples investigated in TGA.

Transmission Electron Microscopy (TEM).

TEM measurements were conducted on a Philips CM 12 transmission electron microscope applying an acceleration voltage of 120 kV. A 50 µm aperture was used in the condenser lens and scattered electrons were blocked with a 20 µm aperture in the focal plane of the objective lens. The instrument was equipped with an Olympus 1376 × 1032 pixel CCD-camera. All samples were applied on Plano 200 mesh copper TEM grids holding a 10–15 nm amorphous carbon film by drop-casting. The TEM grids were placed on a laboratory paper tissue, and one drop of the respective colloidal dispersion was given onto them with a glass pipet. The TEM grid was immediately covered with a small glass vial until all solvent had evaporated.
Particle size distributions had been determined from TE micrographs using the Particle Size Analyzer Macro (Institut Català de Nanotecnologia, Spain) for ImageJ software.[265]

UV/visible Extinction Spectroscopy.

UV/visible spectroscopy was conducted with a Cary 300 Scan photospectrometer using Hellma quartz cuvettes (optical path length 10 mm). The spectra were recorded in a wavelength range between 250 and 900 nm with a scan rate of 150 nm min^{-1}. Baseline correction was performed by subtracting the spectrum of the pure dispersant.

X-ray crystallography.

Single crystal structure analysis was performed by Peter Stollberg and Alexander Paesch.

Suitable crystals for single crystal X-ray diffraction analysis were selected under argon atmosphere and transferred in perfluorated oil on a microscope slide.[266–268] An appropriate crystal was selected using a polarizer microscope, mounted to the tip of a MiTeGen©MicroMount, fixed to a goniometer head and shock cooled by the crystal cooling device.

The data was collected from shock-cooled crystals at 100(2) K on a BRUKER D8 three circle diffractometer equipped with either an INCOATEC Mo or Ag Microsource with mirror optics (λ = 71.073 pm, Mo K_α; λ = 56.086 pm, Ag K_α)

and SMART APEX II detector. The data was integrated with SAINT (v8.30C in BRUKER APEX II, BRUKER AXS Inst. Inc., Madison, USA) and an empirical absorption correction (SADABS)[269,270] was applied. The structures were solved by direct methods (SHELXT)[271,272] and refined by full-matrix least-squares methods against F^2 (SHELXL).[271,272] All non-hydrogen-atoms were refined with anisotropic displacement parameters. The hydrogen atoms were refined isotropically on calculated positions using a riding model with their U_{iso} values constrained to equal to 1.5 times the U_{eq} of their pivot atoms for terminal sp^3 carbon atoms and 1.2 times for all other carbon atoms. Disordered moieties were refined using bond length restraints and isotropic displacement parameter restraints.

6.3 Syntheses

6.3.1 Synthesis of RAFT agents

The syntheses for RAFT agents **2**,[164] $\mathbf{L^1}$,[191,192] and $\mathbf{L^m}$[124] had been performed according to respective literature protocols. RAFT agents $\mathbf{L^2}$, $\mathbf{S^3}$, $\mathbf{S^4}$, and $\mathbf{S^6}$ had been prepared following in principle a literature-known[273] route. The synthesis of RAFT agent **1** follows a similar strategy. The details of their preparation are described in the following.

Synthesis of dibenzyl trithiocarbonate.

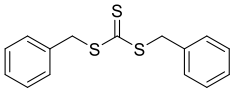

Benzyl mercaptan (5.000 g, 40.26 mmol) was dissolved in chloroform (125 mL). Triethylamine (5.155 g, 50.94 mmol) was added and the resulting mixture was stirred for 1 hour at room temperature. Carbon disulfide (25 mL) was added and the reaction mixture was stirred for further 5 minutes. Benzyl bromide (9.775 g, 57.15 mmol) was added and the reaction mixture was stirred overnight. All volatiles were removed in vacuo and the residue was taken up in diethyl ether (200 mL). The organic phase was washed with hydrochloric acid (1 M, 100 mL) and water (3 × 100 mL). The organic phase was dried over magnesium sulfate and all volatiles were removed under reduced pressure. The crude product was passed through a short column of silica, using pentane as the mobile phase and further purified by crystallization from ethanol at 4 °C, to obtain yellow needles.

MS (ESI) *m/z*: found: 313.0133 $[M+Na]^+$, calcd.: 313.0150.

^{1}H NMR (CD_2Cl_2, 300.132 MHz): δ (ppm) = 7.39–7.26 (m, 10 H), 4.64 (s, 4 H).

^{13}C NMR (CD_2Cl_2, 75.477 MHz): δ (ppm) = 223.38, 135.72, 129.80, 129.23, 128.31, 42.02.

Synthesis of RAFT agent 1.

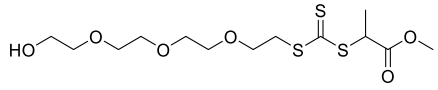

2-(2-(2-(2-Mercaptoethoxy)ethoxy)ethoxy)ethanol (0.200 g, 0.951 mmol) was dissolved in dichloromethane (25 mL). Triethylamine (0.102 g, 1.008 mmol) was added and the resulting solution was stirred for 1 hour. Carbon disulfide (1.0 mL) was then added slowly and the solution turned yellow. After additional 5 minutes, methyl 2-bromopropionate (0.168 g, 1.008 mmol) was added and the reaction mixture was stirred overnight. All volatiles were removed *in vacuo* and the crude product was purified *via* column chromatography on silica using dichloromethane as the mobile phase. The product was obtained as a yellow liquid (0.273 g, 0.733 mmol, 77 %).

^{1}H NMR ($CDCl_3$, 300.132 MHz): δ (ppm) = 4.81 (q, ^3J = 7.4 Hz, 1 H), 3.74–3.57 (m, 19 H), 2.50 (br, 1 H), 1.59 (d, ^3J = 7.4 Hz, 1 H).

^{13}C NMR ($CDCl_3$, 75.477 MHz): δ (ppm) = 221.87, 171.61, 72.60, 70.81, 70.59, 70.48, 68.55, 61.88, 53.00, 48.08, 36.66, 17.04.

Preparation of RAFT agent L^2.

Synthesis of the dibromide precursor to RAFT agent $\mathbf{L^2}$:

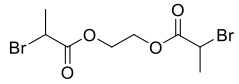

Ethylene glycol (1.24 g, 20.00 mmol) and triethylamine (4.20 g, 41.5 mmol) were dissolved in 50 mL anhydrous dichloromethane. The solution was cooled to 0 °C and a solution of 2-bromopropionyl bromide (13.2 g, 61.1 mmol) in 50 mL anhydrous dichloromethane was added under stirring over a period of 30 minutes. The reaction mixture was allowed to warm to room temperature and stirred overnight. The solvent was evaporated and the residue was dissolved

in diethyl ether. The ethereal solution was washed successively with hydrochloric acid (1 M), brine, and water. The organic layer was concentrated and the product purified *via* column chromatography on silica (hexane/ethyl acetate 20:1 then gradient to 10:1) to yield a colorless liquid (5.00 g, 15.1 mmol, 76%).

MS (ESI) *m*/*z*: found: 330.9171 $[M+H]^+$, calcd.: 330.9175.

^{1}H NMR ($CDCl_3$, 300.132 MHz): δ (ppm) = 5.41–4.35 (m, 6 H), 1.83 (d, ^3J = 6.9 Hz, 6 H).

^{13}C NMR ($CDCl_3$, 75.477 MHz): δ (ppm) = 169.99, 63.22, 39.76, 21.78.

Synthesis of RAFT agent **L^2**:

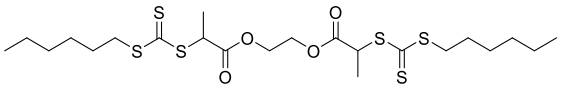

Hexanethiol (3.56 g, 30.1 mmol) was dissolved in chloroform (100 mL). Triehtylamine (3.66 g, 36.2 mmol) was added and the resulting mixture was stirred for 1 hour. Carbon disulfide (15 mL) was then added and the reaction mixture was stirred for 15 minutes before adding the dibromide (5.00 g, 15.1 mmol). The reaction mixture was stirred overnight. The solvent was evaporated and the residue was dissolved in diethyl ether (200 mL). The ethereal solution was extracted with hydrochloric acid (10%, 100 mL) and water (3 × 100 mL). The organic layer was concentrated and the product purified *via* column chromatography on silica (hexane/ethyl acetate 10:1) to afford the difunctional RAFT agent as a yellow liquid (6.98 g, 12.5 mmol, 83%).

MS (ESI) *m*/*z*: found: 559.1168 $[M+H]^+$, calcd.: 559.1167.

^{1}H NMR ($CDCl_3$, 300.132 MHz): δ (ppm) = 4.83 (q, ^3J = 7.4 Hz, 2 H), 4.35 (s, 4 H), 3.40–3.31 (m, 4 H), 1.72–1.59 (m, 10 H), 1.40-1.28 (m, 12 H), 0.89 (t, ^3J = 7.4 Hz, 6 H).

^{13}C NMR ($CDCl_3$, 75.477 MHz): δ (ppm) = 221.87, 170.98, 63.13, 47.80, 37.40, 31.35, 28.68, 27.94, 22.56, 16.85, 14.08.

Preparation of RAFT agent S^3.

Synthesis of the tribromide precursor to RAFT agent **S^3**:

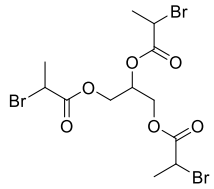

To a mixture of glycerol (3.00 g, 32.6 mmol) and pyridine (7.9 mL) in chloroform (200 mL) was added bromopropionylbromide (24.6 g, 114 mmol) and the resulting mixture was stirred for 72 hours at room temperature. The solution was then washed successively with hydrochloric acid (1 M, 3 × 200 mL), saturated $NaHCO_3$ solution (3 × 200 mL) and water (3 × 200 mL). The organic phase was dried over magnesium sulfate and the solvent removed under reduced pressure. The crude product was purified by column chromatography on silica using hexane/ethyl acetate (10:1) as the mobile phase to yield the product as a mixture of diastereomers in form of a colorless liquid (6.16 g, 12.4 mmol, 38.0 %).

^{1}H NMR ($CDCl_3$, 300.132 MHz): δ (ppm) = 5.41–5.33 (m, 1 H), 4.55–4.26 (m, 7 H), 1.84–1.81 (m, 9 H).

^{13}C NMR ($CDCl_3$, 75.477 MHz): δ (ppm) = 169.85, 169.82, 169.80, 169.56, 169.50, 169.45, 70.32, 70.25, 70.18, 63.10, 63.07, 63.04, 62.94, 39.57, 39.55, 39.44, 39.39, 21.64, 21.61, 21.58.

Synthesis of RAFT agent **S^3**:

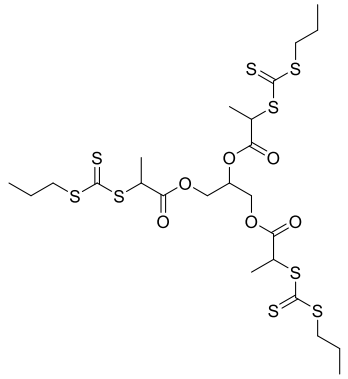

Propanethiol (1.609 g, 21.13 mmol) was dissolved in anhydrous dichloromethane (200 mL). Triethylamine (2.138 g, 21.13 mmol) was added and the mixture was stirred for 1 hour at room temperature. Carbon disulfide (10 mL) was then added and the mixture was stirred for further 15 minutes at room temperature before addition of the tribromide (3.000 g, 6.037 mmol). The resulting mixture was stirred for 72 hours at room temperature. The solution was then washed successively with saturated $NaHCO_3$ solution (3 × 200 mL), hydrochloric acid (10 %, 3 × 200 mL) and water (3 × 200 mL). The organic phase was dried over magnesium sulfate and the solvent removed under reduced pressure. The crude product was purified by column chromatography on silica using hexane/ethyl acetate (10:1) as the mobile phase to yield the product as a mixture of diastereomers in form of a viscuos yellow oil (3.727 g, 5.241 mmol, 86.8 %).

MS (ESI) *m*/*z*: found: 733.0028 $[M+Na]^+$, calcd.: 733.0047.

^{1}H NMR ($CDCl_3$, 300.132 MHz): δ (ppm) = 5.30–5.23 (m, 1 H), 4.88–4.77 (m, 3 H), 4.44–4.14 (m, 4 H), 3.34 (t, ^3J = 7.3 Hz, 6 H), 1.74 (h, ^3J = 7.4 Hz, 6 H), 1.60 (d, ^3J = 7.4 Hz, 9 H), 1.02 (t, ^3J = 7.4 Hz, 9 H).

^{13}C NMR ($CDCl_3$, 75.477 MHz): δ (ppm) = 221.88, 221.86, 170.79, 170.77, 170.74, 170.42, 70.23, 70.17, 70.12, 63.12, 63.08, 47.90, 47.62, 47.62, 47.59, 21.60, 16.76, 16.74, 16.69, 13.62.

Preparation of RAFT agent S^4.

Synthesis of the tetrabromide precursor to RAFT agent **S^4**:

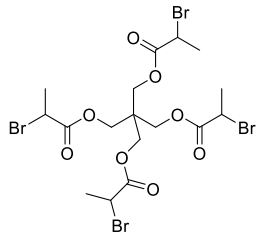

To a mixture of recrystallized pentaerythritol (3.75 g, 27.5 mmol) and pyridine (6.9 mL) in chloroform (75 mL) was added bromopropionylbromide (27.58 g, 127.8 mmol) and the resulting mixture was stirred for 72 hours at room temperature. The solution was then washed successively with water (50 mL), saturated $NaHCO_3$ solution (50 mL) and brine (50 mL). The organic phase was dried over magnesium sulfate and the solvent removed under reduced pressure. The crude product was purified by crystallization from diethylether/ethanol to obtain colorless crystals (14.62 g, 21.63 mmol, 79 %).

^{1}H NMR ($CDCl_3$, 400.130 MHz): δ (ppm) = 4.41–4.35 (m, 6 H), 1.83 (d, ^{3}J = 6.9 Hz, 6 H).

^{13}C NMR ($CDCl_3$, 125.707 MHz): δ (ppm) = 169.99, 63.22, 39.76, 21.78.

Synthesis of RAFT agent **S^{4}**:

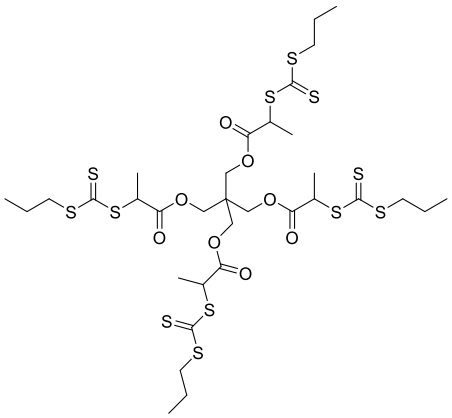

Propanethiol (3.656 g, 48.00 mmol) was dissolved in anhydrous dichloromethane (250 mL). Triethylamine (4.857 g, 48.00 mmol) was added and the mixture was stirred for 1 hour at room temperature. Carbon disulfide (20 mL) was then added and the mixture was stirred for further 15 minutes at room temperature before addition of the tetrabromide (7.000 g, 10.34 mmol). The resulting mixture was stirred for 24 hours at room temperature. The solution was then washed successively with saturated $NaHCO_3$ solution (3 × 200 mL), hydrochloric acid (10 %, 3 × 200 mL) and water (3 × 200 mL). The organic phase was dried over magnesium sulfate and the solvent removed under reduced pressure. The crude product was purified by column chromatography on silica using hexane/diethylether (4:1) as the mobile phase to yield the product as a mixture of diastereomers in form of a viscos yellow oil (7.562 g, 7.865 mmol, 76 %).

MS (ESI) *m*/*z*: found: 961.0380 [*M*+H]$^{+}$, calcd.: 961.0383.

^{1}H NMR ($CDCl_3$, 400.130 MHz): δ (ppm) = 4.82 (q, ^{3}J = 7.4 Hz, 4 H), 4.11–4.01 (m, 8 H), 3.39–3.28 (m, 8 H), 1.73 (h, ^{3}J = 7.4 Hz, 8 H), 1.58 (d, ^{3}J = 7.4 Hz, 12 H), 1.02 (t, ^{3}J = 7.4 Hz, 12 H).

^{13}C NMR ($CDCl_3$, 125.707 MHz): δ (ppm) = 221.73, 170.43, 62.99, 47.44, 42.41, 39.42, 21.64, 16.59, 13.74.

Preparation of RAFT agent S[6].

Synthesis of the hexabromide precursor to RAFT agent **S[6]**:

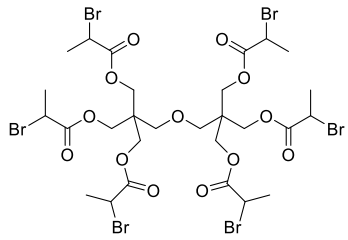

To a mixture of recrystallized dipentaerythritol (7.40 g, 29.1 mmol) and pyridine (14.1 mL) in chloroform (250 mL) was added bromopropionylbromide (40.8 g, 189 mmol) and the resulting mixture was stirred for 72 hours at room temperature. The solution was then washed successively with hydrochloric acid (1 M, 3 × 200 mL), saturated $NaHCO_3$ solution (3 × 200 mL) and water (3 × 200 mL). The organic phase was dried over magnesium sulfate and the solvent removed under reduced pressure. The crude product was purified by twofold crystallization from acetone/ethanol to obtain colorless crystals (18.2 g, 17.1 mmol, 59 %).

^{1}H NMR ($CDCl_3$, 300.132 MHz): δ (ppm) = 4.40 (q, ^3J = 6.9 Hz, 6 H), 4.35–4.14 (m, 12 H), 3.51 (s, 4 H), 1.83 (d, ^3J = 6.9 Hz, 18 H).

^{13}C NMR ($CDCl_3$, 75.477 MHz): δ (ppm) = 169.65, 69.11, 63.34, 44.09, 39.79, 21.63.

Synthesis of RAFT agent **S[6]**:

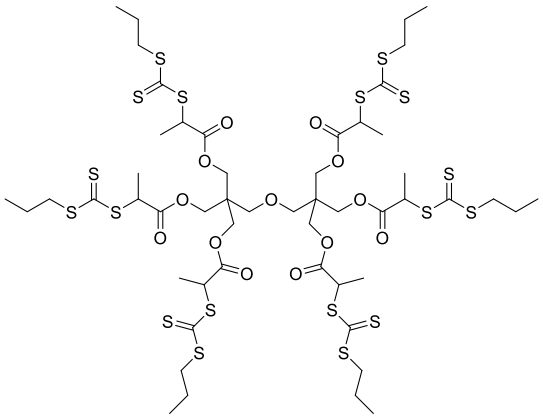

Propanethiol (2.505 g, 32.89 mmol) was dissolved in anhydrous dichloromethane (150 mL). Triethylamine (3.329 g, 32.90 mmol) was added and the mixture was stirred for 1 hour at room temperature. Carbon disulfide (15 mL) was then added and the mixture was stirred for further 15 minutes at room temperature before addition of the hexabromide (5.000 g, 4.699 mmol). The resulting mixture was stirred for 120 hours at room temperature. The solution was then washed successively with saturated $NaHCO_3$ solution (3 × 200 mL), hydrochloric acid (10 %, 3 × 200 mL) and water (3 × 200 mL). The organic phase was dried over magnesium sulfate and the solvent removed under reduced pressure. The crude product was purified by column chromatography on silica using hexane/ethyl acetate (10:1) as the mobile phase to yield the product as a mixture of diastereomers in form of a viscos yellow oil (5.421 g, 3.638 mmol, 77 %).

MS (ESI) *m*/*z*: found: 1491.0797 $[M+H]^+$, calcd.: 1491.0801.

^{1}H NMR ($CDCl_3$, 300.132 MHz): δ (ppm) = 4.86 (q, ^3J = 7.4 Hz, 6 H), 4.11–4.00 (m, 12 H), 3.42–3.27 (m, 16 H), 1.74 (h, ^3J = 7.3 Hz, 12 H), 1.59 (d, ^3J = 7.4 Hz, 18 H), 1.02 (t, ^3J = 7.4 Hz, 18 H).

^{13}C NMR ($CDCl_3$, 75.477 MHz): δ (ppm) = 221.94, 170.56, 69.09, 63.32, 47.50, 43.34, 39.34, 21.61, 16.66, 13.66.

6.3.2 Synthesis of 4-(chloromethyl)benzyl acrylate

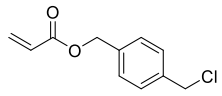

A solution of 4-(chloromethyl)benzyl alcohol (0.500 g, 3.19 mmol) in anhydrous dichloromethane (100 mL) was mixed with triethylamine (0.388 g, 3.83 mmol) and then cooled to 0 °C. Acryloyl chloride (0.347 g, 3.83 mmol) was then added over a period of 30 minutes and the reaction mixture was stirred overnight. The organic phase was successively washed with saturated $NaHCO_3$ solution (100 mL), water (100 mL), hydrochloric acid (1 M, 100 mL) and water (2 × 100 mL). The crude product was purified by column chromatography on silica using dichloromethane as the mobile phase to obtain the product as a colorless liquid (0.463 g, 2.20 mmol, 69 %).

MS (ESI) *m*/*z*: found: 233.0340 $[M+Na]^+$, calcd.: 233.0340.

^{1}H NMR (CD_2Cl_2, 300.132 MHz): δ (ppm) = 7.43–7.37 (m, 4 H), 6.43 (dd, ^3J = 17.3 Hz, ^2J = 1.5 Hz, 1 H), 6.17 (dd, ^3J = 17.3 Hz, 10.4 Hz, 1 H), 5.86 (dd, ^3J = 10.4 Hz, 2J = 1.5 Hz, 1 H), 5.19 (s, 2 H), 4.61 (s, 2 H).

^{13}C NMR (CD_2Cl_2, 75.477 MHz): δ (ppm) = 166.29, 138.21, 137.04, 131.44, 129.35, 128.99, 128.82, 66.26, 46.53.

6.3.3 Synthesis of Gold(I) Complexes

Preparation of chloro(dibenzyl trithiocarbonato) gold(I).

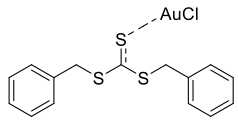

Hydrogen tetrachloroaurate(III) trihydrate (1.000 g, 2.539 mmol) was dissolved in a solvent mixture of ethanol (8.4 mL) and water (1.8 mL). Tetrahydrothiophene (483 µL) was then added to the mixture under stirring at room temperature and the reaction mixture was stirred for 30 minutes. A white precipitate formed which was filtered, washed with ethanol and vacuum dried to yield chloro(tetrahydrothiophene) gold(I) (779 mg, 2.430 mmol, 96 %), which was directly used in the next step.

Chloro(tetrahydrothiophene) gold(I) (779 mg, 2.430 mmol) was dissolved in acetone (100 mL). Dibenzyl trithiocarbonate (705.8 mg, 2.430 mmol) was then

added and the reaction mixture was stirred for 2 hours at room temperature. After that, the reaction mixture was cooled to 4 °C, to induce crystallization of the title compound from the mother liquor, which is obtained as yellow needles (768.4 mg, 1.470 mmol, 60 %).

^{1}H NMR (CD_2Cl_2, 300.132 MHz): δ (ppm) = 7.39–7.26 (m, 10 H), 4.64 (s, 4 H).
^{13}C NMR (CD_2Cl_2, 75.477 MHz): δ (ppm) = 223.36, 135.71, 129.79, 129.22, 128.31, 42.01.

Preparation of bis(dibenzyl trithiocarbonato) gold(I) hexafluoroantimonate.

A mixture of chloro(dibenzyl trithiocarbonato) gold(I) (266.3 mg, 0.509 mmol) in anhydrous dichloromethane (40 mL) was degassed with argon in the dark and cooled to 0 °C. Silver hexafluoroantimonate (175.0 mg, 0.509 mmol) dissolved in acetone (2 mL) was then added. The reaction mixture was stirred for 2 hours in the dark at 0 °C. The mixture was then centrifuged (1400 g, 5 minutes, 0 °C) and filtered. Hexane (3 mL) was added to the filtered solution, which was then cooled at −20 °C to induce crystallization of the title compound which is obtained as orange crystals together with amorphous precipitate.

6.3.4 Preparation of the Different RAFT Polymers

Unless otherwise stated, all polymerizations were conducted by placing the polymerization cocktail (containing monomer, solvent, RAFT agent, and AIBN as thermal initiator) into glass vials sealed with a rubber septum. The mixtures were then purged with argon to remove oxygen from the reaction mixture before they were heated to 60 °C in a thermostated heating block to initiate polymerization. After predetermined times, the polymerizations were stopped by cooling on ice and exposing the mixtures to air. The polymeric material was isolated by threefold precipitation (into methanol in the case of polystyrene and PVBC samples and into diethylether in the case of PN^{i}PAAM and PDMAAM samples.) Detailed polymerization conditions for the individual polymerizations together with reults from SEC analysis can be found in the following. The reported M_n values for the star polymer species are corrected values, considering an experimentally determined form factor which takes into account the polymer star topology.[237,238] In the case were monomer conversion, x, had been determined, theoretical molar masses were calculated as such:

$$M_n^{theo} = \frac{[Monomer]_0 \cdot x}{[RAFT]_0} \cdot M(Monomer) + M(RAFT). \quad (6.1)$$

In equation (6.1) the contribution from initiator-derived chains is neglected, which is however, a reasonable simplification under the polymerization conditions applied throughout this work.

Table 6.1 Polymerization conditions and characterization results for the PN^{i}PAAM sample derived from **L^{1}**.

Polymer	[DMF]/[N^{i}PAAM]$_0$/ [RAFT]$_0$/[AIBN]$_0$	t / min	M_n / (10^3 g mol^{-1})^a	$Đ^a$
L^{1}-49k	2400 : 800 : 1 : 0.5	120	49	1.18

[a]Apparent average molar masses and dispersity values measured by DMAc SEC (PMMA calibration, refractive index detection).

Table 6.2 Polymerization conditions and characterization results for the P(4-ClMeBnA) sample derived from **L^{1}**.

Polymer	[4-ClMeBnA]$_0$/ [RAFT]$_0$/[AIBN]$_0$[a]	t / min	M_n / (10^3 g mol^{-1})^b	$Đ^b$	M_n^{theo} / (10^3 g mol^{-1})^c
L^{1}-P(4-ClMeBnA)	150 : 1 : 0.1	270	18	1.19	27

[a]Polymerization was conducted in 38% wt DMF. [b]Apparent average molar masses and dispersity values measured by THF SEC (PS calibration, refractive index detection). [c]Calculated according to equation (6.1).

Table 6.3 Polymerization conditions and characterization results for the PDMAAM sample derived from **L^{1}**.

Polymer	[DMAAM]$_0$/ [RAFT]$_0$/[ACCN]$_0$[a]	t / min	M_n / (10^3 g mol^{-1})^b	$Đ^b$
L^{1}-PDMAAM	100 : 1 : 0.2	60	8	1.33

[a]Polymerization was conducted in 37% wt DMF at 100 °C. [b]Apparent average molar masses and dispersity values measured by DMAc SEC (PMMA calibration, refractive index detection).

Table 6.4 Polymerization conditions and characterization results for the PN^{i}PAAM samples derived from **L^{2}**.

Polymer	[DMF]/[N^{i}PAAM]$_0$/ [RAFT]$_0$/[AIBN]$_0$	t / min	M_n / (10^3 g mol^{-1})[a]	$Đ$[a]
L^{2}-19k	1000 : 250 : 1 : 0.1	150	19	1.12
L^{2}-24k	1000 : 250 : 1 : 0.1	240	24	1.13
L^{2}-33k	1800 : 400 : 1 : 0.1	240	33	1.13
L^{2}-36k	1800 : 400 : 1 : 0.1	300	36	1.15
L^{2}-40k	1800 : 400 : 1 : 0.1	420	40	1.16
L^{2}-53k	6000 : 1000 : 1 : 0.1	420	53	1.15

[a]Apparent average molar masses and dispersity values measured by DMAc SEC (PMMA calibration, refractive index detection).

Table 6.5 Polymerization conditions and characterization results for the PN^{i}PAAM samples derived from **S^{3}**.

Polymer	[DMF]/[N^{i}PAAM]$_0$/ [RAFT]$_0$/[AIBN]$_0$	t / min	M_n / (10^3 g mol^{-1})[a]	$Đ$[a]
S^{3}-23k	1000 : 250 : 1 : 0.1	240	23	1.13
S^{3}-32k	1800 : 400 : 1 : 0.1	255	32	1.11
S^{3}-36k	1800 : 400 : 1 : 0.1	290	36	1.10
S^{3}-41k	1800 : 400 : 1 : 0.1	420	41	1.11
S^{3}-59k	6000 : 1000 : 1 : 0.1	420	59	1.13
S^{3}-63k	6000 : 1000 : 1 : 0.1	540	63	1.17

[a]Apparent average molar masses and dispersity values measured by DMAc SEC (PMMA calibration, refractive index detection). The reported M_n values are corrected values, considering an experimentally determined form factor which takes into account the polymer star topology.

Table 6.6 Polymerization conditions and characterization results for the PN^{i}PAAM samples derived from **S^{4}**.

Polymer	[DMF]/[N^{i}PAAM]$_0$/ [RAFT]$_0$/[AIBN]$_0$	t / min	M_n / (10^3 g mol^{-1})[a]	$Đ$[a]
S^{4}-12k	300 : 100 : 1 : 0.1	360	12	1.20
S^{4}-22k	1600 : 400 : 1 : 0.4	90	22	1.10
S^{4}-27k	1600 : 400 : 1 : 0.4	120	27	1.11
S^{4}-34k	1600 : 400 : 1 : 0.4	180	34	1.11
S^{4}-40k	1600 : 400 : 1 : 0.4	240	40	1.08
S^{4}-42k	6000 : 1000 : 1 : 0.75	90	42	1.08
S^{4}-46k	6000 : 1000 : 1 : 0.75	105	46	1.09
S^{4}-52k	6000 : 1000 : 1 : 0.75	120	52	1.13
S^{4}-62k	6000 : 1000 : 1 : 0.75	180	62	1.15

[a]Apparent average molar masses and dispersity values measured by DMAc SEC (PMMA calibration, refractive index detection). The reported M_n values are corrected values, considering an experimentally determined form factor which takes into account the polymer star topology.

Table 6.7 Polymerization conditions and characterization results for the PN^{i}PAAM samples derived from **S^{6}**.

Polymer	[DMF]/[N^{i}PAAM]$_0$/ [RAFT]$_0$/[AIBN]$_0$	t / min	M_n / (10^3 g mol^{-1})[a]	$Đ$[a]
S^{6}-29k	1800 : 400 : 1 : 0.1	240	29	1.10
S^{6}-33k	1800 : 400 : 1 : 0.1	300	33	1.13
S^{6}-42k	1800 : 400 : 1 : 0.1	420	42	1.11
S^{6}-50k	3000 : 600 : 1 : 0.1	420	50	1.14
S^{6}-59k	6000 : 1000 : 1 : 0.1	420	59	1.14
S^{6}-69k	6000 : 1000 : 1 : 0.1	540	69	1.10

[a]Apparent average molar masses and dispersity values measured by DMAc SEC (PMMA calibration, refractive index detection). The reported M_n values are corrected values, considering an experimentally determined form factor which takes into account the polymer star topology.

6.3.5 Synthesis Gold Nanoparticles and Nanohybrid Structures

Synthesis of citrate-capped gold nanocrystals (~13 nm).

The synthetic procedure has already been described.[71] In a typical experiment, all glassware was cleaned with *aqua regia*, repeatedly washed with ultrapure water and oven-dried. To a boiling solution of hydrogen tetrachloroaurate (100 mL, 0.50 mM, 1.0 equiv.) was added a hot solution of sodium citrate (5 mL, 39 mM, 3.9 equiv.) under vigorous stirring. The mixture was refluxed for 10 minutes and then cooled to room temperature. The colloidal suspension was stored in polypropylene tubes in the dark at room temperature.

A small amount (approx. 3 mL) of the as-prepared suspension was used to extract AuNPs into chloroform containing octadecylamine.[274] AuNPs were analyzed via TEM after drop-casting from chloroform suspension, to obtain a particle size distribution for every batch that was subsequently used.

Synthesis of citrate-capped gold nanocrystals (~50 nm).

The synthetic procedure is analogous to the procedure described above for the smaller AuNPs, except that the concentrations of gold salt precursor and citrate reducing agent had been adapted: To a boiling aqueous solution of hydrogen tetrachloroaurate solution (100 mL, 0.30 mM, 1.0 equiv.) was added a hot solution of sodium citrate (1.6 mL, 34 mM, 1.8 equiv.).

Synthesis of tetraoctylammonium bromide-capped gold nanocrystals.

Tetraoctylammonium bromide-capped AuNPs were prepared by the two-phase Brust–Schiffrin synthesis as already reported elsewhere.[192] Briefly, hydrogen tetrachloroaurate trihydrate (94.5 mg, 0.240 mmol) dissolved in ultrapure water (20 mL) and tetra-*N*-octylammonium bromide (524.9 mg, 0.960 mmol) dissolved in toluene (20 mL) were added to a round bottom flask and the mixture was stirred vigorously for at least 30 minutes. The aqueous layer was then removed and the organic layer was degassed with argon for 15 minutes. A freshly prepared solution of sodium borohydride (72.6 mg, 1.92 mmol) in water (5 mL) was added dropwise under vigorous stirring. The mixture was stirred for further 5 hours. The organic layer was separated and washed with dilute sulfuric acid (5 %, 10 mL) and water (5 × 10 mL) and then dried over magnesium sulfate. The AuNPs prepared in this way were used for functionalization reactions directly after their synthesis and work-up.

A small amount (approx. 5 mL) of the as-prepared suspension was treated with $\mathbf{L^1}$ (20 mg) dissolved in toluene (1 mL) under ultrasonication. The obtained AuNPs were analyzed via TEM after drop-casting from toluene dispersion, to obtain a particle size distribution for every batch that was used in experiments.

Functionalization of tetraoctylammonium bromide-capped AuNPs with RAFT agent and telechelic and multiblock RAFT oligomer.

To a solution of the TOAB-capped Brust–Schiffrin AuNPs (1000 µL) was added the respective RAFT agent or RAFT oligomer in toluene (100 µL) under stirring. The amount of RAFT species added was 1 µmol for **L^1,** 0.5 µmol for telechelic RAFT agent **L^2** and telechelic RAFT oligomers **L^{2}a–e,** and 0.167 µmol for multiblock oligomers **L^{m}a–e**, such that a constant amount of TTC groups was present throughout all samples. Based on the amount of gold salt precursor used in the particle synthesis and on the average particle diameter determined by TEM, this means that a constant ratio of approx. 125:1 and 42:1 of macromolecules per particle was added in case of telechelic and multiblock RAFT oligomers, respectively. The mixtures were stirred overnight.

Functionalization of citrate-capped AuNPs – preparation of core–shell nanohybrids.

A solution of the respective RAFT polymer in acetone (5 mL, 4 mg mL^{-1} for grafting with 4-arm star polymers, 1 mL, 20 mg mL^{-1} for all other grafting reactions) was added to a colloidal dispersion of citrate-capped AuNPs (15 mL) under sonication at room temperature. The mixtures were incubated over night at room temperature and then subjected to three centrifugation-redispersion steps to remove nonbound polymer: first step: 8 hours, 8600 g, 0 °C, redispersion in 15 mL methanol; second and third step: 8 hours, 8600 g, –5 °C, redispersion in 15 mL dichloromethane. This allowed purification of the core–shell particles with a shell of linear or star-shaped RAFT polymer, respectively, by removing excess sodium citrate from the gold nanoparticle synthesis as well as excess polymer used in the polymer grafting step.

Functionalization of core–shell nanohybrids with Brust–Schiffrin AuNPs– preparation of planet–satellite structures.

A colloidal dispersion of Brust–Schiffrin AuNPs (1 mL) was added to core–shell nanohybrids at room temperature and the mixture was shaken for 10 minutes. A solution (1 mL, 40 mg for structures derived from 4-arm star polymer, 1 mg mL^{-1}, 20 mg mL^{-1} in all other cases) of linear polymer species in dichloromethane was added and the mixtures were shaken for 5 minutes and then centrifuged for 8 h at 8600 g and –5 °C. After redispersion in dichloromethane, this centrifugation was repeated to purify the planet–satellite structures. Colloidal dispersions of planet–satellite nanoobjects were obtained after redispersion in a respective solvent (i.e., methanol for the SAXS experiments, dichloromethane in all other cases).

Bibliography

(1) Diels, H.; Kranz, W. *Die Fragmente Der Vorsokratiker*; 1903.

(2) Whitesides, G. M.; Grzybowski, B. Self-Assembly at All Scales. *Science* **2002**, *295* (5564), 2418–2421.

(3) Moraes, J.; Ohno, K.; Maschmeyer, T.; Perrier, S. Selective Patterning of Gold Surfaces by Core/Shell, Semisoft Hybrid Nanoparticles. *Small* **2015**, *11* (4), 482–488.

(4) Ye, X.; Jiang, X.; Yu, B.; Yin, J.; Vana, P. Functional Binary Micropattern of Hyperbranched Poly(ether Amine) (hPEA-AN) Network and Poly(ether Amine) (PEA) Brush for Recognition of Guest Molecules. *Biomacromolecules* **2012**, *13* (2), 535–541.

(5) Waldrop, M. M. The Chips Are down for Moore's Law. *Nature* **2016**, *530* (7589), 144–147.

(6) Cui, Y.; Lieber, C. M. Functional Nanoscale Electronic Devices Assembled Using Silicon Nanowire Building Blocks. *Science* **2001**, *291* (5505), 851–853.

(7) Matthies, M.; Agarwal, N. P.; Schmidt, T. L. Design and Synthesis of Triangulated DNA Origami Trusses. *Nano Lett.* **2016**, *16* (3), 2108–2113.

(8) Yao, G.; Li, J.; Chao, J.; Pei, H.; Liu, H.; Zhao, Y.; Shi, J.; Huang, Q.; Wang, L.; Huang, W.; et al. Gold-Nanoparticle-Mediated Jigsaw-Puzzle-Like Assembly of Supersized Plasmonic DNA Origami. *Angew. Chemie Int. Ed.* **2015**, *54* (10), 2966–2969.

(9) Barner-Kowollik, C.; Goldmann, A. S.; Schacher, F. H. Polymer Interfaces: Synthetic Strategies Enabling Functionality, Adaptivity, and Spatial Control. *Macromolecules* **2016**, *49* (14), 5001–5516.

(10) Matyjaszewski, K.; Tsarevsky, N. V. Nanostructured Functional Materials Prepared by Atom Transfer Radical Polymerization. *Nat. Chem.* **2009**, *1* (4), 276–288.

(11) Moad, G.; Rizzardo, E.; Thang, S. H. Living Radical Polymerization by the RAFT Process - A Third Update. *Aust. J. Chem.* **2012**, *65* (8), 985–1076.

(12) Börner, H. G.; Duran, D.; Matyjaszewski, K.; Da Silva, M.; Sheiko, S. S. Synthesis of Molecular Brushes with Gradient in Grafting Density by Atom Transfer Polymerization. *Macromolecules* **2002**, *35* (9), 3387–3394.

(13) Matyjaszewski, K.; Qin, S.; Boyce, J. R.; Shirvanyants, D.; Sheiko, S. S. Effect of Initiation Conditions on the Uniformity of Three-Arm Star Molecular Brushes. *Macromolecules* **2003**, *36* (6), 1843–1849.

(14) Gody, G.; Rossner, C.; Moraes, J.; Vana, P.; Maschmeyer, T.; Perrier, S. One-Pot RAFT/"click" Chemistry via Isocyanates: Efficient Synthesis of α-End-Functionalized Polymers. *J. Am. Chem. Soc.* **2012**, *134* (30), 12596–12603.

(15) Moraes, J.; Maschmeyer, T.; Perrier, S. "Clickable" Polymers via a Conmbination of RAFT Polymerization and Isocyanate Chemistry. *J. Polym. Sci. Part A Polym. Chem.* **2011**, *49* (13), 2771–2782.

(16) Tietz, K.; Finkhäuser, S.; Samwer, K.; Vana, P. Stabilizing the Microphase Separation of Block Copolymers by Controlled Photo-Crosslinking. *Macromol. Chem. Phys.* **2014**, *215* (16), 1563–1572.

(17) Gody, G.; Maschmeyer, T.; Zetterlund, P. B.; Perrier, S. Rapid and Quantitative One-Pot Synthesis of Sequence-Controlled Polymers by Radical Polymerization. *Nat. Commun.* **2013**, *4*, 2505.

(18) Gody, G.; Zetterlund, P. B.; Perrier, S.; Harrisson, S. The Limits of Precision Monomer Placement in Chain Growth Polymerization. *Nat. Commun.* **2016**, *7*, 10514.

(19) Warren, N. J.; Armes, S. P. Polymerization-Induced Self-Assembly of Block Copolymer Nano-Objects via RAFT Aqueous Dispersion Polymerization. *J. Am. Chem. Soc.* **2014**, *136* (29), 10174–10185.

(20) Ullal, C. K.; Primpke, S.; Schmidt, R.; Böhm, U.; Egner, A.; Vana, P.; Hell, S. W. Flexible Microdomain Specific Staining of Block Copolymers for 3D Optical Nanoscopy. *Macromolecules* **2011**, *44* (19), 7508–7510.

(21) Luo, Q.; Hickey, R. J.; Park, S.-J. Controlling the Location of Nanoparticles in Colloidal Assemblies of Amphiphilic Polymers by Tuning Nanoparticle Surface Chemistry. *ACS Macro Lett.* **2013**, *2* (2), 107–111.

(22) Yoo, M.; Kim, S.; Jang, S. G.; Choi, S.-H.; Yang, H.; Kramer, E. J.; Lee, W. B.; Kim, B. J.; Bang, J. Controlling the Orientation of Block Copolymer Thin Films Using Thermally-Stable Gold Nanoparticles with Tuned Surface Chemistry. *Macromolecules* **2011**, *44* (23), 9356–9365.

(23) Velev, O. D.; Gupta, S. Materials Fabricated by Micro- and Nanoparticle Assembly - The Challenging Path from Science to Engineering. *Adv. Mater.* **2009**, *21* (19), 1897–1905.

(24) Li, D.; Jones, G. L.; Dunlap, J. R.; Hua, F.; Zhao, B. Thermosensitive Hairy Hybrid Nanoparticles Synthesized by Surface-Initiated Atom Transfer Radical Polymerization. *Langmuir* **2006**, *22* (7), 3344–3351.

(25) Takara, M.; Toyoshima, M.; Seto, H.; Hoshino, Y.; Miura, Y. Polymer-Modified Gold Nanoparticles via RAFT Polymerization: A Detailed Study for a Biosensing Application. *Polym. Chem.* **2014**, *5* (3), 931–939.

(26) Richards, S.-J.; Gibson, M. I. Optimization of the Polymer Coating for Glycosylated Gold Nanoparticle Biosensors to Ensure Stability and Rapid Optical Readouts. *ACS Macro Lett.* **2014**, *3* (10), 1004–1008.

(27) Lowe, A. B.; Sumerlin, B. S.; Donovan, M. S.; McCormick, C. L. Facile Preparation of Transition Metal Nanoparticles Stabilized by Well-Defined (Co)polymers Synthesized via Aqueous Reversible Addition-Fragmentation Chain Transfer Polymerization. *J. Am. Chem. Soc.* **2002**, *124* (39), 11562–11563.

(28) Ranjan, R.; Brittain, W. J. Combination of Living Radical Polymerization and Click Chemistry for Surface Modification. *Macromolecules* **2007**, *40* (17), 6217–6223.

(29) Li, C.; Benicewicz, B. C. Synthesis of Well-Defined Polymer Brushes Grafted onto Silica Nanoparticles via Surface Reversible Addition–Fragmentation Chain Transfer Polymerization. *Macromolecules* **2005**, *38* (14), 5929–5936.

(30) Nguyen, D. H.; Wood, M. R.; Zhao, Y.; Perrier, S.; Vana, P. Solid-Supported MADIX Polymerization of Vinyl Acetate. *Macromolecules* **2008**, *41* (19), 7071–7078.

(31) Garcia, M. A. Surface Plasmons in Metallic Nanoparticles: Fundamentals and Applications. *J. Phys. D. Appl. Phys.* **2011**, *44*, 283001.

(32) Duwez, A.-S.; Guillet, P.; Colard, C.; Gohy, J.-F.; Fustin, C.-A. Dithioesters and Trithiocarbonates as Anchoring Groups for the "Grafting-To" Approach. *Macromolecules* **2006**, *39* (8), 2729–2731.

(33) Fustin, C.-A.; Duwez, A.-S. Dithioesters and Trithiocarbonates Monolayers on Gold. *J. Electron Spectros. Relat. Phenomena* **2009**, *172* (1-3), 104–106.

(34) Pujari, S. P.; Scheres, L.; Marcelis, A. T. M.; Zuilhof, H. Covalent Surface Modification of Oxide Surfaces. *Angew. Chemie Int. Ed.* **2014**, *53* (25), 6322–6356.

(35) Huebner, D.; Koch, V.; Ebeling, B.; Mechau, J.; Steinhoff, J. E.; Vana, P. Comparison of Monomethoxy-, Dimethoxy-, and Trimethoxysilane Anchor Groups for Surface-Initiated RAFT Polymerization from Silica Surfaces. *J. Polym. Sci. Part A Polym. Chem.* **2015**, *53* (1), 103–113.

(36) Liu, W.; Greytak, A. B.; Lee, J.; Wong, C. R.; Park, J.; Marshall, L. F.; Jiang, W.; Curtin, P. N.; Ting, A. Y.; Nocera, D. G.; et al. Compact Biocompatible Quantum Dots via RAFT-Mediated Synthesis of Imidazole-Based Random Copolymer Ligand. *J. Am. Chem. Soc.* **2010**, *132* (2), 472–483.

(37) Gao, B.; Rozin, M. J.; Tao, A. R. Plasmonic Nanocomposites: Polymer-Guided Strategies for Assembling Metal Nanoparticles. *Nanoscale* **2013**, *5* (13), 5677–5691.

(38) Li, H.; John, J. V.; Byeon, S. J.; Heo, M. S.; Sung, J. H.; Kim, K.-H.; Kim, I. Controlled Accommodation of Metal Nanostructures within the Matrices of Polymer Architectures through Solution-Based Synthetic Strategies. *Prog. Polym. Sci.* **2014**, *39* (11), 1878–1907.

(39) Vogel, N.; Retsch, M.; Fustin, C. A.; Del Campo, A.; Jonas, U. Advances in Colloidal Assembly: The Design of Structure and Hierarchy in Two and Three Dimensions. *Chem. Rev.* **2015**, *115* (13), 6265–6311.

(40) Gibson, M. I.; Danial, M.; Klok, H.-A. Sequentially Modified, Polymer-Stabilized Gold Nanoparticle Libraries: Convergent Synthesis and Aggregation Behavior. *ACS Comb. Sci.* **2011**, *13* (3), 286–297.

(41) Freese, C.; Gibson, M. I.; Klok, H.-A.; Unger, R. E.; Kirkpatrick, C. J. Size- and Coating-Dependent Uptake of Polymer-Coated Gold Nanoparticles in Primary Human Dermal Microvascular Endothelial Cells. *Biomacromoleules* **2012**, *13* (5), 1533–1543.

(42) Blakey, I.; Merican, Z.; Thurecht, K. J. A Method for Controlling the Aggregation of Gold Nanoparticles: Tuning of Optical and Spectroscopic Properties. *Langmuir* **2013**, *29* (26), 8266–8274.

(43) Fasting, C.; Schalley, C. A.; Weber, M.; Seitz, O.; Hecht, S.; Koksch, B.; Dernedde, J.; Graf, C.; Knapp, E.-W.; Haag, R. Multivalency as a Chemical Organization and Action Principle. *Angew. Chemie Int. Ed.* **2012**, *51* (42), 10472–10498.

(44) Álvarez-Paino, M.; Bordegé, V.; Cuervo-Rodríguez, R.; Muñoz-Bonilla, A.; Fernández-García, M. Well-Defined Glycopolymers via RAFT Polymerization: Stabilization of Gold Nanoparticles. *Macromol. Chem. Phys.* **2014**, *215* (19), 1915–1924.

(45) Housni, A.; Cai, H.; Liu, S.; Pun, S. H.; Narain, R. Facile Preparation of Glyconanoparticles and Their Bioconjugation to Streptavidin. *Langmuir* **2007**, *23* (9), 5056–5061.

(46) Toyoshima, M.; Miura, Y. Preparation of Glycopolymer-Substituted Gold Nanoparticles and Their Molecular Recognition. *J. Polym. Sci. Part A Polym. Chem.* **2009**, *47* (5), 1412–1421.

(47) Spain, S. G.; Albertin, L.; Cameron, N. R. Facile in Situ Preparation of Biologically Active Multivalent Glyconanoparticles. *Chem. Commun.* **2006**, No. 40, 4198–4200.

(48) Lu, J.; Zhang, W.; Richards, S.-J.; Gibson, M. I.; Chen, G. Glycopolymer-Coated Gold Nanorods Synthesised by a One Pot copper(0) Catalyzed Tandem RAFT/click Reaction. *Polym. Chem.* **2014**, *5* (7), 2326–2332.

(49) Li, X.; Bao, M.; Weng, Y.; Yang, K.; Zhang, W.; Chen, G. Glycopolymer-Coated Iron Oxide Nanoparticles: Shape-Controlled Synthesis and Cellular Uptake. *J. Mater. Chem. B* **2014**, *2* (34), 5569–5575.

(50) Li, J.; Han, C.; Wu, W.; Zhang, S.; Guo, J.; Zhou, H. Selective and Cyclic Detection of Cr^{3+} Using Poly(methylacrylic Acid) Monolayer Protected Gold Nanoparticles. *New J. Chem.* **2014**, *38* (2), 717–722.

(51) Celiz, A. D.; Lee, T.-C.; Scherman, O. A. Polymer-Mediated Dispersion of Gold Nanoparticles: Using Supramolecular Moieties on the Periphery. *Adv. Mater.* **2009**, *21* (38-39), 3937–3940.

(52) Ohno, K.; Koh, K.; Tsujii, Y.; Fukuda, T. Fabrication of Ordered Arrays of Gold Nanoparticles Coated with High-Density Polymer Brushes. *Angew. Chemie Int. Ed.* **2003**, *42* (24), 2751–2754.

(53) Ohno, K.; Morinaga, T.; Koh, K.; Tsujii, Y.; Fukuda, T. Synthesis of Monodisperse Silica Particles Coated with Well-Defined, High-Density Polymer Brushes by Surface-Initiated Atom Transfer Radical Polymerization. *Macromolecules* **2005**, *38* (6), 2137–2142.

(54) Boyer, C.; Whittaker, M. R.; Luzon, M.; Davis, T. P. Design and Synthesis of Dual Thermoresponsive and Antifouling Hybrid Polymer/Gold Nanoparticles. *Macromolecules* **2009**, *42* (18), 6917–6926.

(55) Ohno, K.; Morinaga, T.; Takeno, S.; Tsujii, Y.; Fukuda, T. Suspensions of Silica Particles Grafted with Concentrated Polymer Brush: Effects of Graft Chain Length on Brush Layer Thickness and Colloidal Crystallization. *Macromolecules* **2007**, *40* (25), 9143–9150.

(56) Morinaga, T.; Ohno, K.; Tsujii, Y.; Fukuda, T. Structural Analysis of "Semisoft" Colloidal Crystals by Confocal Laser Scanning Microscopy. *Macromolecules* **2008**, *41* (10), 3620–3626.

(57) Ohno, K.; Akashi, T.; Huang, Y.; Tsujii, Y. Surface-Initiated Living Radical Polymerization from Narrowly Size-Distributed Silica Nanoparticles of Diameters Less Than 100 Nm. *Macromolecules* **2010**, *43* (21), 8805–8812.

(58) Ohno, K.; Morinaga, T.; Takeno, S.; Tsujii, Y.; Fukuda, T. Suspensions of Silica Particles Grafted with Concentrated Polymer Brush: A New Family of Colloidal Crystals. *Macromolecules* **2006**, *39* (3), 1245–1249.

(59) Daoud, M.; Cotton, J. P. Star Shaped Polymers: A Model for the Conformation and Its Concentration Dependence. *J. Phys.* **1982**, *43* (3), 531–538.

(60) Dukes, D.; Li, Y.; Lewis, S.; Benicewicz, B.; Schadler, L.; Kumar, S. K. Conformational Transitions of Spherical Polymer Brushes: Synthesis, Characterization, and Theory. *Macromolecules* **2010**, *43* (3), 1564–1570.

(61) Choi, J.; Dong, H.; Matyjaszewski, K.; Bockstaller, M. R. Flexible Particle Array Structures by Controlling Polymer Graft Architecture. *J. Am. Chem. Soc.* **2010**, *132* (36), 12537–12539.

(62) Choi, J.; Hui, C. M.; Pietrasik, J.; Dong, H.; Matyjaszewski, K.; Bockstaller, M. R. Toughening Fragile Matter: Mechanical Properties of Particle Solids Assembled from Polymer-Grafted Hybrid Particles Synthesized by ATRP. *Soft Matter* **2012**, *8* (15), 4072–4082.

(63) Choi, J.; Hui, C. M.; Schmitt, M.; Pietrasik, J.; Margel, S.; Matyjazsewski, K.; Bockstaller, M. R. Effect of Polymer-Graft Modification on the Order Formation in Particle Assembly Structures. *Langmuir* **2013**, *29* (21), 6452–6459.

(64) Rungta, A.; Natarajan, B.; Neely, T.; Dukes, D.; Schadler, L. S.; Benicewicz, B. C. Grafting Bimodal Polymer Brushes on Nanoparticles Using Controlled Radical Polymerization. *Macromolecules* **2012**, *45* (23), 9303–9311.

(65) Akcora, P.; Liu, H.; Kumar, S. K.; Moll, J.; Li, Y.; Benicewicz, B. C.; Schadler, L. S.; Acehan, D.; Panagiotopoulos, A. Z.; Pryamitsyn, V.; et al. Anisotropic Self-Assembly of Spherical Polymer-Grafted Nanoparticles. *Nat. Mater.* **2009**, *8* (4), 354–359.

(66) Goel, V.; Pietrasik, J.; Dong, H.; Sharma, J.; Matyjaszewski, K.; Krishnamoorti, R. Structure of Polymer Tethered Highly Grafted Nanoparticles. *Macromolecules* **2011**, *44* (20), 8129–8135.

(67) Yockell-Lelièvre, H.; Gingras, D.; Vallée, R.; Ritcey, A. M. Coupling of Localized Surface Plasmon Resonance in Self-Organized Polystyrene-Capped Gold Nanoparticle Films. *J. Phys. Chem. C* **2009**, *113* (51), 21293–21302.

(68) Karg, M.; Hellweg, T.; Mulvaney, P. Self-Assembly of Tunable Nanocrystal Superlattices Using Poly-(NIPAM) Spacers. *Adv. Funct. Mater.* **2011**, *21* (24), 4668–4676.

(69) Ohno, K.; Ma, Y.; Huang, Y.; Mori, C.; Yahata, Y.; Tsujii, Y.; Maschmeyer, T.; Moraes, J.; Perrier, S. Surface-Initiated Reversible Addition–Fragmentation Chain Transfer (RAFT) Polymerization from Fine Particles Functionalized with Trithiocarbonates. *Macromolecules* **2011**, *44* (22), 8944–8953.

(70) Moraes, J.; Ohno, K.; Gody, G.; Maschmeyer, T.; Perrier, S. The Synthesis of Well-Defined Poly(vinylbenzyl chloride)-Grafted Nanoparticles via RAFT Polymerization. *Beilstein J. Org. Chem.* **2013**, *9*, 1226–1234.

(71) Ebeling, B.; Vana, P. RAFT-Polymers with Single and Multiple Trithiocarbonate Groups as Uniform Gold-Nanoparticle Coatings. *Macromolecules* **2013**, *46* (12), 4862–4871.

(72) Yockell-Lelièvre, H.; Desbiens, J.; Ritcey, A. M. Two-Dimensional Self-Organization of Polystyrene-Capped Gold Nanoparticles. *Langmuir* **2007**, *23* (5), 2843–2850.

(73) Wang, Y.; Yang, G.; Tang, P.; Qiu, F.; Yang, Y.; Zhu, L. Mixed Homopolymer Brushes Grafted onto a Nanosphere. *J. Chem. Phys.* **2011**, *134* (13), 134903.

(74) Wang, J.; Müller, M. Microphase Separation of Mixed Polymer Brushes: Dependence of the Morphology on Grafting Density, Composition, Chain-Length Asymmetry, Solvent Quality, and Selectivity. *J. Phys. Chem. B* **2009**, *113* (33), 11384–11402.

(75) Jiang, X.; Zhong, G.; Horton, J. M.; Jin, N.; Zhu, L.; Zhao, B. Evolution of Phase Morphology of Mixed Poly(tert-butyl acrylate)/Polystyrene Brushes Grafted on Silica Particles with the Change of Chain Length Disparity. *Macromolecules* **2010**, *43* (12), 5387–5395.

(76) Wang, Z.-L.; Xu, J.-T.; Du, B.-Y.; Fan, Z.-Q. Facile Fabrication of Amphiphilic Gold Nanoparticles with V-Shaped Brushes from Block Copolymers with a Trithiocarbonate Group as the Junction. *J. Colloid Interface Sci.* **2011**, *360* (2), 350–354.

(77) Kotsuchibashi, Y.; Ebara, M.; Aoyagi, T.; Narain, R. Fabrication of Doubly Responsive Polymer Functionalized Silica Nanoparticles via a Simple Thiol–ene Click Chemistry. *Polym. Chem.* **2012**, *3* (9), 2545–2550.

(78) Li, D.; Sheng, X.; Zhao, B. Environmentally Responsive "Hairy" Nanoparticles: Mixed Homopolymer Brushes on Silica Nanoparticles Synthesized by Living Radical Polymerization Techniques. *J. Am. Chem. Soc.* **2005**, *127* (7), 6248–6256.

(79) Zhu, L.; Zhao, B. Transmission Electron Microscopy Study of Solvent-Induced Phase Morphologies of Environmentally Responsive Mixed Homopolymer Brushes on Silica Particles. *J. Phys. Chem. B* **2008**, *112* (37), 11529–11536.

(80) Zhao, B.; Zhu, L. Nanoscale Phase Separation in Mixed Poly (tert-butyl acrylate)/Polystyrene Brushes on Silica Nanoparticles under Equilibrium Melt Conditions. *J. Am. Chem. Soc.* **2006**, *128* (14), 4574–4575.

(81) Bao, C.; Tang, S.; Wright, R. A. E.; Tang, P.; Qiu, F.; Zhu, L.; Zhao, B. Effect of Molecular Weight on Lateral Microphase Separation of Mixed Homopolymer Brushes Grafted on Silica Particles. *Macromolecules* **2014**, *47* (19), 6824–6835.

(82) Bao, C.; Tang, S.; Horton, J. M.; Jiang, X.; Tang, P.; Qiu, F.; Zhu, L.; Zhao, B. Effect of Overall Grafting Density on Microphase Separation of Mixed Homopolymer Brushes Synthesized from Y-Initiator-Functionalized Silica Particles. *Macromolecules* **2012**, *45* (19), 8027–8036.

(83) Horton, J. M.; Tang, S.; Bao, C.; Tang, P.; Qiu, F.; Zhu, L.; Zhao, B. Truncated Wedge-Shaped Nanostructures Formed from Lateral Microphase Separation of Mixed Homopolymer Brushes Grafted on 67 nm Silica Nanoparticles: Evidence of the Effect of Substrate Curvature. *ACS Macro Lett.* **2012**, *1* (8), 1061–1065.

(84) Tang, S.; Lo, T.-Y.; Horton, J. M.; Bao, C.; Tang, P.; Qiu, F.; Ho, R.-M.; Zhao, B.; Zhu, L. Direct Visualization of Three-Dimensional Morphology in Hierarchically Self-Assembled Mixed Poly(tert-butyl acrylate)/Polystyrene Brush-Grafted Silica Nanoparticles. *Macromolecules* **2013**, *46* (16), 6575–6584.

(85) Santer, S.; Kopyshev, A.; Donges, J.; Rühe, J.; Jiang, X.; Zhao, B.; Müller, M. Memory of Surface Patterns in Mixed Polymer Brushes: Simulation and Experiment. *Langmuir* **2007**, *23* (22), 279–285.

(86) Shan, J.; Nuopponen, M.; Jiang, H.; Viitala, T.; Kauppinen, E.; Kontturi, K.; Tenhu, H. Amphiphilic Gold Nanoparticles Grafted with Poly (N-Isopropylacrylamide) and Polystyrene. *Macromolecules* **2005**, *38* (7), 2918–2926.

(87) Ionov, L.; Minko, S. Mixed Polymer Brushes with Locking Switching. *ACS Appl. Mater. Interfaces* **2012**, *4* (1), 483–489.

(88) Cheng, L.; Song, J.; Yin, J.; Duan, H. Self-Assembled Plasmonic Dimers of Amphiphilic Gold Nanocrystals. *J. Phys. Chem. Lett.* **2011**, *2* (17), 2258–2262.

(89) Song, J.; Cheng, L.; Liu, A.; Yin, J.; Kuang, M.; Duan, H. Plasmonic Vesicles of Amphiphilic Gold Nanocrystals: Self-Assembly and External-Stimuli-Triggered Destruction. *J. Am. Chem. Soc.* **2011**, *133* (28), 10760–10763.

(90) Song, J.; Zhou, J.; Duan, H. Self-Assembled Plasmonic Vesicles of SERS-Encoded Amphiphilic Gold Nanoparticles for Cancer Cell Targeting and Traceable Intracellular Drug Delivery. *J. Am. Chem. Soc.* **2012**, *134* (32), 13458–13469.

(91) Song, J.; Pu, L.; Zhou, J.; Duan, B.; Duan, H. Biodegradable Theranostic Plasmonic Vesicles of Amphiphilic Gold Nanorods. *ACS Nano* **2013**, *7* (11), 9947–9960.

(92) Basuki, J. S.; Duong, H. T. T.; Macmillan, A.; Whan, R.; Boyer, C.; Davis, T. P. Polymer-Grafted, Nonfouling, Magnetic Nanoparticles Designed to Selectively Store and Release Molecules via Ionic Interactions. *Macromolecules* **2013**, *46* (17), 7043–7054.

(93) Yuan, J.-J.; Schmid, A.; Armes, S. P.; Lewis, A. L. Facile Synthesis of Highly Biocompatible Poly (2-(methacryloyloxy)ethyl Phosphorylcholine)-Coated Gold Nanoparticles in Aqueous Solution. *Langmuir* **2006**, *22* (23), 11022–11027.

(94) Song, J.; Duan, B.; Wang, C.; Zhou, J.; Pu, L.; Fang, Z.; Wang, P.; Lim, T. T.; Duan, H. SERS-Encoded Nanogapped Plasmonic Nanoparticles: Growth of Metallic Nanoshell by Templating Redox-Active Polymer Brushes. *J. Am. Chem. Soc.* **2014**, *136* (19), 6838–6841.

(95) Marcelo, G.; Martinho, J. M. G.; Farinha, J. P. S. Polymer-Coated Nanoparticles by Adsorption of Hydrophobically Modified Poly(N,N-Dimethylacrylamide). *J. Phys. Chem. B* **2013**, *117* (12), 3416–3427.

(96) Kang, Y.; Taton, T. A. Core/Shell Gold Nanoparticles by Self-Assembly and Crosslinking of Micellar, Block-Copolymer Shells. *Angew. Chemie Int. Ed.* **2005**, *44* (3), 409–412.

(97) Chen, H. Y.; Abraham, S.; Mendenhall, J.; Delamarre, S. C.; Smith, K.; Kim, I.; Batt, C. A. Encapsulation of Single Small Gold Nanoparticles by Diblock Copolymers. *Chemphyschem* **2008**, *9* (3), 388–392.

(98) Kang, Y.; Taton, T. A. Controlling Shell Thickness in Core-Shell Gold Nanoparticles via Surface-Templated Adsorption of Block Copolymer Surfactants. *Macromolecules* **2005**, *38* (14), 6115–6121.

(99) Kim, B.-S.; Qiu, J.-M.; Wang, J.-P.; Taton, T. A. Magnetomicelles: Composite Nanostructures from Magnetic Nanoparticles and Cross-Linked Amphiphilic Block Copolymers. *Nano Lett.* **2005**, *5* (10), 1987–1991.

(100) Li, Y.; Smith, A. E.; Lokitz, B. S.; McCormick, C. L. In Situ Formation of Gold-"Decorated" Vesicles from a RAFT-Synthesized, Thermally Responsive Block Copolymer. *Macromolecules* **2007**, *40* (24), 8524–8526.

(101) Smith, A. E.; Xu, X.; Abell, T. U.; Kirkland, S. E.; Hensarling, R. M.; McCormick, C. L. Tuning Nanostructure Morphology and Gold Nanoparticle "Locking" of Multi-Responsive Amphiphilic Diblock Copolymers. *Macromolecules* **2009**, *42* (8), 2958–2964.

(102) Hickey, R. J.; Haynes, A. S.; Kikkawa, J. M.; Park, S.-J. Controlling the Self-Assembly Structure of Magnetic Nanoparticles and Amphiphilic Block-Copolymers: From Micelles to Vesicles. *J. Am. Chem. Soc.* **2011**, *133* (5), 1517–1525.

(103) Kamps, A. C.; Sanchez-Gaytan, B. L.; Hickey, R. J.; Clarke, N.; Fryd, M.; Park, S.-J. Nanoparticle-Directed Self-Assembly of Amphiphilic Block Copolymers. *Langmuir* **2010**, *26* (17), 14345–14350.

(104) Sanchez-Gaytan, B. L.; Cui, W.; Kim, Y.; Mendez-Polanco, M. A.; Duncan, T. V.; Fryd, M.; Wayland, B. B.; Park, S.-J. Interfacial Assembly of Nanoparticles in Discrete Block-Copolymer Aggregates. *Angew. Chemie Int. Ed.* **2007**, *46* (48), 9235–9238.

(105) Liu, Y.; Li, Y.; He, J.; Duelge, K. J.; Lu, Z.; Nie, Z. Entropy-Driven Pattern Formation of Hybrid Vesicular Assemblies Made from Molecular and Nanoparticle Amphiphiles. *J. Am. Chem. Soc.* **2014**, *136* (6), 2602–2610.

(106) Mai, Y.; Eisenberg, A. Self-Assembly of Block Copolymers. *Chem. Soc. Rev.* **2012**, *41* (18), 5969–5985.

(107) Matsen, M. W.; Thompson, R. B. Particle Distributions in a Block Copolymer Nanocomposite. *Macromolecules* **2008**, *41* (5), 1853–1860.

(108) Chiu, J. J.; Kim, B. J.; Yi, G.-R.; Bang, J.; Kramer, E. J.; Pine, D. J. Distribution of Nanoparticles in Lamellar Domains of Block Copolymers. *Macromolecules* **2007**, *40* (9), 3361–3365.

(109) Chiu, J. J.; Kim, B. J.; Kramer, E. J.; Pine, D. J. Control of Nanoparticle Location in Block Copolymers. *J. Am. Chem. Soc.* **2005**, *127* (14), 5036–5037.

(110) Li, Q.; He, J.; Glogowski, E.; Li, X.; Wang, J.; Emrick, T.; Russell, T. P. Responsive Assemblies: Gold Nanoparticles with Mixed Ligands in Microphase Separated Block Copolymers. *Adv. Mater.* **2008**, *20* (8), 1462–1466.

(111) Lin, Y.; Böker, A.; He, J.; Sill, K.; Xiang, H.; Abetz, C.; Li, X.; Wang, J.; Emrick, T.; Long, S.; et al. Self-Directed Self-Assembly of Nanoparticle/copolymer Mixtures. *Nature* **2005**, *434* (7029), 55–59.

(112) He, J.; Tangirala, R.; Emrick, T.; Russell, T. P.; Böker, A.; Li, X.; Wang, J. Self-Assembly of Nanoparticle–Copolymer Mixtures: A Kinetic Point of View. *Adv. Mater.* **2007**, *19* (3), 381–385.

(113) Son, J. G.; Bae, W. K.; Kang, H.; Nealey, P. F.; Char, K. Placement Control of Nanomaterial Arrays on the Surface-Reconstructed Block Copolymer Thin Films. *ACS Nano* **2009**, *3* (12), 3927–3934.

(114) Xu, C.; Ohno, K.; Ladmiral, V.; Milkie, D. E.; Kikkawa, J. M.; Composto, R. J. Simultaneous Block Copolymer and Magnetic Nanoparticle Assembly in Nanocomposite Films. *Macromolecules* **2009**, *42* (4), 1219–1228.

(115) Kim, B. J.; Fredrickson, G. H.; Hawker, C. J.; Kramer, E. J. Nanoparticle Surfactants as a Route to Bicontinuous Block Copolymer Morphologies. *Langmuir* **2007**, *23* (14), 7804–7809.

(116) Karagoz, B.; Yeow, J.; Esser, L.; Prakash, S. M.; Kuchel, R. P.; Davis, T. P.; Boyer, C. An Efficient and Highly Versatile Synthetic Route to Prepare Iron Oxide Nanoparticles/Nanocomposites with Tunable Morphologies. *Langmuir* **2014**, *30* (34), 10493–10502.

(117) Bleach, R.; Karagoz, B.; Prakash, S. M.; Davis, T. P.; Boyer, C. In Situ Formation of Polymer−Gold Composite Nanoparticles with Tunable Morphologies. *ACS Macro Lett.* **2014**, *3* (7), 591–596.

(118) Duxin, N.; Liu, F.; Vali, H.; Eisenberg, A. Cadmium Sulphide Quantum Dots in Morphologically Tunable Triblock Copolymer Aggregates. *J. Am. Chem. Soc.* **2005**, *127* (28), 10063–10069.

(119) Niu, H.; Zhang, L.; Gao, M.; Chen, Y. Amphiphilic ABC Triblock Copolymer-Assisted Synthesis of Core/Shell Structured CdTe Nanowires. *Langmuir* **2005**, *21* (9), 4205–4210.

(120) Azzam, T.; Bronstein, L.; Eisenberg, A. Water-Soluble Surface-Anchored Gold and Palladium Nanoparticles Stabilized by Exchange of Low Molecular Weight Ligands with Biamphiphilic Triblock Copolymers. *Langmuir* **2008**, *24* (13), 6521–6529.

(121) Krüger, C.; Agarwal, S.; Greiner, A. Stoichiometric Functionalization of Gold Nanoparticles in Solution through a Free Radical Polymerization Approach. *J. Am. Chem. Soc.* **2008**, *130* (9), 2710–2711.

(122) Hu, J.; Wu, T.; Zhang, G.; Liu, S. Efficient Synthesis of Single Gold Nanoparticle Hybrid Amphiphilic Triblock Copolymers and Their Controlled Self-Assembly. *J. Am. Chem. Soc.* **2012**, *134* (18), 7624–7627.

(123) Hu, B.; Henn, D. M.; Wright, R. A. E.; Zhao, B. Hybrid Micellar Hydrogels of a Thermosensitive ABA Triblock Copolymer and Hairy Nanoparticles: Effect of Spatial Location of Hairy Nanoparticles on Gel Properties. *Langmuir* **2014**, *30* (37), 11212–11224.

(124) Ebeling, B.; Vana, P. Multiblock Copolymers of Styrene and Butyl Acrylate via Polytrithiocarbonate-Mediated RAFT Polymerization. *Polymers (Basel).* **2011**, *3* (4), 719–739.

(125) You, Y.-Z.; Hong, C.-Y.; Pan, C.-Y. A Novel Strategy for Synthesis of Multiblock Copolymers. *Chem. Commun.* **2002**, No. 23, 2800–2801.

(126) Hong, J.; Wang, Q.; Fan, Z. Synthesis of Multiblock Polymer Containing Narrow Polydispersity Blocks. *Macromol. Rapid Commun.* **2006**, *27* (1), 57–62.

(127) Ebeling, B.; Eggers, M.; Vana, P. Ideal Molecular Weight Distributions of Multiblock Copolymers Prepared via RAFT Polymerization. *Macromolecules* **2010**, *43* (24), 10283–10290.

(128) Rossner, C.; Ebeling, B.; Vana, P. Design Strategies for the Fabrication of Tailored Nanocomposites via RAFT Polymerization. In *ACS Symposium Series*; Matyjaszewski, K., Ed.; American Chemical Society: Washington, DC, 2015; pp 293–307.

(129) Du, B.; Chen, X.; Zhao, B.; Mei, A.; Wang, Q.; Xu, J.; Fan, Z. Interfacial Entrapment of Noble Metal Nanoparticles and Nanorods Capped with Amphiphilic Multiblock Copolymer at a Selective Liquid-Liquid Interface. *Nanoscale* **2010**, *2* (9), 1684–1689.

(130) Mori, H.; Seng, D. C.; Zhang, M.; Müller, A. H. E. Hybrid Nanoparticles with Hyperbranched Polymer Shells via Self-Condensing Atom Transfer Radical Polymerization from Silica Surfaces. *Langmuir* **2002**, *18* (17), 3682–3693.

(131) Dey, P.; Blakey, I.; Thurecht, K. J.; Fredericks, P. M. Self-Assembled Hyperbranched Polymer-Gold Nanoparticle Hybrids: Understanding the Effect of Polymer Coverage on Assembly Size and SERS Performance. *Langmuir* **2013**, *29* (2), 525–533.

(132) Dey, P.; Blakey, I.; Thurecht, K. J.; Fredericks, P. M. Hyperbranched Polymer-Gold Nanoparticle Assemblies: Role of Polymer Architecture in Hybrid Assembly Formation and SERS Activity. *Langmuir* **2014**, *30* (8), 2249–2258.

(133) Dey, P.; Zhu, S.; Thurecht, K. J.; Fredericks, P. M.; Blakey, I. Self Assembly of Plasmonic Core–satellite Nano-Assemblies Mediated by Hyperbranched Polymer Linkers. *J. Mater. Chem. B* **2014**, *2* (19), 2827–2837.

(134) Jiang, W.; Schalley, C. A. Integrative Self-Sorting Is a Programming Language for High Level Self-Assembly. *Proc. Natl. Acad. Sci. U. S. A.* **2009**, *106* (26), 10425–10429.

(135) Jiang, W.; Schäfer, A.; Mohr, P. C.; Schalley, C. A. Monitoring Self-Sorting by Electrospray Ionization Mass Spectrometry: Formation Intermediates and Error-Correction during the Self-Assembly of Multiply Threaded Pseudorotaxanes. *J. Am. Chem. Soc.* **2010**, *132* (7), 2309–2320.

(136) Love, J. C.; Estroff, L. A.; Kriebel, J. K.; Nuzzo, R. G.; Whitesides, G. M. Self-Assembled Monolayers of Thiolates on Metals as a Form of Nanotechnology. *Chem. Rev.* **2005**, *105* (4), 1103–1169.

(137) Zhu, M.-Q.; Wang, L.-Q.; Exarhos, G. J.; Li, A. D. Q. Thermosensitive Gold Nanoparticles. *J. Am. Chem. Soc.* **2004**, *126* (9), 2656–2657.

(138) Corbierre, M. K.; Cameron, N. S.; Lennox, R. B. Polymer-Stabilized Gold Nanoparticles with High Grafting Densities. *Langmuir* **2004**, *20* (7), 2867–2873.

(139) Sugata, E.; Kobatake, S. Synthesis and Optical Properties of Gold Nanoparticle Networks Cross-Linked with Chain-Length-Controlled Polymers. *RSC Adv.* **2015**, *5* (44), 34704–34708.

(140) Jadzinsky, P. D.; Calero, G.; Ackerson, C. J.; Bushnell, D. A.; Kornberg, R. D. Structure of a Thiol Monolayer-Protected Gold Nanoparticle at 1.1 Å Resolution. *Science* **2007**, *318* (5849), 430–433.

(141) Qian, H.; Eckenhoff, W. T.; Zhu, Y.; Pintauer, T.; Jin, R. Total Structure Determination of Thiolate-Protected Au_{38} Nanoparticles. *J. Am. Chem. Soc.* **2010**, *132* (24), 8280–8281.

(142) Zeng, C.; Li, T.; Das, A.; Rosi, N. L.; Jin, R. Chiral Structure of Thiolate-Protected 28-Gold-Atom Nanocluster Determined by X-Ray Crystallography. *J. Am. Chem. Soc.* **2013**, *135* (27), 10011–10013.

(143) Das, A.; Liu, C.; Byun, H. Y.; Nobusada, K.; Zhao, S.; Rosi, N.; Jin, R. Structure Determination of $[Au_{18}(SR)_{14}]$. *Angew. Chemie Int. Ed.* **2015**, *54* (10), 3140–3144.

(144) Chen, S.; Wang, S.; Zhong, J.; Song, Y.; Zhang, J.; Sheng, H.; Pei, Y.; Zhu, M. The Structure and Optical Properties of the $[Au_{18}(SR)_{14}]$ Nanocluster. *Angew. Chemie Int. Ed.* **2015**, *54* (10), 3145–3149.

(145) Dass, A.; Theivendran, S.; Nimmala, P. R.; Kumara, C.; Jupally, V. R.; Fortunelli, A.; Sementa, L.; Barcaro, G.; Zuo, X.; Noll, B. C. $Au_{133}(SPh\text{-}tBu)_{52}$ Nanomolecules: X-Ray Crystallography, Optical, Electrochemical, and Theoretical Analysis. *J. Am. Chem. Soc.* **2015**, *137* (14), 4610–4613.

(146) Chen, Y.; Zeng, C.; Liu, C.; Kirschbaum, K.; Gayathri, C.; Gil, R. R.; Rosi, N. L.; Jin, R. Crystal Structure of Barrel-Shaped Chiral $Au_{130}(p\text{-}MBT)_{50}$ Nanocluster. *J. Am. Chem. Soc.* **2015**, *137* (32), 10076–10079.

(147) Weinberger, D. S.; Melaimi, M.; Moore, C. E.; Rheingold, A. L.; Frenking, G.; Jerabek, P.; Bertrand, G. Isolation of Neutral Mono- and Dinuclear Gold Complexes of Cyclic (alkyl)(amino)carbenes. *Angew. Chemie Int. Ed.* **2013**, *52* (34), 8964–8967.

(148) Blakey, I.; Schiller, T. L.; Merican, Z.; Fredericks, P. M. Interactions of Phenyldithioesters with Gold Nanoparticles (AuNPs): Implications for AuNP Functionalization and Molecular Barcoding of AuNP Assemblies. *Langmuir* **2010**, *26* (2), 692–701.

(149) Liu, Y.; Sun, C.; Bolin, T.; Wu, T.; Liu, Y.; Sternberg, M.; Sun, S.; Lin, X. M. Kinetic Pathway of Palladium Nanoparticle Sulfidation Process at High Temperatures. *Nano Lett.* **2013**, *13* (10), 4893–4901.

(150) Morinaga, T.; Ohno, K.; Tsujii, Y.; Fukuda, T. Two-Dimensional Ordered Arrays of Monodisperse Silica Particles Grafted with Concentrated Polymer Brushes. *Eur. Polym. J.* **2007**, *43* (1), 243–248.

(151) Horiuchi, S.; Hanada, T.; Ebisawa, M.; Matsuda, Y.; Kobayashi, M.; Takahara, A. Contamination-Free Transmission Electron Microscopy for High-Resolution Carbon Elemental Mapping of Polymers. *ACS Nano* **2009**, *3* (5), 1297–1304.

(152) Jung, S. H.; Jeon, J.; Kim, H.; Jaworski, J.; Jung, J. H. Chiral Arrangement of Achiral Au Nanoparticles by Supramolecular Assembly of Helical Nanofiber Templates. *J. Am. Chem. Soc.* **2014**, *136* (17), 6446–6452.

(153) Guyon, F.; Hameau, A.; Khatyr, A.; Knorr, M.; Amrouche, H.; Fortin, D.; Harvey, P. D.; Strohmann, C.; Ndiaye, A. L.; Huch, V.; et al. Syntheses, Structures, and Photophysical Properties of Mono- and Dinuclear Sulfur-Rich gold(I) Complexes. *Inorg. Chem.* **2008**, *47* (17), 7483–7492.

(154) Schmidbaur, H.; Schier, A. Aurophilic Interactions as a Subject of Current Research: An up-Date. *Chem. Soc. Rev.* **2012**, *41* (1), 370–412.

(155) Teo, P.; Wang, J.; Koh, L. L.; Hor, T. S. A. Isolation of Cationic Digold-Frame with Free Carboxylic Acid Pendants. *Dalt. Trans.* **2009**, No. 25, 5009–5014.

(156) Wiedemann, D.; Gamer, M. T.; Roesky, P. W. Substituted Bisphosphanylamines as Ligands in gold(I) Chemistry - Synthesis and Structures. *Zeitschrift fur Anorg. und Allg. Chemie* **2009**, *635* (1), 125–129.

(157) Yusa, S.; Fukuda, K.; Yamamoto, T.; Iwasaki, Y.; Watanabe, A.; Akiyoshi, K.; Morishima, Y. Salt Effect on the Heat-Induced Association Behavior of Gold Nanoparticles Coated with Poly(N-Isopropylacrylamide) Prepared via Reversible Addition−Fragmentation Chain Transfer (RAFT) Radical Polymerization. *Langmuir* **2007**, *23* (26), 12842–12848.

(158) Hotchkiss, J. W.; Lowe, A. B.; Boyes, S. G. Surface Modification of Gold Nanorods with Polymers Synthesized by Reversible Addition-Fragmentation Chain Transfer Polymerization. *Chem. Mater.* **2007**, *19* (1), 6–13.

(159) Walczak, M. M.; Alves, C. A.; Lamp, B. D.; Porter, M. D. Electrochemical and X-Ray Photoelectron Spectroscopic Evidence for Differences in the Binding Sites of Alkanethiolate Monolayers Chemisorbed at Gold. *J. Electroanal. Chem.* **1995**, *396* (1-2), 103–114.

(160) Nuzzo, R. G.; Zegarski, B. R.; Dubois, L. H. Fundamental Studies of the Chemisorption of Organosulfur Compounds on Au(111). Implications for Molecular Self-Assembly on Gold Surfaces. *J. Am. Chem. Soc.* **1987**, *109* (3), 733–740.

(161) Kankate, L.; Turchanin, A.; Gölzhäuser, A. On the Release of Hydrogen from the S-H Groups in the Formation of Self-Assembled Monolayers of Thiols. *Langmuir* **2009**, *25* (18), 10435–10438.

(162) Nuzzo, R. G.; Dubois, L. H.; Allara, D. L. Fundamental Studies Of Microscopic Wetting On Organic-Surfaces. 1. Formation And Structural Characterization Of A Self-Consistent Series Of Polyfunctional Organic Monolayers. *J. Am. Chem. Soc.* **1990**, *112* (2), 558–569.

(163) Schlenoff, J. B.; Li, M.; Ly, H. Stability and Self-Exchange in Alkanethiol Monolayers. *J. Am. Chem. Soc.* **1995**, *117* (50), 12528–12536.

(164) Lai, J. T.; Filla, D.; Shea, R. Functional Polymers from Novel Carboxyl-Terminated Trithiocarbonates as Highly Efficient RAFT Agents. *Macromolecules* **2002**, *35* (18), 6754–6756.

(165) Kreibing, U.; Vollmer, M. *Optical Properties of Metal Clusters*; Springer: New York, 1995.

(166) Sendroiu, I. E.; Mertens, S. F. L.; Schiffrin, D. J. Plasmon Interactions between Gold Nanoparticles in Aqueous Solution with Controlled Spatial Separation. *Phys. Chem. Chem. Phys.* **2006**, *8* (12), 1430–1436.

(167) Blakey, I.; Merican, Z.; Rintoul, L.; Chuang, Y.-M.; Jack, K. S.; Micallef, A. S. Interactions of Iodoperfluorobenzene Compounds with Gold Nanoparticles. *Phys. Chem. Chem. Phys.* **2012**, *14* (10), 3604–3611.

(168) Slavin, S.; Soeriyadi, A. H.; Voorhaar, L.; Whittaker, M. R.; Becer, C. R.; Boyer, C.; Davis, T. P.; Haddleton, D. M. Adsorption Behaviour of Sulfur Containing Polymers to Gold Surfaces Using QCM-D. *Soft Matter* **2012**, *8* (1), 118–128.

(169) Frankamp, B. L.; Boal, A. K.; Rotello, V. M. Controlled Interparticle Spacing through Self-Assembly of Au Nanoparticles and Poly(amidoamine) Dendrimers. *J. Am. Chem. Soc.* **2002**, *124* (51), 15146–15147.

(170) Mirkin, C. A.; Letsinger, R. L.; Mucic, R. C.; Storhoff, J. J. A DNA-Based Method for Rationally Assembling Nanoparticles into Macroscopic Materials. *Nature* **1996**, *382* (6592), 607–609.

(171) Boal, A. K.; Ilhan, F.; DeRouchey, J. E.; Thurn-Albrecht, T.; Russell, T. P.; Rotello, V. M. Self-Assembly of Nanoparticles into Structured Spherical and Network Aggregates. *Nature* **2000**, *404* (6779), 746–748.

(172) Wang, J.; Xia, H.; Zhang, Y.; Lu, H.; Kamat, R.; Dobrynin, A. V; Cheng, J.; Lin, Y. Nucleation-Controlled Polymerization of Nanoparticles into Supramolecular Structures. *J. Am. Chem. Soc.* **2013**, *135* (31), 11417–11420.

(173) van Herrikhuyzen, J.; Janssen, R. A. J.; Meijer, E. W.; Meskers, S. C. J.; Schenning, A. P. H. J. Fractal-like Self-Assembly of Oligo(p-Phenylene Vinylene) Capped Gold Nanoparticles. *J. Am. Chem. Soc.* **2006**, *128* (3), 686–687.

(174) van Herrikhuyzen, J.; Willems, R.; George, S. J.; Flipse, C.; Gielen, J. C.; Christianen, P. C. M.; Schenning, A. P. H. J.; Meskers, S. C. J. Atomic Force Microscopy Nanomanipulation of Shape Persistent, Spherical, Self-Assembled Aggregates of Gold Nanoparticles. *ACS Nano* **2010**, *4* (11), 6501–6508.

(175) Zhang, X.; Li, D.; Zhou, X.-P. From Large 3D Assembly to Highly Dispersed Spherical Assembly: Weak and Strong Coordination Mediated Self-Aggregation of Au Colloids. *New J. Chem.* **2006**, *30* (5), 706.

(176) Klajn, R.; Bishop, K. J. M.; Grzybowski, B. a. Light-Controlled Self-Assembly of Reversible and Irreversible Nanoparticle Suprastructures. *Proc. Natl. Acad. Sci. U. S. A.* **2007**, *104* (25), 10305–10309.

(177) Shirman, T.; Arad, T.; van der Boom, M. E. Halogen Bonding: A Supramolecular Entry for Assembling Nanoparticles. *Angew. Chemie Int. Ed.* **2010**, *49* (5), 926–929.

(178) Hussain, I.; Wang, Z.; Cooper, A. I.; Brust, M. Formation of Spherical Nanostructures by the Controlled Aggregation of Gold Colloids. *Langmuir* **2006**, *22* (7), 2938–2941.

(179) Yan, H.; Lim, S. I.; Zhang, L.-C.; Gao, S.-C.; Mott, D.; Le, Y.; Loukrakpam, R.; An, D.-L.; Zhong, C.-J. Rigid, Conjugated and Shaped Arylethynes as Mediators for the Assembly of Gold Nanoparticles. *J. Mater. Chem.* **2011**, *21* (6), 1890–1901.

(180) Lim, I.-I. S.; Vaiana, C.; Zhang, Z.-Y.; Zhang, Y.-J.; An, D.-L.; Zhong, C.-J. X-Shaped Rigid Arylethynes to Mediate the Assembly of Nanoparticles. *J. Am. Chem. Soc.* **2007**, *129* (17), 5368–5369.

(181) Huebner, D.; Rossner, C.; Vana, P. Light-Induced Self-Assembly of Gold Nanoparticles with a Photoresponsive Polymer Shell. *Polymer* **2016**, 10.1016/j.polymer.2016.05.073.

(182) Brust, M.; Walker, M.; Bethell, D.; Schiffrin, D. J.; Whyman, R. Synthesis of Thiol-Derivatised Gold Nanoparticles in a Two-Phase Liquid-Liquid System. *J. Chem. Soc. Chem. Commun.* **1994**, No. 7, 801–802.

(183) Rama, S.; Perala, K.; Kumar, S. On the Mechanism of Phase Transfer Catalysis in Brust−Schiffrin Synthesis of Metal Nanoparticles. *Langmuir* **2013**, *29* (48), 14756–14762.

(184) Fink, J.; Kiely, C. J.; Bethell, D.; Schiffrin, D. J. Self-Organization of Nanosized Gold Particles. *Chem. Mater.* **1998**, *10* (11), 922–926.

(185) Zhou, J.; Beattie, D. A.; Sedev, R.; Ralston, J. Synthesis and Surface Structure of Thymine-Functionalized, Self-Assembled Monolayer-Protected Gold Nanoparticles. *Langmuir* **2007**, *23* (16), 9170–9177.

(186) Hussain, I.; Zhang, H.; Brust, M.; Barauskas, J.; Cooper, A. I. Emulsions-Directed Assembly of Gold Nanoparticles to Molecularly-Linked and Size-Controlled Spherical Aggregates. *J. Colloid Interface Sci.* **2010**, *350* (1), 368–372.

(187) Hussain, I.; Brust, M.; Barauskas, J.; Cooper, A. I. Controlled Step Growth of Molecularly Linked Gold Nanoparticles: From Metallic Monomers to Dimers to Polymeric Nanoparticle Chains. *Langmuir* **2009**, *25* (4), 1934–1939.

(188) Frankamp, B. L.; Uzun, O.; Ilhan, F.; Boal, A. K.; Rotello, V. M. Recognition-Mediated Assembly of Nanoparticles into Micellar Structures with Diblock Copolymers. *J. Am. Chem. Soc.* **2002**, *124* (6), 892–893.

(189) Arumugam, P.; Xu, H.; Srivastava, S.; Rotello, V. M. "Bricks and Mortar" Nanoparticle Self-Assembly Using Polymers. *Polym. Int.* **2007**, *56* (4), 461–466.

(190) Deans, R.; Ilhan, F.; Rotello, V. M. Recognition-Mediated Unfolding of a Self-Assembled Polymeric Globule. *Macromolecules* **1999**, *32* (15), 4956–4960.

(191) Rossner, C. Tuning the Interaction of RAFT Polymers with Gold Nanoparticles, Master Thesis, Georg-August-Universität Göttingen, 2013.

(192) Rossner, C.; Ebeling, B.; Vana, P. Spherical Gold-Nanoparticle Assemblies with Tunable Interparticle Distances Mediated by Multifunctional RAFT Polymers. *ACS Macro Lett.* **2013**, *2* (12), 1073–1076.

(193) Siauw, M.; Hawkett, B. S.; Perrier, S. Short Chain Amphiphilic Diblock Co-Oligomers via RAFT Polymerization. *J. Polym. Sci. Part A Polym. Chem.* **2012**, *50* (1), 187–198.

(194) Buchkremer, A.; Linn, M. J.; Timper, J. U.; Eckert, T.; Mayer, J.; Richtering, W.; von Plessen, G.; Simon, U. Synthesis and Internal Structure of Finite-Size DNA−Gold Nanoparticle Assemblies. *J. Phys. Chem. C* **2014**, *118* (13), 7174–7184.

(195) Park, S.-J.; Lazarides, A. A.; Storhoff, J. J.; Pesce, L.; Mirkin, C. A. The Structural Characterization of Oligonucleotide-Modified Gold Nanoparticle Networks Formed by DNA Hybridization. *J. Phys. Chem. B* **2004**, *108* (33), 12375–12380.

(196) Innerlohinger, J.; Wyss, H. M.; Glatter, O. Colloidal Systems with Attractive Interactions: Evaluation of Scattering Data Using the Generalized Indirect Fourier Transformation Method. *J. Phys. Chem. B* **2004**, *108* (47), 18149–18157.

(197) Wyss, H. M.; Innerlohinger, J.; Meier, L. P.; Gauckler, L. J.; Glatter, O. Small-Angle Static Light Scattering of Concentrated Silica Suspensions during in Situ Destabilization. *J. Colloid Interface Sci.* **2004**, *271* (2), 388–399.

(198) Cherhal, F.; Cousin, F.; Capron, I. Influence of Charge Density and Ionic Strength on the Aggregation Process of Cellulose Nanocrystals in Aqueous Suspension, as Revealed by Small-Angle Neutron Scattering. *Langmuir* **2015**, *31* (20), 5596–5602.

(199) Glatter, O.; Kratky, O. *Small Angle X-Ray Scattering*; Academic Press: London, 1982.

(200) Wang, T.; LaMontagne, D.; Lynch, J.; Zhuang, J.; Cao, Y. C. Colloidal Superparticles from Nanoparticle Assembly. *Chem. Soc. Rev.* **2013**, *42* (7), 2804–2823.

(201) Glatter, O. A New Method for the Evaluation of Small-Angle Scattering Data. *J. Appl. Crystallogr.* **1977**, *10* (5), 415–421.

(202) Xiong, H.; van der Lelie, D.; Gang, O. DNA Linker-Mediated Crystallization of Nanocolloids. *J. Am. Chem. Soc.* **2008**, *130* (8), 2442–2443.

(203) Ohara, P. C.; Heath, J. R.; Gelbart, W. M. Self-Assembly of Submicrometer Rings of Particles from Solutions of Nanoparticles. *Angew. Chemie Int. Ed.* **1997**, *36* (10), 1078–1080.

(204) Ohara, P. C.; Gelbart, W. M. Interplay between Hole Instability and Nanoparticle Array Formation in Ultrathin Liquid Films. *Langmuir* **1998**, *14* (12), 3418–3424.

(205) Rechberger, W.; Hohenau, A.; Leitner, a.; Krenn, J. R.; Lamprecht, B.; Aussenegg, F. R. Optical Properties of Two Interacting Gold Nanoparticles. *Opt. Commun.* **2003**, *220* (1-3), 137–141.

(206) Huang, W.; Qian, W.; Jain, P. K.; El-Sayed, M. A. The Effect of Plasmon Field on the Coherent Lattice Phonon Oscillation in Electron-Beam Fabricated Gold Nanoparticle Pairs. *Nano Lett.* **2007**, *7* (10), 3227–3234.

(207) Schreiber, R.; Do, J.; Roller, E.-M.; Zhang, T.; Schüller, V. J.; Nickels, P. C.; Feldmann, J.; Liedl, T. Hierarchical Assembly of Metal Nanoparticles, Quantum Dots and Organic Dyes Using DNA Origami Scaffolds. *Nat. Nanotechnol.* **2014**, *9* (1), 74–78.

(208) Edwardson, T. G. W.; Lau, K. L.; Bousmail, D.; Serpell, C. J.; Sleiman, H. F. Transfer of Molecular Recognition Information from DNA Nanostructures to Gold Nanoparticles. *Nat. Chem.* **2016**, *8* (2), 162–170.

(209) Nguyen, T.-D.; Tran, T.-H. Multicomponent Nanoarchitectures for the Design of Optical Sensing and Diagnostic Tools. *RSC Adv.* **2014**, *4* (2), 916–942.

(210) Borsley, S.; Flook, S.; Kay, E. R. Rapid and Simple Preparation of Remarkably Stable Binary Nanoparticle Planet–satellite Assemblies. *Chem. Commun.* **2015**, *51* (37), 7812–7815.

(211) Gandra, N.; Singamaneni, S. "Clicked" Plasmonic Core–satellites: Covalently Assembled Gold Nanoparticles. *Chem. Commun.* **2012**, *48* (94), 11540–11542.

(212) Yoon, J. H.; Lim, J.; Yoon, S. Controlled Assembly and Plasmonic Properties of Asymmetric Core-Satellite Nanoassemblies. *ACS Nano* **2012**, *6* (8), 7199–7208.

(213) Yoon, J. H.; Zhou, Y.; Blaber, M. G.; Schatz, G. C.; Yoon, S. Surface Plasmon Coupling of Compositionally Heterogeneous Core–Satellite Nanoassemblies. *J. Phys. Chem. Lett.* **2013**, *4* (9), 1371–1378.

(214) Yoon, J. H.; Yoon, S. Probing Interfacial Interactions Using Core-Satellite Plasmon Rulers. *Langmuir* **2013**, *29* (48), 14772–14778.

(215) Kanaras, A. G.; Wang, Z.; Bates, A. D.; Cosstick, R.; Brust, M. Towards Multistep Nanostructure Synthesis Programmed Enzymatic Self-Assembly of DNA/Gold Systems. *Angew. Chemie Int. Ed.* **2003**, *42* (2), 191–194.

(216) Park, S. Y.; Lytton-Jean, A. K. R.; Lee, B.; Weigand, S.; Schatz, G. C.; Mirkin, C. A. DNA-Programmable Nanoparticle Crystallization. *Nature* **2008**, *451* (7178), 553–556.

(217) Zhang, C.; Macfarlane, R. J.; Young, K. L.; Choi, C. H. J.; Hao, L.; Auyeung, E.; Liu, G.; Zhou, X.; Mirkin, C. A. A General Approach to DNA-Programmable Atom Equivalents. *Nat. Mater.* **2013**, *12* (8), 741–746.

(218) Xu, X.; Rosi, N. L.; Wang, Y.; Huo, F.; Mirkin, C. A. Asymmetric Functionalization of Gold Nanoparticles with Oligonucleotides. *J. Am. Chem. Soc.* **2006**, *128* (29), 9286–9287.

(219) Sebba, D. S.; Lazarides, A. A. Robust Detection of Plasmon Coupling in Core–Satellite Nanoassemblies Linked by DNA. *J. Phys. Chem. C* **2008**, *112* (47), 18331–18339.

(220) Pal, S.; Sharma, J.; Yan, H.; Liu, Y. Stable Silver Nanoparticle-DNA Conjugates for Directed Self-Assembly of Core-Satellite Silver-Gold Nanoclusters. *Chem. Commun.* **2009**, No. 40, 6059–6061.

(221) Fan, J. A.; He, Y.; Bao, K.; Wu, C.; Bao, J.; Schade, N. B.; Manoharan, V. N.; Shvets, G.; Nordlander, P.; Liu, D. R.; et al. DNA-Enabled Self-Assembly of Plasmonic Nanoclusters. *Nano Lett.* **2011**, *11* (11), 4859–4864.

(222) Lermusiaux, L.; Sereda, A.; Portier, B.; Larquet, E.; Bidault, S. Reversible Switching of the Interparticle Distance in DNA-Templated Gold Nanoparticle Dimers. *ACS Nano* **2012**, *6* (12), 10992–10998.

(223) Li, K.; Wang, K.; Qin, W.; Deng, S.; Li, D.; Shi, J.; Huang, Q.; Fan, C. DNA-Directed Assembly of Gold Nanohalo for Quantitative Plasmonic Imaging of Single-Particle Catalysis. *J. Am. Chem. Soc.* **2015**, *137* (13), 4292–4295.

(224) Chou, L. Y. T.; Zagorovsky, K.; Chan, W. C. W. DNA Assembly of Nanoparticle Superstructures for Controlled Biological Delivery and Elimination. *Nat. Nanotechnol.* **2014**, *9* (2), 148–155.

(225) Rossner, C.; Vana, P. Nanocomposites and Self-Assembled Structures via Controlled Radical Polymerization. *Adv. Polym. Sci.* **2016**, *270*, 193–220.

(226) Zhang, L.; Xu, Y.; Yao, H.; Xie, L.; Yao, J.; Lu, H.; Yang, P. Boronic Acid Functionalized Core-Satellite Composite Nanoparticles for Advanced Enrichment of Glycopeptides and Glycoproteins. *Chem. Eur. J.* **2009**, *15* (39), 10158–10166.

(227) Boschmann, D.; Vana, P. Z-RAFT Star Polymerizations of Acrylates: Star Coupling via Intermolecular Chain Transfer to Polymer. *Macromolecules* **2007**, *40* (8), 2683–2693.

(228) Turkevich, J.; Stevenson, P. C.; Hillier, J. A Study of the Nucleation and Growth Processes in the Synthesis of Colloidal Gold. *Discuss. Faraday Soc.* **1951**, No. 11, 55–75.

(229) Xia, H.; Xiahou, Y.; Zhang, P.; Ding, W.; Wang, D. Revitalizing the Frens Method To Synthesize Uniform, Quasi-Spherical Gold Nanoparticles with Deliberately Regulated Sizes from 2 to 330 nm. *Langmuir* **2016**, *32* (23), 5870–5880.

(230) Chow, M. K.; Zukoski, C. F. Gold Sol Formation Mechanisms: Role of Colloidal Stability. *J. Colloid Interface Sci.* **1994**, *165* (2), 97–109.

(231) Ebeling, B. *Smart Nanohybrids of RAFT Polymers and Inorganic*; Springer: Cham, Heidelberg, New York, Dordrecht, London, 2015.

(232) Ebeling, B.; Eggers, S.; Hendrich, M.; Nitschke, A.; Vana, P. Flipping the Pressure- and Temperature-Dependent Cloud-Point Behavior in the Cononsolvency System of poly(N-Isopropylacrylamide) in Water and Ethanol. *Macromolecules* **2014**, *47* (4), 1462–1469.

(233) Fröhlich, M. G.; Vana, P.; Zifferer, G. Shielding Effects in Polymer-Polymer Reactions, 1 Z-RAFT Star Polymerization of For-Arm Stars. *Macromol. Theory Simulations* **2007**, *16* (6), 610–618.

(234) Boschmann, D.; Mänz, M.; Pöppler, A.-C.; Sörensen, N.; Vana, P. Tracing Arm-Growth Initiation in Z-RAFT Star Polymerization by NMR: The Impact of the Leaving R-Group on Star Topology. *J. Polym. Sci. Part A Polym. Chem.* **2008**, *46* (21), 7280–7286.

(235) Joanny, J. F.; A, J. Adsorption of Polymers with Various Architectures: Mean Field Theory. *J. Phys. II* **1996**, *6* (4), 511–527.

(236) Mayadunne, R. T. A.; Jeffery, J.; Moad, G.; Rizzardo, E. Living Free Radical Polymerization with Reversible Addition−Fragmentation Chain Transfer (RAFT Polymerization): Approaches to Star Polymers. *Macromolecules* **2003**, *36* (5), 1505–1513.

(237) Boschmann, D.; Edam, R.; Schoenmakers, P. J.; Vana, P. Z-RAFT Star Polymerizations of Styrene: Comprehensive Characterization Using Size-Exclusion Chromatography. *Polymer* **2008**, *49* (24), 5199–5208.

(238) Boschmann, D.; Edam, R.; Schoenmakers, P. J.; Vana, P. Characterization of Z-RAFT Star Polymerization of Butyl Acrylate by Size-Exclusion Chromatography. *Macromol. Symp.* **2009**, *275-276*, 184–196.

(239) Boles, M. A.; Talapin, D. V. Many-Body Effects in Nanocrystal Superlattices: Departure from Sphere Packing Explains Stability of Binary Phases. *J. Am. Chem. Soc.* **2015**, *137* (13), 4494–4502.

(240) Rossner, C.; Glatter, O.; Saldanha, O.; Köster, S.; Vana, P. The Structure of Gold-Nanoparticle Networks Cross-Linked by Di- and Multifunctional RAFT Oligomers. *Langmuir* **2015**, *31* (38), 10573–10582.

(241) Kryachko, E. S.; Remacle, F. Three-Gold Clusters Form Nonconventional Hydrogen Bonds O-H···Au and N-H···Au with Formamide and Formic Acid. *Chem. Phys. Lett.* **2005**, *404* (1-3), 142–149.

(242) Schmidbaur, H.; Raubenheimer, H. G.; Dobrzańska, L. The Gold-Hydrogen Bond, Au-H, and the Hydrogen Bond to Gold, Au···H-X. *Chem. Soc. Rev.* **2014**, *43* (1), 345–380.

(243) Rossner, C.; Tang, Q.; Glatter, O.; Müller, M.; Vana, P. Uniform Distance Scaling Behavior of Planet–Satellite Nanostructures. *submitted to ACS Nano.*

(244) Rossner, C.; Vana, P. Planet–Satellite Nanostructures Made To Order by RAFT Star Polymers. *Angew. Chemie Int. Ed.* **2014**, *53* (46), 12639–12642.

(245) Buchkremer, A.; Linn, M. J.; Reismann, M.; Eckert, T.; Witten, K. G.; Richtering, W.; von Plessen, G.; Simon, U. Stepwise Thermal and Photothermal Dissociation of a Hierarchical Superaggregate of DNA-Functionalized Gold Nanoparticles. *Small* **2011**, *7* (10), 1397–1402.

(246) Glatter, O. The Interpretation of Real-Space Information from Small-Angle Scattering Experiments. *J. Appl. Crystallogr.* **1979**, *12* (2), 166–175.

(247) Che, J.; Park, K.; Grabowski, C. A.; Jawaid, A.; Kelley, J.; Koerner, H.; Vaia, R. A. Preparation of Ordered Monolayers of Polymer Grafted Nanoparticles: Impact of Architecture, Concentration, and Substrate Surface Energy. *Macromolecules* **2016**, *49* (5), 1834–1847.

(248) Maye, M. M.; Luo, J.; Han, L.; Zhong, C. Probing pH-Tuned Morphological Changes in Core−Shell Nanoparticle Assembly Using Atomic Force Microscopy. *Nano Lett.* **2001**, *1* (10), 575–579.

(249) Sabouri, H.; Huang, Y.; Ohno, K.; Perrier, S. Silica Core–polystyrene Shell Nanoparticle Synthesis and Assembly in Three Dimensions. *Nanoscale* **2015**, *7* (45), 19036–19046.

(250) Wu, C.-K.; Hultman, K. L.; O'Brien, S.; Koberstein, J. T. Functional Oligomers for the Control and Fixation of Spatial Organization in Nanoparticle Assemblies. *J. Am. Chem. Soc.* **2008**, *130* (11), 3516–3520.

(251) Ojha, S.; Beppler, B.; Dong, H.; Matyjaszewski, K.; Garoff, S.; Bockstaller, M. R. Impact of Polymer Graft Characteristics and Evaporation Rate on the Formation of 2-D Nanoparticle Assemblies. *Langmuir* **2010**, *26* (16), 13210–13215.

(252) Boyer, C.; Whittaker, M. R.; Chuah, K.; Liu, J.; Davis, T. P. Modulation of the Surface Charge on Polymer-Stabilized Gold Nanoparticles by the Application of an External Stimulus. *Langmuir* **2010**, *26* (4), 2721–2730.

(253) Ye, X.; Zhu, C.; Ercius, P.; Raja, S. N.; He, B.; Jones, M. R.; Hauwiller, M. R.; Liu, Y.; Xu, T.; Alivisatos, A. P. Structural Diversity in Binary Superlattices Self-Assembled from Polymer-Grafted Nanocrystals. *Nat. Commun.* **2015**, *6*, 10052.

(254) Liang, M.; Lin, I.-C.; Whittaker, M. R.; Minchin, R. F.; Monteiro, M. J.; Toth, I. Cellular Uptake of Densely Packed Polymer Coatings on Gold Nanoparticles. *ACS Nano* **2010**, *4* (1), 403–413.

(255) Quinn, J. F.; Chaplin, R. P.; Davis, T. P. Facile Synthesis of Comb, Star, and Graft Polymers via Reversible Addition–Fragmentation Chain Transfer (RAFT) Polymerization. *J. Polym. Sci. Part A Polym. Chem.* **2002**, *40* (17), 2956–2966.

(256) Strube, O. I.; Schmidt-Naake, G. Synthesis of Reactive Triblock Copolymers via Reversible Addition-Fragmentation Chain Transfer (RAFT) Polymerization. *Macromol. Symp.* **2009**, *275-276*, 13–23.

(257) Cen, L.; Neoh, K. G.; Kang, E. T. Gold Nanocrystal Formation on Viologen-Functionalized Polymeric Nanospheres. *Adv. Mater.* **2005**, *17* (13), 1656–1661.

(258) Rathod, P. B.; Pandey, A. K.; Meena, S. S.; Athawale, A. A. Quaternary Ammonium Bearing Hyper-Crosslinked Polymer Encapsulation on Fe_3O_4 Nanoparticles. *RSC Adv.* **2016**, *6* (26), 21317–21325.

(259) Peng, W.; Rossner, C.; Roddatis, V.; Vana, P. Gold-Planet–Silver-Satellite Nanostructures Using RAFT Star Polymer. *ACS Macro Lett.* **2016**, *5* (11), 1227–1231.

(260) Förster, N.; Schmidt, S.; Vana, P. Tailoring Confinement: Nano-Carrier Synthesis via Z-RAFT Star Polymerization. *Polymers (Basel).* **2015**, *7* (4), 695–716.

(261) Hirschfeld-Warneken, V. C.; Arnold, M.; Cavalcanti-Adam, A.; López-García, M.; Kessler, H.; Spatz, J. P. Cell Adhesion and Polarisation on Molecularly Defined Spacing Gradient Surfaces of Cyclic RGDfK Peptide Patches. *Eur. J. Cell Biol.* **2008**, *87* (8-9), 743–750.

(262) Kruss, S.; Erpenbeck, L.; Amschler, K.; Mundinger, T. A.; Boehm, H.; Helms, H.; Friede, T.; Andrews, R. K.; Schön, M. P.; Spatz, J. P. Adhesion Maturation of Neutrophils on Nanoscopically Presented Platelet Glycoprotein Iba. *ACS Nano* **2013**, *7* (11), 9984–9996.

(263) Amschler, K.; Erpenbeck, L.; Kruss, S.; Schön, M. P. Nanoscale Integrin Ligand Patterns Determine Melanoma Cell Behavior. *ACS Nano* **2014**, *8* (9), 9113–9125.

(264) Orthaber, D.; Bergmann, A.; Glatter, O. SAXS Experiments on Absolute Scale with Kratky Systems Using Water as a Secondary Standard. *J. Appl. Crystallogr.* **2000**, *33* (2), 218–225.

(265) Schneider, C. A.; Rasband, W. S.; Eliceiri, K. W. NIH Image to ImageJ: 25 Years of Image Analysis. *Nat. Methods* **2012**, *9* (7), 671–675.

(266) Kottke, T.; Stalke, D. Crystal Handling at Low Temperatures. *J. Appl. Crystallogr.* **1993**, *26* (4), 615–619.

(267) Kottke, T.; Lagow, R. J.; Stalke, D. Low-Cost Conversion of a Co-Axial Nozzle Arrangement into a Stationary Low-Temperature Attachment. *J. Appl. Crystallogr.* **1996**, *29* (4), 465–468.

(268) Stalke, D. Cryo Crystal Structure Determination and Application to Intermediates. *Chem. Soc. Rev.* **1998**, *27* (3), 171–178.

(269) Krause, L.; Herbst-Irmer, R.; Sheldrick, G. M.; Stalke, D. Comparison of Silver and Molybdenum Microfocus X-Ray Sources for Single-Crystal Structure Determination. *J. Appl. Crystallogr.* **2015**, *48* (1), 3–10.

(270) Sheldrick, G. M. SHELXT - Integrated Space-Group and Crystal-Structure Determination. *Acta Crystallogr. Sect. A* **2015**, *71* (1), 3–8.

(271) Sheldrick, G. M. Crystal Structure Refinement with SHELXL. *Acta Crystallogr. Sect. C* **2015**, *71* (1), 3–8.

(272) Sheldrick, G. M. A Short History of SHELX. *Acta Crystallogr. Sect. A* **2008**, *64* (1), 112–122.

(273) Sebakhy, K. O.; Gavrilov, M.; Valade, D.; Jia, Z.; Monteiro, M. J. Nanoparticles of Well-Defined 4-Arm Stars Made Using Nanoreactors in Water. *Macromol. Rapid Commun.* **2014**, *35* (2), 193–197.

(274) Karg, M.; Schelero, N.; Oppel, C.; Gradzielski, M.; Hellweg, T.; von Klitzing, R. Versatile Phase Transfer of Gold Nanoparticles from Aqueous Media to Different Organic Media. *Chem. Eur. J.* **2011**, *17* (16), 4648–4654.

Acknowledgements

First of all, I want to express my extraordinary gratitude to my supervisor Professor Philipp Vana for his exceptional and continuous support and guidance during my work. Professor Alec Wodtke deserves special credit for being co-referent of that work.

Professor Michael Buback, Professor Martin Suhm, Professor Dietmar Stalke, and Professor Claudia Höbartner are gratefully acknowledged for being part of my thesis committee.

I am very lucky that I had the opportunity to collaborate with many different people on special topics, which was both very fruitful and a lot of fun. Therefore, I am very thankful to Professor Otto Glatter to host me during two research stays in his lab in Graz, Austria, for introducing me to SAXS, and for the many interesting and funny discussions. Professor Sarah Köster and Oliva Saldanha are acknowledged for giving me the opportunity to perform SAXS measurements on their lab source in Göttingen and for support with these measurements. Dr. Vladimir Roddatis and Dr. Sergei Lopatin performed the elemental mapping presented in this work, which gave very detailed insights into the structure of the materials studied in this work. I want to thank Peter Stollberg and Alexander Paesch from Professor Stalke's research group a lot for performing single crystal structure analysis. Qiyun Tang and Marcus Müller are acknowledged for a very fruitful collaboration, which involved the simulation of hybrid structures. I want to thank Dr. Jens Grosche for the graphical design of the synthetic scheme for the fabrication of planet–satellite structures (Scheme 4.1).

Generous support from the *Fonds der Chemischen Industrie* (PhD fellowship), the *DFG* (project number VA226-10/1), and the *Georg-August-Universität Göttingen* is gratefully acknowledged.

I want to thank all members of the MMC and TMC groups for contributing to a very nice working environment, for a lot of support, interesting and cheerful discussions, and for making the three PhD years a very joyful time.

I would also like to acknowledge Katharina Dabow, Alex Groschopp, Michael Hendrich, Dennis Hübner, Julia Möhrke, Wentao Peng, Radka Tomečková, and Jannik Wagner for thorough proof reading of this work.

Above all, I want to deeply thank my friends, my family, and my partner Radka for their unconditional and loving support at any time. I keep in loving memory my grandad Dietmar, who sparked my fascination for Chemistry already at young age. To him I dedicate this thesis.

Appendices

Appendix A

^{1}H NMR Spectra for RAFT Oligomers of Styrene

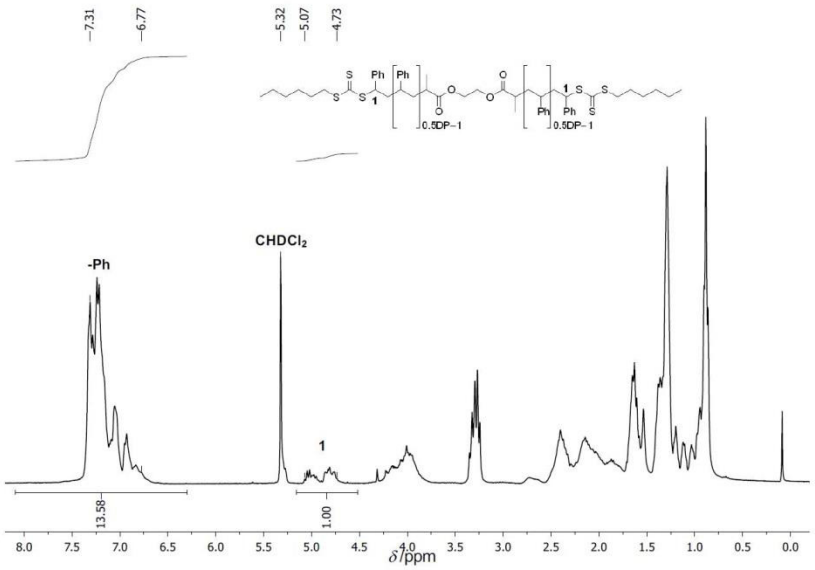

Figure A1 ^{1}H NMR spectrum of telechelic RAFT oligomer **L^{2}a**.

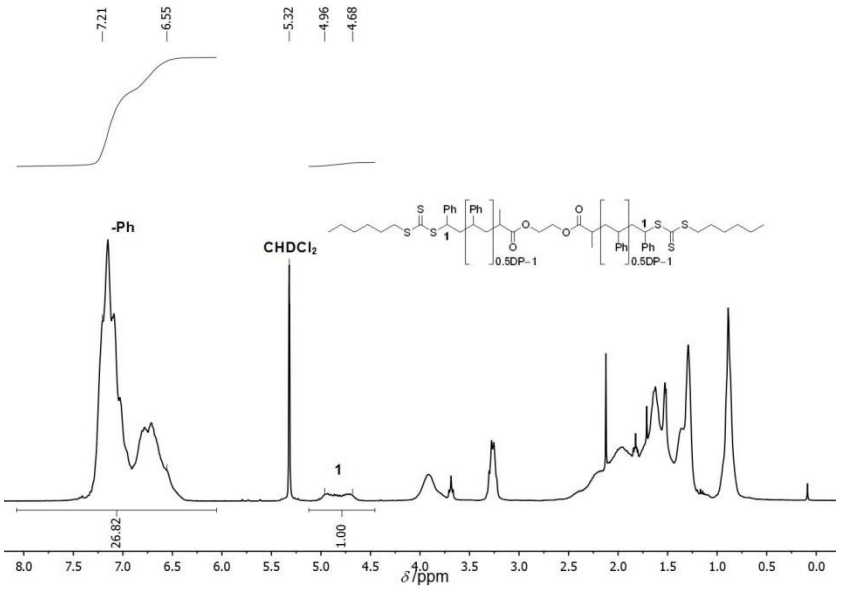

Figure A2 ^{1}H NMR spectrum of telechelic RAFT oligomer **L^{2}b**.

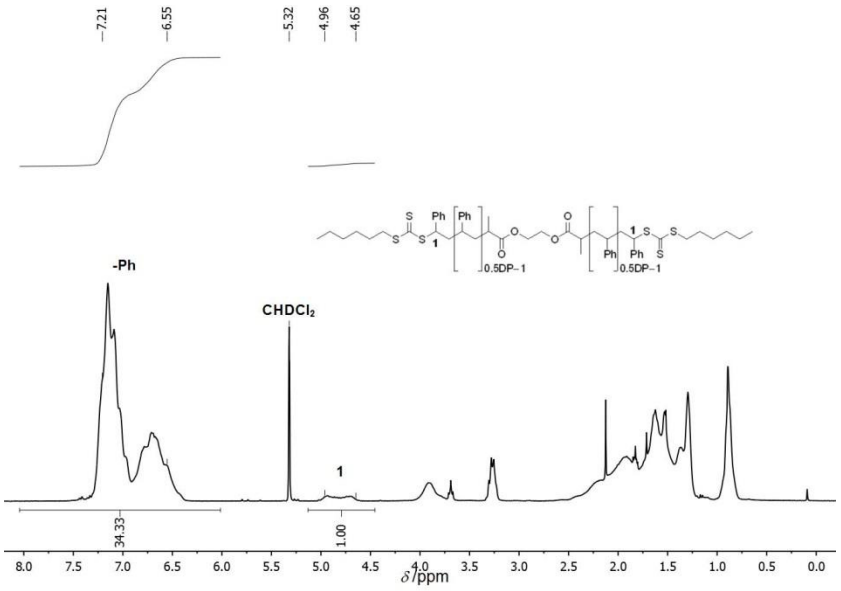

Figure A3 [1]H NMR spectrum of telechelic RAFT oligomer **L[2]c**.

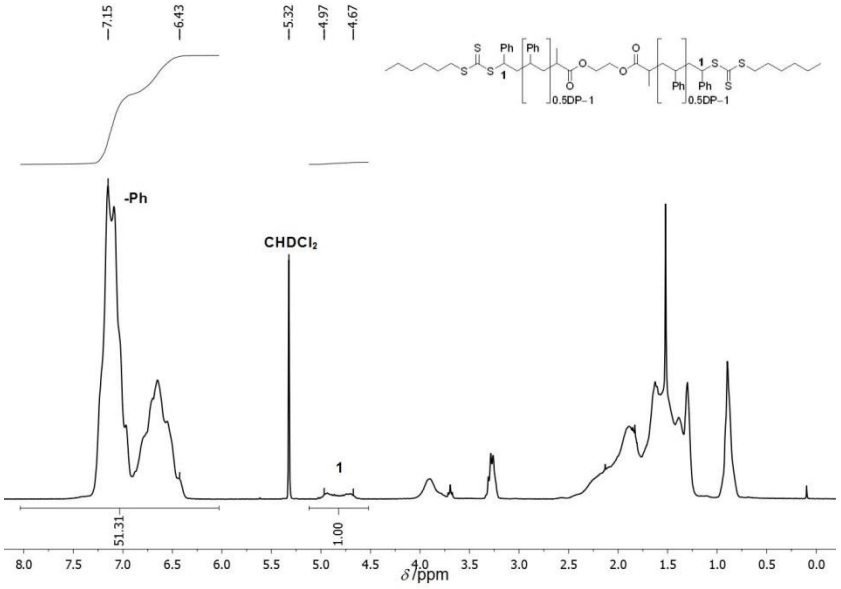

Figure A4 [1]H NMR spectrum of telechelic RAFT oligomer **L[2]d**.

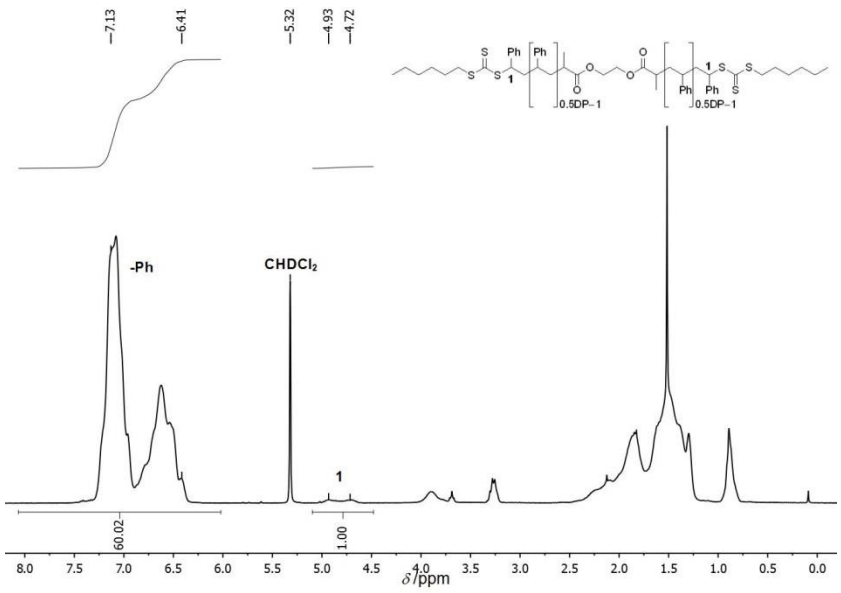

Figure A5 [1]H NMR spectrum of telechelic RAFT oligomer **L[2]e**.

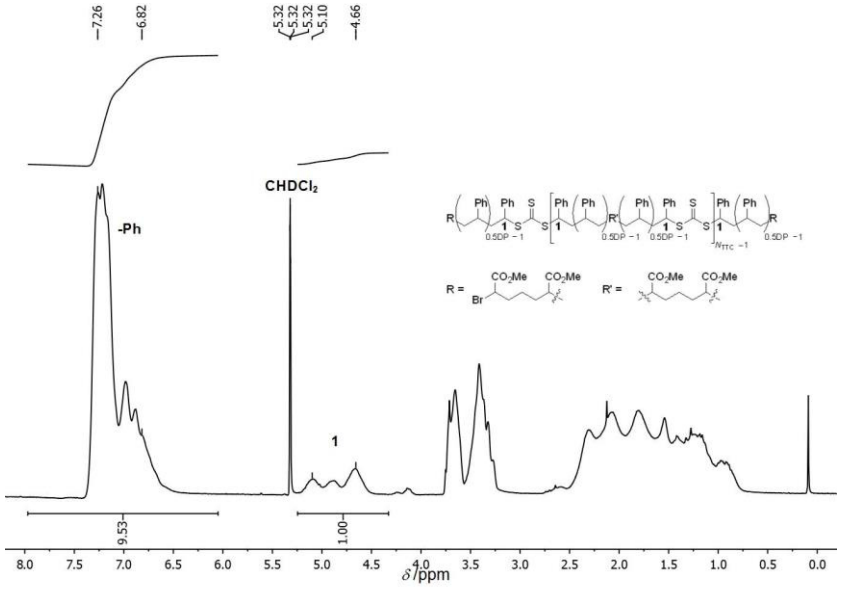

Figure A6 [1]H NMR spectrum of multifunctional RAFT oligomer **L[m]a**.

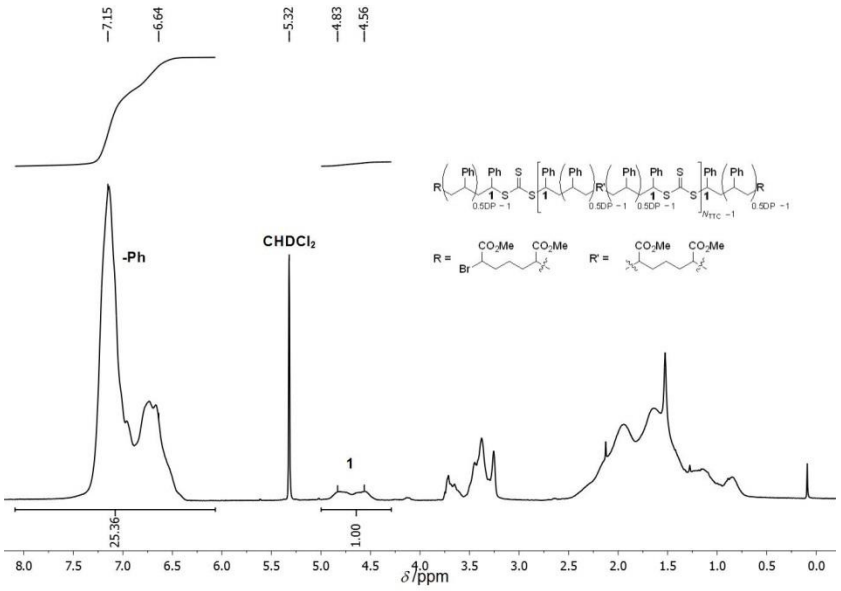

Figure A7 ^{1}H NMR spectrum of multifunctional RAFT oligomer **L^{m}b**.

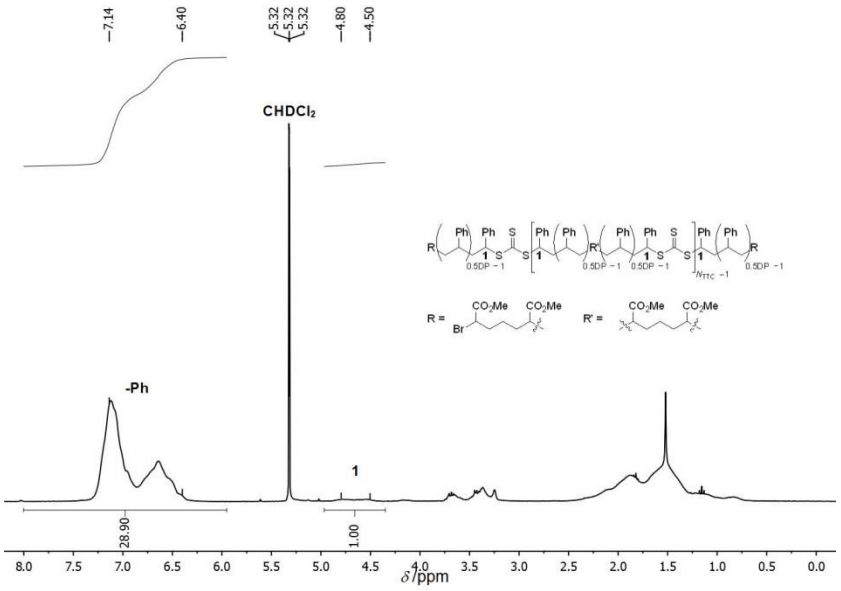

Figure A8 ^{1}H NMR spectrum of multifunctional RAFT oligomer **L^{m}c**.

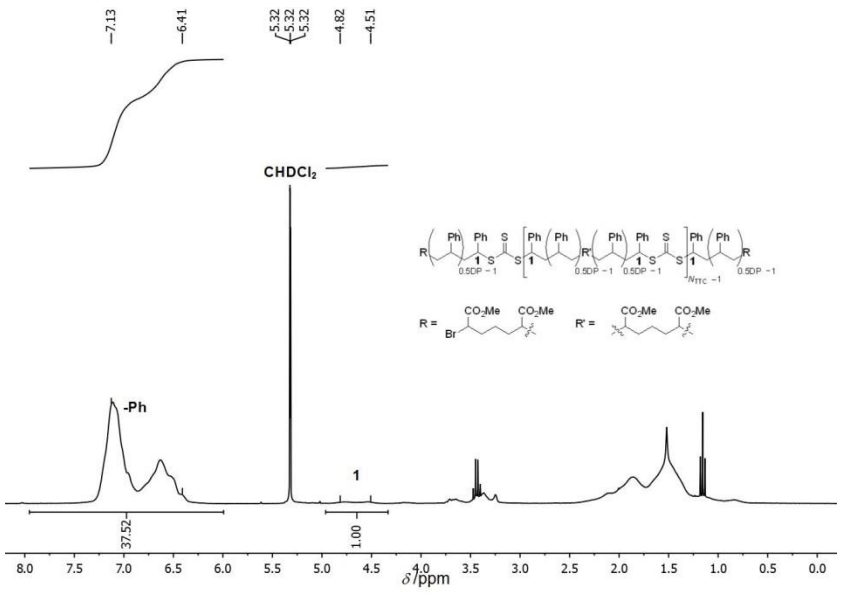

Figure A9 [1]H NMR spectrum of multifunctional RAFT oligomer $\mathbf{L^m d}$.

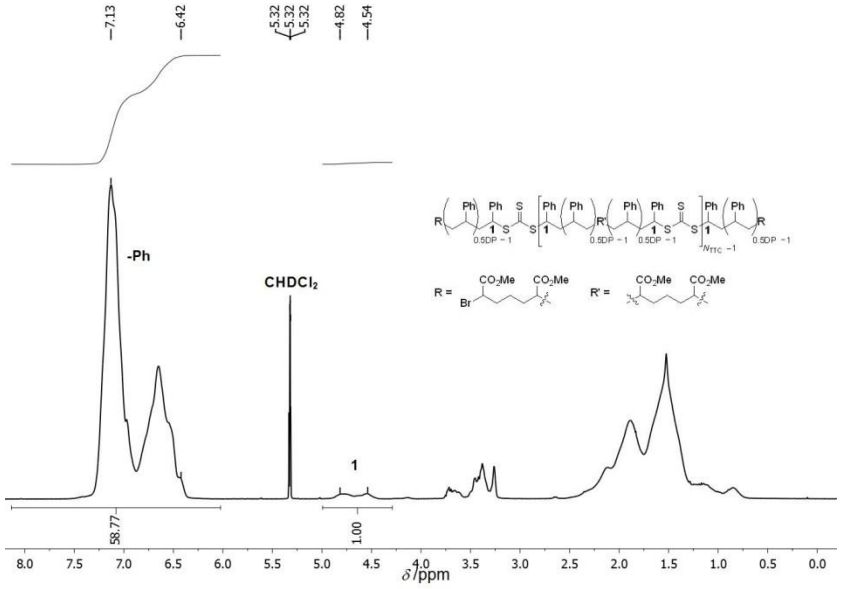

Figure A10 [1]H NMR spectrum of multifunctional RAFT oligomer $\mathbf{L^m e}$.

Appendix B

Porod Approximation of SAXS Profiles

For the Porod regime, the scattered intensity was approximated by the following form (for point collimation, see experimental)

$$I(q) = I_{bg} + p_0 \cdot q^{-4} \Leftrightarrow I(q) \cdot q^4 = I_{bg} \cdot q^4 + p_0 ,$$

where I_{bg} can be interpreted as contributions from the background to the scattered intensity. Consequently, by neglecting background intensity, the expression $I(q) \cdot q^2$ is given by:

$$I(q) \cdot q^2 = p_0 \cdot q^{-2}$$

This is straightforward to integrate:

$$\int_{q=2.0}^{\infty} I(q) \cdot q^2 \mathrm{d}q = p_0 \int_{q=2.0}^{\infty} q^{-2} \mathrm{d}q = -\frac{p_0}{q}\Big|_{2.0}^{\infty} .$$

See Figures B1 and B2 for two Porod fits used for the analysis in Section 3.3.

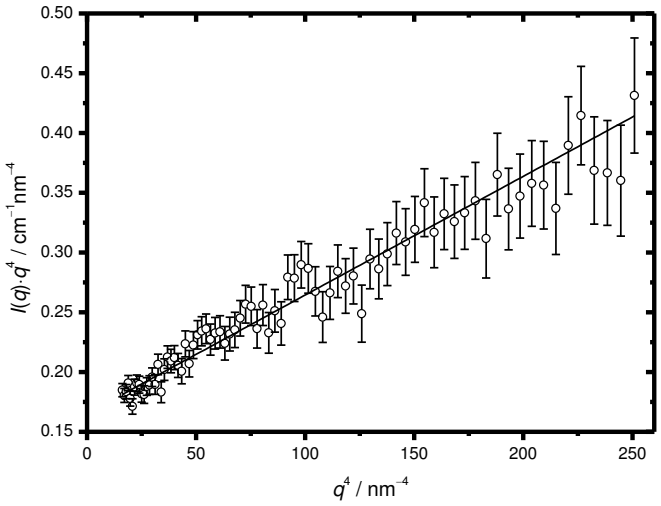

Figure B1 Porod fit of the scattering data for sample $\mathbf{L^1_{NC}}$ in a q-range $2.0 < q < 4.0$. From the linear fit, a Porod constant $p_0 = 0.17$ cm^{-1}nm^{-4} and a contribution of the background to the scattering profile of $I_{bg} = 1.0 \cdot 10^{-3}$ cm^{-1} can be obtained.

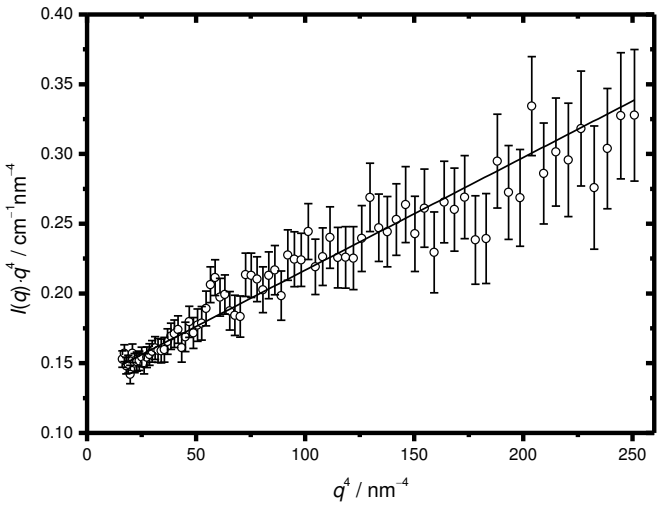

Figure B2 Porod fit of the scattering data for sample $\mathbf{L^2_{NC}}$ in a q-range $2.0 < q < 4.0$. From the linear fit, a Porod constant $p_0 = 0.14$ cm^{-1}nm^{-4} and a contribution of the background to the scattering profile of $I_{bg} = 8.1 \cdot 10^{-4}$ cm^{-1} can be obtained.

Appendix C

Additional SAXS Data and TE micrograph

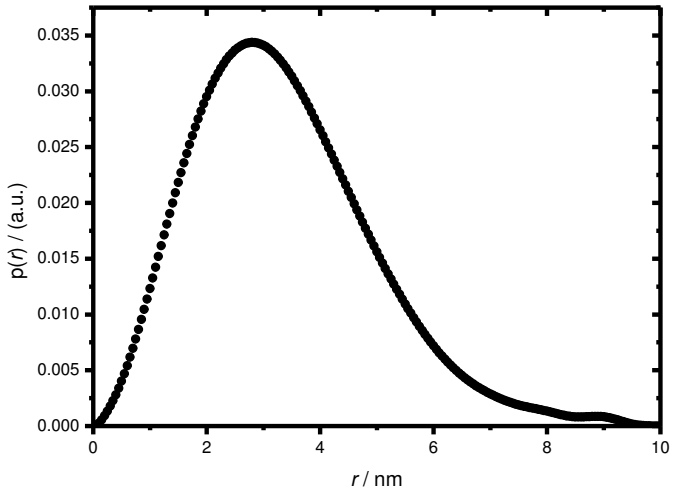

Figure C1 Pair-distance distribution function (PDDF) determined *via* indirect Fourier Transformation of the scattering profile for sample $\mathbf{L}^{1}_{\mathbf{NC}}$. This PDDF shows a maximum dimension of the scattering objects of approx. 9.5 nm.

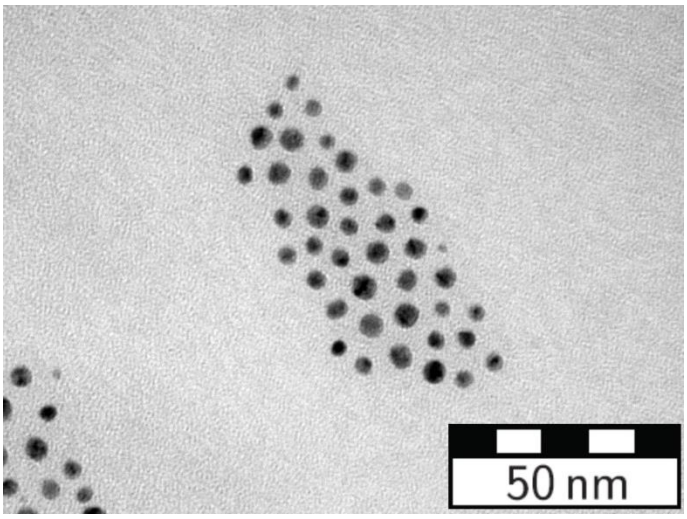

Figure C2 A representative TE micrograph of sample $\mathbf{L}^{2}\mathbf{e}_{\mathbf{NC}}$.

Appendix D

Exemplary Calculations of PDDFs for Multibody Model Structures

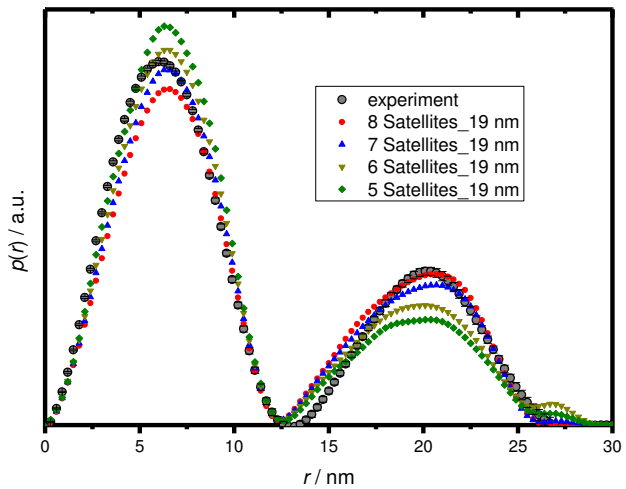

Figure D1 The influence of the number of satellite particles on model PDDFs (colored data points) in comparison with the experimental data for planet–satellite nanostructure with star polymer **S^3-23k** (gray cicles). Planet–satellite center-to-center distances were fixed to 19 nm for all models.

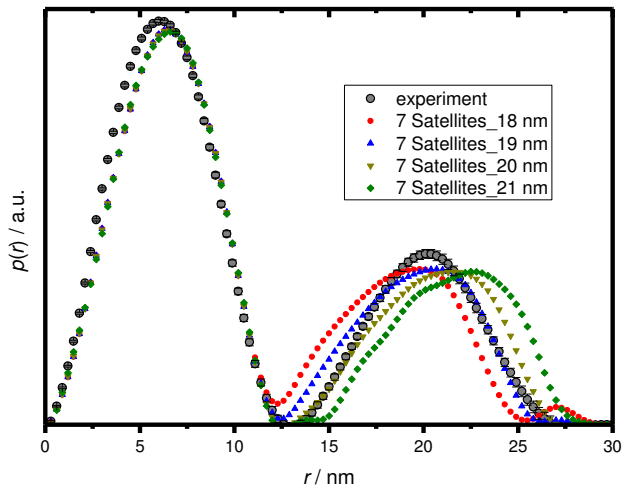

Figure D2 The influence of planet–satellite center-to-center distances on model PDDFs (colored data points) in comparison with the experimental data for planet–satellite nanostructure with star polymer **S^3-23k** (gray cicles).

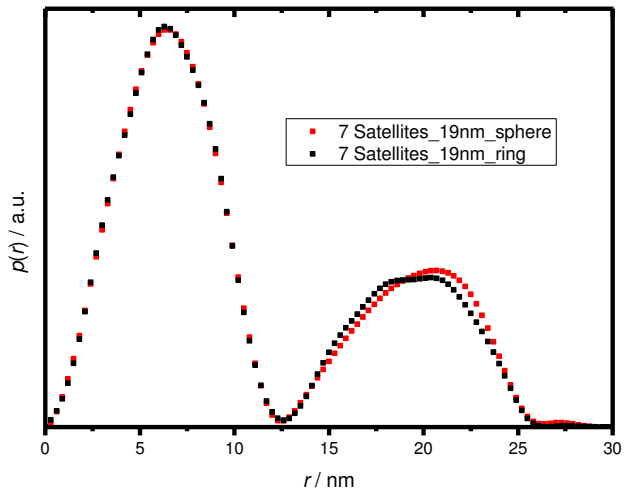

Figure D3 The influence of particle arrangement on model PDDFs exemplified for 7 satellites arranged in pentagonal-bipyramidal geometry (red data points) in comparison with planar heptagonal arrangement (black data points). Planet–satellite center-to-center distances were fixed to 19 nm in both models.

Appendix E

Crystallographic Details

Chloro(dibenzyl trithiocarbonato) gold(I) (Analysis undertaken by Peter Stollberg)

Empirical formula	$C_{30}\ H_{28}\ Au_2\ Cl_2\ S_6$	
Formula weight	1045.72	
Temperature	100(2) K	
Wavelength	0.71073 Å	
Crystal system	Monoclinic	
Space group	$P2_1/c$	
Unit cell dimensions	a = 11.25(2) Å	α= 90°.
	b = 6.08(2) Å	β= 92.933(2)°.
	c = 23.43(3) Å	γ = 90°.
Volume	1600(6) $Å^3$	
Z	2	
Density (calculated)	2.171 Mg/m^3	
Absorption coefficient	9.739 mm^{-1}	
F(000)	992	
Crystal size	0.146 x 0.086 x 0.076 mm^3	
Theta range for data collection	0.870 to 25.354°.	
Index ranges	$-12 \le h \le 13, -7 \le k \le 7, -28 \le l \le 28$	
Reflections collected	23928	
Independent reflections	2977 [R(int) = 0.0287]	
Completeness to theta = 25.242°	100.0 %	
Absorption correction	Semi-empirical from equivalents	
Max. and min. transmission	0.3574 and 0.2575	
Refinement method	Full-matrix least-squares on F^2	
Data / restraints / parameters	2977 / 0 / 182	
Goodness-of-fit on F^2	1.190	
Final R indices [$I > 2\sigma(I)$]	R1 = 0.0139, wR2 = 0.0311	
R indices (all data)	R1 = 0.0152, wR2 = 0.0319	
Extinction coefficient	n/a	
Largest diff. peak and hole	1.953 and −1.666 $eÅ^{-3}$	

Bis(dibenzyl trithiocarbonato) gold(I) hexafluoroantimonate (Analysis undertaken by Alexander Paesch)

Empirical formula	$C_{30}\ H_{28}\ Au\ F_6\ S_6\ Sb$
Formula weight	1013.60
Temperature	100(2) K
Wavelength	0.56086 Å
Crystal system	Triclinic
Space group	P-1
Unit cell dimensions	a = 12.462(2) Å α= 90.21(2)°.
	b = 13.645(2) Å β= 92.34(2)°.
	c = 20.235(3) Å γ = 90.25(2)°.
Volume	3437.9(9) $Å^3$
Z	4
Density (calculated)	1.958 Mg/m^3
Absorption coefficient	2.956 mm^{-1}
F(000)	1952
Crystal size	0.158 × 0.109 × 0.084 mm^3
Theta range for data collection	0.795 to 19.791°.
Index ranges	$-15 \le h \le 14, -16 \le k \le 16, -24 \le l \le 24$
Reflections collected	120004
Independent reflections	12666 [R(int) = 0.0499]
Completeness to theta = 19.665°	100.0 %
Absorption correction	Semi-empirical from equivalents
Max. and min. transmission	0.2290 and 0.2042
Refinement method	Full-matrix least-squares on F^2
Data / restraints / parameters	12666 / 7280 / 1189
Goodness-of-fit on F^2	1.093
Final R indices [$I > 2\sigma(I)$]	R1 = 0.0300, wR2 = 0.0615
R indices (all data)	R1 = 0.0490, wR2 = 0.0730
Extinction coefficient	n/a
Largest diff. peak and hole	1.627 and −2.785 $eÅ^{-3}$

Appendix F

About the Author

Christian Roßner (* September 4, 1988 in Eilenburg, German Citizen)
(Short vita.)

2008–2013 studies of Chemistry at *Georg-August-Universität Göttingen*, 2011 graduation as B.Sc. with a thesis entitled "Functionalizing RAFT Polymers using Isocyanate Chemistry" and 2013 as M.Sc. with the thesis "Tuning the interaction of RAFT Polymers with gold nanoparticles" (both degrees "with distinction", the Master degree being recognized with the Bunsen book award of the *Bunsen-Gesellschaft für Physikalische Chemie*). 2009 a student internship in the research group of Professor Thomas A. Bayer, Universitätsklinikum Göttingen (14 weeks); 2012 an internship in the department Medicinal Chemistry IV-Computational Chemistry of the Bayer AG lead by Dr. Heinrich, Berlin (14 weeks). During summer term 2011, Christian Roßner studied under supervision of Professor Sébastien Perrier, *The University of Sydney* (research focus: Functionalization of RAFT polymers). During the whole period of studies, Roßner was supported by a scholarship of the *Studienstiftung des deutschen Volkes*.

Since 2013 doctoral studies on the topic of tailored preparation of nanohybrids exploiting the characteristic features of RAFT polymerization, under supervision of Professor Philipp Vana (co-referent being Professor Alec M. Wodtke). During the winter terms 2014/15 and 2015/16 visiting researcher at *Technische Universität Graz*, under supervision of Professor Otto Glatter (methodological focus: small-angle X-ray scattering). 2014–2016, Roßner received financial support from a PhD scholarship of the *Fonds der Chemischen Industrie*. 2013–2014 and since 2016 (within the DFG funded project "Nanostructured Surfaces from Planet–Satellite Assemblies of Nanoparticles"), Roßner was employed in the research group of Professor Vana.

Publications.

(Articles published by outlets with scientific quality assurance, book publications, works accepted for publication but not yet published, and works submitted for publication.)

Rossner, C.; Tang, Q.; Glatter, O.; Müller, M.; Vana, P.: Uniform Distance Scaling Behavior of Planet–Satellite Nanostructures. *submitted to ACS Nano.*

Rossner, C.; Roddatis, V.; Lopatin, S.; Vana, P.: Functionalization of Planet–Satellite Nanostructures Revealed by Nanoscopic Localization of Distinct Macromolecular Species. *Macromol. Rapid Commun.* **2016**, *37*, 1742–1747.

Peng, W.; Rossner, C.; Roddatis, V.; Vana, P.: Gold-planet–silver-satellite nanostructures using RAFT star polymer. *ACS Macro Lett.* **2016**, *5*, 1227–1231.

Hübner, D.; Rossner, C.; Vana, P.: Light-induced self-assembly of gold nanoparticles with a photoresponsive polymer shell. *Polymer* **2016**, *In press, DOI:10.1016/j.polymer.2016.05.073.*

Rossner, C.; Vana, P.: Nanocomposites and Self-Assembled Structures via Controlled Radical Polymerization. *Advances in Polymer Science* **2016**, *270*, 193–220.

Rossner, C.; Glatter, O.; Saldanha, O.; Köster, S.; Vana, P.: The Structure of Gold-Nanoparticle Networks Cross-Linked by Di- and Multifunctional RAFT Oligomers. *Langmuir* **2015**, *31*, 10573–10582.

Rossner, C.; Ebeling, B.; Vana, P.: Design Strategies for the Fabrication of Tailored Nanocomposites via RAFT Polymerization. *Controlled Radical Polymerization: Materials (ACS Symposium Series)* **2015**, *1188*, 293–307.

Rossner, C.; Vana, P.: Planet–satellite nanostructures made to order by RAFT star polymers. *Angew. Chem. Int. Ed.* **2014**, 53, 12639–12642.// Rossner, C.; Vana, P.: Kontrollierte Herstellung von Planet-Satellit-Nanostrukturen durch RAFT-Sternpolymere. *Angew. Chem.* **2014**, 126, 12849–12852. *(Selected as hot paper.)*

Rossner, C.; Ebeling, B.; Vana, P.: Spherical gold nanoparticle assemblies with tunable interparticles distances mediated by multifunctional RAFT polymers. *ACS Macro Lett.* **2013**, 2, 1073–1076.

Gody, G.; Rossner, C.; Moraes, J.; Vana, P.; Maschmeyer, T.; Perrier, S.: One-pot RAFT/"click" chemistry via isocyanates: Efficient synthesis of α-end-functionalized polymers. *J. Am. Chem. Soc.* **2012**, 134, 12596–12603.

Venkataramani, V.; Rossner, C.; Iffland, L.; Schweyer, S.; Tamboli, I. Y.; Walter, J.; Wirths, O.; Bayer, T. A.: Histone deacetylase inhibitor valproic acid inhibits cancer cell proliferation via down-regulation of the alzheimer amyloid precursor protein. *J. Biol. Chem.* **2010**, 285, 10678–10689.

Presentations/ talks.

"Planet-satellite nanostructures from star polymers and gold nanoparticles", *80th Prague Meeting on Macromolecules "Self-Assembly in the World of Polymers"*, Prague, Czech Republic, **14.07.2016**.

„Goldnanopartikel und Polymere. Eine Liebesgeschichte", *Mannschaftswettbewerb Chemie Klasse 10*, Wilhelm-Ostwald-Gymnasium, Leipzig, Germany, **21.06.2016**.

„The RAFT Polymerization: From Macromolecular Design to Complex Nanoparticle Arrangements", *Stipendiatentreffen des Fonds der Chemischen Industrie*, Göttingen, Germany, **07.12.2015**.

"Nanocomposites and Self-Assembled Structures via Controlled Radical Polymerization", *7. Göttinger Chemie-Forum*, Göttingen, Germany, **01.07.2015**.

"Self-assembly of gold nanoparticles and RAFT polymers: Superballs and planet–satellite structures", *Fourth International Conference on Multifunctional, Hybrid and Nanomaterials*, Sitges, Spain, **11.03.2015**.

"Maßgeschneiderte Nanohybride mittels RAFT-Polymerisation", *GDCh Weihnachtskolloquium*, Georg-August-Universität Göttingen, Germany, **18.12.2014**.

"Self-assembly of gold nanoparticles and RAFT polymers: Superballs and planet-satellite structures", *2nd Summer School of the German-Japanese University Network HeKKSaGOn*, Karlsruhe Institute of Technology, Karlsruhe, Germany, **03.09.2014**.

Presentations/ posters.

"RAFT Polymerization is a Programming Language for Gold Nanoparticle Assembly", *Jülich Soft Matter Days 2015*, Bad Honnef, Germany, **12.11.2015**.

"Self-assembly of gold nanoparticles and RAFT polymers: Superballs and planet–satellite structures", *2nd Summer School of the German-Japanese University Network HeKKSaGOn*, Karlsruhe Institute of Technology, Karlsruhe, Germany, **02.09.2014**.